University of Alberta

STUDY OF MICROSCOPIC BLACK HOLES AT THE LHC USING NONCOMMUTATIVE INSPIRED GEOMETRY

by

Kingsley Emelideme

A thesis submitted to the Faculty of Graduate Studies and Research
in partial fulfillment of the requirements for the degree of

Master of Science

Department of Physics

© Kingsley Emelideme

Fall 2013

Edmonton, Alberta

I dedicate this work to all those who struggle despite the initial setbacks to keep their dreams and aspirations alive.

The future belongs to those who believe in the beauty of their dreams.

Eleanor Roosevelt

Abstract

A study for a noncommutative (NC) black hole was performed using data recorded by the ATLAS detector using proton-proton collisions at a centre-of-mass energy of 7 TeV with an integrated luminosity of 502 ± 9 pb^{-1}.

A missing transverse energy trigger was used in this search. The efficiency of the trigger versus reconstructed missing transverse energy was determined. A missing transverse energy requirement was imposed in the analysis so that the trigger was at its maximum efficiency.

A black hole production process having a cross-section of 4.67 pb was simulated with eight total dimensions, a higher dimensional Planck scale of 0.94 TeV and a black hole remnant mass of 3.6 TeV. The main goal of this thesis is to search study NC black holes in the ATLAS data. To achieve this, simulated Standard Model backgrounds events were used: QCD, $t\bar{t}$, $W+$ jets and $Z+$jets processes.

The significance of a possible black hole discovery using the ATLAS detector at the LHC was estimated after optimizing the signal yield and reducing the Standard Model simulated background contribution through the application of some derived selection criteria.

Acknowledgements

Render therefore to all their dues: tribute to whom tribute is due; custom to whom custom; fear to whom fear; honour to whom honour. Owe no man any thing, but to love one another: for he that loveth another hath fulfilled the law. Romans 13:7-8.

On this note, I would like to acknowledge the many people who made this thesis possible.

First and foremost, I wish to express my deep gratitude to my supervisor, Dr. Douglas Gingrich, the director of the Centre for Particle Physics for his patience, assistance, continued encouragement and invaluable suggestions during my work. I want to thank him for his willingness to correct and untiring support and attention all through this work which altogether made this thesis a success.

I knowledge the help and support of my research group members, Shima (former), Siva, Asif and Francesc who were always ready to explain concepts and debug scripts. To Siva, thanks for generating the data used for this work and your ever-willing effort to explain things in detail, and to Francesc, your addition to the group was timely and handy within the short time you joined the group.

Not forgetting Logan Sibley, Burkhard Ritter and Andrew Karamaou; you guys are much appreciated for your help.

Nadine and Eno, you two are like a family to me: a family across the Atlantic. Thank you guys for showing me the hospitality of the Canadian people thereby making Edmonton, Alberta a home away from home for me. I

so much enjoyed the Thanksgiving and Christmas Eve dinners. You two are a rare gem. God bless your home.

A big thank you to all my friends including Pitam Mitra, Daniiar Marlisov, Ebele Ezeokafor, Ndubisi Obi, Jessica Akande, Daniel Foster, Micah Yusuf, Adekunle Adeyanju, Saheed Amoo; your friendship is appreciated. Special thanks to the Obiosa-Maife's who made my transition to Edmonton very smooth.

Also, I would like to appreciate my big cousin, Morgan Dibie for his support and love. Dr. Solomon, God bless you for the numerous fatherly advice. The encouragement, love and prayers received from the Adepetu's is highly appreciated.

To my loving parents and siblings (Chukwudi, Joy and Blessing), thank you all for your encouragement. I really miss you all.

Finally, I would like to thank the love of my life and Elysium, Mojirola for her unrelenting love, patience, encouragement and friendship while working on this degree. Indeed, you came into my life when I needed someone the most, for I found solace in your words in the time of uncertainties. Eventually, I look forward to the day when we will be together to part no more. God bless you real good.

Table of Contents

List of Tables

List of Figures

Chapter 1

Introduction

The aim of this thesis was to study for microscopic black holes in the ATLAS (A Toroidal LHC Apparatus) detector using a noncommutative geometry inspired model. The search for microscopic black hole events was conducted with a total integrated luminosity of 502 pb^{-1} of data from the Large Hadron Collider (LHC) running at energy $\sqrt{s} = 7$ TeV.

Theories that include extra dimension, for example, the large extra dimension model proposed by Arkani-Hamed, Dimopoulos and Dvali (ADD model)[1], may lower the Planck scale to the order of the electroweak scale which may allow for the creation of black holes at particle physics accelerators, like at the LHC.

In the ADD model, the Standard Model particles, and forces are confined to our usual three dimensional space, called the brane, while gravity can propagate in extra dimensions, called the bulk. This can explain why gravity is weaker than the other three fundamental interactions (strong, electromagnetism and weak) on the brane.

The decay of black holes will have unique signatures that allow us to dis-

cover them. The main focus for this thesis has been to studying the decay of simulated black holes where we have been focusing on methods to remove Standard Model backgrounds from our signal selection. If black holes are able to be produced at the LHC, we conclude that ATLAS will have great discovery potential for black holes.

Chapter 2 briefly discusses the Standard Model of particles, beyond the Standard Model, the theoretical model for black hole production and decay at the LHC. Chapter 3 gives information about the LHC and the ATLAS experiment at the European Centre for Nuclear Research (CERN), discussing the various ATLAS sub-detectors, and how data are stored using the ATLAS trigger system. Chapter 4 introduces the data formats and analysis framework that are used within the ATLAS experiment, and Chapter 5 the trigger used in this thesis. Chapter 6 describes the analysis strategy employed in studying potential black hole events in ATLAS and the results obtained from such analysis. Finally, Chapter 7 briefly talk about the discovery potential for black hole events in the ATLAS detector.

Chapter 2

Theoretical Overview

2.A   Standard Model

The theories and discoveries of thousands of physicists over the past century have resulted in a remarkable insight into the fundamental structure of matter: less than five per cent of the Universe is found to be made from twelve basic building blocks called fundamental particles, governed by four fundamental forces – the strong, the electromagnetic, the weak and the gravitational force. Our best understanding of how these twelve particles and three of the forces – the strong, the electromagnetic and the weak are related to each other is encapsulated in the Standard Model (SM) of particles and forces. Developed in the early 1970's, it has successfully explained a host of experimental results and precisely predicted a wide variety of phenomena. Over time and through many experiments by many physicists, the Standard Model has become established as a well-tested physics theory.

The SM describes all matter and interactions as due to point-like particles. Matter consists of particles called fermions that have an internal spin of $1/2\hbar$.

Forces between fermions are mediated by integer spin particles, bosons.

There are three main symmetries in the SM. There is the U(1) hypercharge symmetry with the associated gauge boson field, B. The conserved charge is hypercharge, Y. Next there is SU(2) isospin symmetry which couples only to left-handed fermions. There are three associated gauge fields: W_1, W_2 and W_3 and the conserved charge is I_3: the third component of the isospin. These first two symmetries are described by the electroweak theory. Finally there is the SU(3) colour symmetry described by quantum chromodynamics (QCD) which has three conserved colour charges. There are eight gauge bosons, gluons, which carry a force called the strong force and these also carry colour and anti-colour.

During electroweak symmetry breaking, the W_3 and B fields mix to give the photon and Z^0 bosons which are the observed particles, while the W_1 and W_2 mix to give $W^\pm$. The charge of the remaining U(1) symmetry is the standard electromagnetic charge, $Q = Y/2 + I_3$.

The particle content consists of six quarks which are the only particles to feel the strong force. There are also six leptons which do not feel the strong force. Three carry electromagnetic charge and the other three are the neutrinos which interact only weakly with matter. Each fermion also has a corresponding antiparticle.

The particle content and their gauge charges are shown in Table 2.1 and 2.2. An interesting feature of the Standard Model is that the fermionic particles come in three generations, with each generation similar but with higher masses than the previous. Normal matter is made up of only the lightest generation: the u and d quarks and electrons.

Leptons				
Name	Mass (MeV)	Charge (Q)	Isospin (I_3)	Hypercharge (Y)
electron (e)	~ 0.511	-1	-1/2	-1
ν_e	0	0	1/2	
muon (μ)	~ 105.658	-1	-1/2	-1
ν_μ	0	0	1/2	
tau (τ)	~ 1776.990	-1	-1/2	-1
ν_τ	0	0	1/2	

Table 2.1: Lepton content in the Standard Model with relevant quantum numbers. Neutrinos are considered as massless in the SM. PDG (Particle Data Group) information [2].

Quarks				
Name	Mass (MeV)	Charge (Q)	Isospin (I_3)	Hypercharge (Y)
up (u)	$1.5 - 3.0$	2/3	1/2	1/3
down (d)	$3.0 - 7.0$	-1/3	-1/2	
charm (c)	1250 ± 90	2/3	1/2	1/3
strange (s)	95 ± 25	-1/3	-1/2	
top (t)	174200 ± 33	2/3	1/2	1/3
bottom (b)	4200 ± 70	-1/3	-1/2	

Table 2.2: Quark content in the Standard Model with relevant quantum numbers. PDG (Particle Data Group) information [2].

The SM is well understood as an effective theory in the low energy regime, but some fundamental theory beyond it is required to fulfill the picture of nature. Therefore, it is believed that there is physics beyond the Standard

Model, or new physics, which gives motivation for high energy particle physics experiments such as ATLAS [3] at the LHC [4] at CERN. Furthermore, the prominent questions in the SM are:

1. Why are there three families of leptons and quarks?

2. Is there unification of all forces?

3. Can gravity be incorporated into the theory?

4. Why are the strengths of the fundamental forces so different, reaching over many orders of magnitude?

5. Why is there is no dark matter candidate in the SM?

These questions cannot be answered by the SM. Hence, fundamental theories beyond the SM model are proposed to answer these questions. One of which is the theory of extra dimensions known as the ADD (Arkani-Hamed, Dimopoulos and Dvali) model. The ADD model attempts to incorporate gravity to the SM.

2.B   Hierarchy Problem

The hierarchy problem may be expressed in two ways. The first, known as the aesthetic hierarchy problem, notes that there appear to be two fundamental scales in particle physics: the electroweak scale (mass ~ 1 TeV) and the Planck scale (mass $\sim 10^{16}$ TeV). Why then are these two scales so different? Alternatively, this question could be phrased as: Why is gravity so weak compared to the other forces?

The second hierarchy problem, the technical hierarchy problem, stems from the Higgs mass. Since the Higgs mechanism is responsible for electroweak symmetry breaking, it would seem natural that the Higgs mass be at the electroweak scale. However, the bare Higgs mass is modified due to one-loop corrections such as those shown in Figure 2.1. These corrections are quadratically divergent and must be regulated by a energy cutoff, Λ, that limits the integral over the loop momentum.
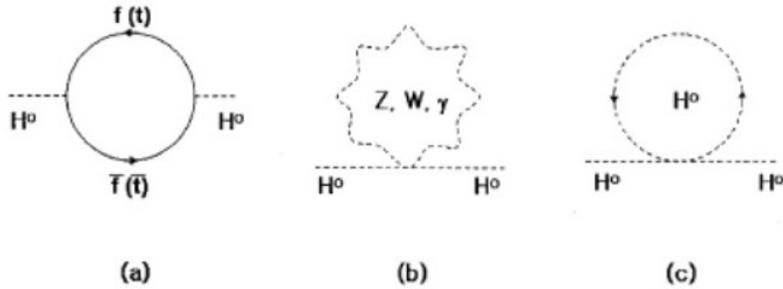
Figure 2.1: The one-loop corrections to the Higgs mass in the Standard Model, (a) Higgs coupling to fermions (b) Higgs coupling to gauge bosons (c) Higgs coupling to itself. Adapted from Ref. [5].

The resulting correction for fermion loops is of the form

$$\Delta M_H^2 = \frac{|\lambda_f|}{16\pi^2} \left[-2\Lambda^2 + 6m_f^2 \ln\left(\frac{\Lambda}{m_f}\right) + ... \right], \qquad (2.1)$$

where λ_f is the coupling of Higgs to the fermion and m_f is the fermion mass. The bosonic correction is similar but with the opposite sign for the Λ^2 term. If the SM is valid up to Planck scale energies then the natural scale for Λ would be the Planck scale.

2.C   Beyond the Standard Model

Although the SM gives a good description of low energy phenomena, it fails to describe the large difference in the coupling constants. The Grand Unified Theory (GUT) suggests that the Standard Model groups $SU(3)_C$, $SU(2)_L$ and $U(1)_Y$ are subgroups of a larger symmetry group. GUT suggests that symmetries are unbroken above a certain very large mass scale, M_X. Above this mass scale, the coupling constant can be related to a single gauge coupling.

Another theory for physics beyond the SM is the theory of superstrings. Attempts to unify all fundamental forces and include the theory of quantum gravity can be found in superstring theory. The relevant scale for this unification is at the Planck scale. Here all fundamental objects are 1-D strings, with dimensions of length.

2.C.1   Extra Dimensions

Kaluza-Klein towers

Kaluza-Klein theory (KK theory) is a model that seeks to unify the two fundamental forces of gravity and electromagnetism. The idea of using extra dimensions to unify physical theories is not new.

In 1919, Theodor Kaluza introduced a fifth dimension in an attempt to unify Einstein's theory of gravity with electromagnetism. However, his fifth dimension was essentially identical to the other spacial dimensions with no explanation for why it is not observed. Oskar Klein solved this by modifying Kaluza's idea in 1926 to make the extra dimension compacted. Ultimately their attempts to unify gravity and electromagnetism failed, but the idea of extra, compactified dimensions remained and has been revived in the models

8

that will be presented shortly.

One interesting feature of compactified extra dimensions is that they lead to a tower of masses for any field that is allowed to propagate in the extra dimensions. To see how this arises, it is useful to follow the example in Ref. [6]. Consider a 5-dimensional scalar field, $\Psi(t, x, y, z, \phi)$ where ϕ is the coordinate in the extra dimension. If the extra dimension is compactified on a circle of radius, R, then $\phi = \phi + 2\pi R$. The 5-dimensional field equation for a massive scalar is

$$(\partial_5^2 + m^2)\Psi = 0, \tag{2.2}$$

where $\partial_5^2 = \frac{d^2}{dt^2} - \frac{d^2}{dx^2} - \frac{d^2}{dy^2} - \frac{d^2}{dz^2} - \frac{d^2}{d\phi^2}$. Since solutions must be periodic in ϕ, the solution must be of the form

$$\Psi = \sum_{k \in N} \Phi_k(t, x, y, z) \exp\left(i\frac{k\phi}{R}\right). \tag{2.3}$$

The field equation is thus

$$\sum_{k \in N} \left(\partial_4^2 + m^2 + \frac{k^2}{R^2}\right) \Phi_k = 0, \tag{2.4}$$

which looks very much like a standard 4-dimensional field equation, Equation 2.2, but with a tower of mass states $\sqrt{m^2 + \frac{k^2}{R^2}}$ with a separation determined by the radius of compactification.

ADD Model

In 1998, Arkani-Hamed, Dimopoulos and Dvali (ADD) [1, 7] revived interest in extra dimensional models by proposing a model with n extra dimensions compacted on a $n-$dimensional sphere with common radius, R. Only the

9

gravitational field propagates into the extra dimensions, the Standard Model fields are restricted to the normal 3-brane (a brane is an object which can have any number of allowed dimensions).

Their motivation was to solve the hierarchy problem by reducing the Planck scale to the weak scale. How this is achieved can be seen by considering the gravitational potential when the distance between two masses is very small or very large compared with the size of the extra dimensions. If two masses, m_1 and m_2, are separated by a distance, r, with $r \ll R$ then the potential is

$$V(r) \sim G_{4+n} \frac{m_1 m_2}{r^{n+2}},$$ (2.5)

where G_{4+n} is the gravitational constant in $(4 + n)-$dimensions. However, if $r \gg R$ then the potential will be the normal Newtonian one

$$V(r) \sim G_4 \frac{m_1 m_2}{r^2}.$$ (2.6)

Requiring that these match at the boundary suggests that $G_{4+n} \sim G_4 R^n$ and therefore, given that $G_{4+n} \sim M_{PL}^{-(n+2)}$, that is

$$M_{PL}^2 \sim R^n M_{PL(n+4)}^{n+2}.$$ (2.7)

Thus, if there are enough large extra dimensions (large compared to the $(4+n)-$dimensional Planck scale) then the fundamental $(4+n)-$dimensional Planck scale can be reduced from 10^{19} GeV to the weak scale. The weakness of gravity is thus seen as a result of the extra dimensions in which it can propagate rather than any inherent weakness.

By requiring that the fundamental Planck scale be at the electroweak scale,

the size of the extra dimensions can be estimated with Equation 2.7. This gives $R \sim 10^{13}$ cm for $n = 1$ which is clearly ruled out because it deviates from solar system tests of Newtonian gravity. However, for $n = 2$, R is $\sim 0.1 - 1$ mm and for higher n they are even smaller.

Since gravity can propagate into the bulk, a Kaluza-Klein tower of graviton states emerges in much the same way as presented in Section 2.C.1. In this case, the fundamental particle, the spin-2 graviton, is massless and there is a tower of excited modes with masses $m_k = k/R$, which are normally referred to as gravitons. Since R is typically quite large in ADD models, these masses are closely spaced and can be considered to form a continuum.

It is interesting to consider the rate of typical processes which create gravitons. From a $4-$dimensional perspective, each graviton will have a coupling $\sim 1/M_{PL}$. Although this coupling is very small, there are many possible gravitons to couple to, so the combined effect can be large. If there is an energy, E, available to the graviton, then the number of graviton modes that can interact is $(ER)^n$ and thus the interaction rate to all gravitons is

$$\Gamma \sim \frac{(ER)^n}{M_{PL}^2},$$
(2.8)

which gives

$$\Gamma \sim \frac{E^n}{M_{PL(4+n)}^2}$$
(2.9)

using Equation 2.7. This is not surprising, since from a $(4 + n)-$dimensional perspective, there is only one graviton, but it will have a coupling $\sim 1/M_{PL(4+n)}$ giving the same rate as above. This is a good example of a general principle: that processes may be considered in either the effective $4-$dimensional theory,

in which case there is a tower of graviton modes; or in the $(4+n)-$dimensional theory in which case there is a single, strongly coupled, massless graviton.

2.C.2 ADD Black Holes

For an object to become a black hole, the mass of the object has to be compressed into a sphere with radius, R_S. This solution was first obtain by Karl Schwarzschild, thus known as the Schwarzschild radius. For a four dimensional object, the solution for the Schwarzschild radius was found by applying general relativity to a static non-spinning, non-charged massive object

$$R_S = 2GM, \tag{2.10}$$

where G is the Newton constant and M is the mass of the object. Equation 2.10 can be used to calculate the Schwarzschild radius for all four dimensional objects.

In the case of large extra dimensions, the solution for Schwarzschild radius changes to [8]

$$R_{BH} = \frac{1}{M_D} \left(\frac{M_{BH}}{M_D} \right)^{\frac{1}{n+1}} f(n), \tag{2.11}$$

with

$$f(n) = \left(\frac{2^n \pi^{\frac{n-3}{2}} \Gamma(\frac{n+3}{2})}{n+2} \right)^{\frac{1}{n+1}}, \tag{2.12}$$

where M_{BH} is the mass of the black hole, n is the number of extra dimensions, M_D is the Planck scale in $(4+n)-$ dimensions [2] (PDG definition) and $\Gamma(x)$ is the gamma function.

The Schwarzschild radius is an important factor in the creation of a black hole, when considering two partons traveling towards each other, with a centre

12

of mass energy of $\sqrt{s} \geq M_{BH}$. If the colliding partons pass within a distance of $r < R_S$, a black hole may form with mass M_{BH}. The parton level cross section for creation of a black hole in $(4+n)-$dimensions, can be approximated by geometrical arguments as [9]

$$\hat{\sigma}(M_{BH}) \approx \pi R_S^2 = \pi \frac{f^2(n)}{M_D^2}\left(\frac{M_{BH}}{M_D}\right)^{\frac{2}{n+1}}. \tag{2.13}$$

2.C.3 Black Hole Evaporation

Classically, black holes do not emit particles, only absorb them. But Steven Hawking showed using semiclassical arguments that black holes can evaporate by emitting Hawking radiation [10]. Hawking found that the black hole radiation spectrum is almost like a black body radiation spectrum. It is categorized by the Hawking temperature

$$T_H = \frac{\hbar c}{4\pi k R_S}, \tag{2.14}$$

where k is the Boltzmann constant and $\hbar = c = k = 1$. The Hawking temperature can be expressed in terms of number of dimensions and M_D as [8]:

$$T_H = \left(\frac{M_D}{M_{BH}}\frac{n+2}{8\Gamma(\frac{n+3}{2})}\right)^{\frac{1}{n+1}}\frac{n+1}{4\sqrt{\pi}} = \frac{n+1}{4\pi R_S}. \tag{2.15}$$

It is expected that a black hole produced at the LHC will Hawking evaporate almost instantaneously, with a life time of the order of 10^{-27} to 10^{-26} s [11]. In this short life time, one expects the black hole to go through four phases [12]. These phases are listed below:

1. Balding phase : The black hole emits mainly gravitational radiation.

13

2. Spin-down phase : The typically non-zero impact parameter of the colliding partons leads to black holes with some angular momentum about an axis perpendicular to the plane of parton collision. During this phase, the black hole loses its angular momentum through the emission of Hawking radiation.

3. Schwarzschild phase : A spherically-symmetric black hole loses energy due to the emission of Hawking radiation, which eventually results in the decrease of its mass and the increase of its temperature.

4. Planck phase : The mass and/or the Hawking temperature approaches the Planck scale. A theory of quantum gravity is necessary to study this phase but it is suggested that the black hole will decay into a few fundamental particles (in this thesis, it is a stable remnant).

The average number of particles produced during the Schwarzschild phase in a black hole decay can be estimated from the Hawking temperature, as a function of the number of dimensions and M_D. Note that this argument is based on the assumption that the decay of a black hole is a blackbody radiation process [9]. The average number is then given by

$$\langle N \rangle = \frac{2\sqrt{\pi}}{n+1} \left(\frac{M_{BH}}{M_{D(4+n)}} \right)^{\frac{n+2}{n+1}} \left(\frac{8\Gamma(\frac{n+3}{2})}{n+2} \right)^{\frac{1}{n+1}}. \qquad (2.16)$$

2.C.4   Experimental signatures

The phases of black hole decay described in the previous section combine to produce distinctive experimental signatures which make it unlikely that black hole events would be mistaken for other processes. These features are due to

14

the black hole high mass. Some of these features are:

1. Most events have a relatively high multiplicity which is result of black holes being massive excited states.

2. There is a very large total cross section (because the parton-level cross section grows with energy).

3. The ratio of hadronic to leptonic activity is roughly 5:1 because of the high degrees of freedom of quarks and gluons, and the amount of energy visible in the detector is large.

4. Events have a high sphericity (only if not spinning) since most black holes are produced almost at rest with very high energies (sphericity is a measure of how spherical (round) an object is).

For a noncommutative black hole these signatures are a little different. It is characterized by a remnant mass (large missing energy) after decaying with low transverse momentum jets.

2.D   Noncommutative Geometry Inspired Black Holes

Quantum field theory on noncommutative spacetime is an application of non-commutative mathematics to the spacetime of quantum field theory that is an outgrowth of noncommutative geometry in which the coordinate operator functions, $\hat{x}^A$ and $\hat{x}^B$ are noncommutative.

In this model, the commutation coordinates $\hat{x}^A$ and $\hat{x}^B$ in $D-$dimensions are thought of as operators. This relation can be written as:

$$[\hat{x}^A, \hat{x}^B] = i\theta^{AB} \equiv i\frac{\epsilon^{AB}}{\Lambda_{NC}^2}, \tag{2.17}$$

where Λ_{NC} is the mass scale associated with the noncommutative and the dimensionless anti-symmetric matrix structure, ϵ^{AB}, which has entries of $O(1)$.

The idea here is to formulate the noncommutative equivalent of general relativity (GR), which in turn could lead to a much deeper understanding of gravity.

The effects of noncommutative gravity can be comprehended by formulating a model in which GR is its usual commutative, and noncommutative geometry leads to a smearing of matter distributions on length scales of $O(\Lambda_{NC}^{-1})$.

Thus, the usual Dirac-delta function for mass is now replaced by a centrally peaked, spherically symmetric mass distribution which has a size of $O(\Lambda_{NC}^{-1})$. The smearing is taken as a Gaussian distribution of width $\sqrt{\theta}$ of the form:

$$\rho = \frac{m}{(4\pi\theta)^{(n+3)/2}}e^{r^2/(4\theta)}, \tag{2.18}$$

where r is the radial distance in $D-1 = n+3$ space dimensions from the most probable value of the mass, m. The width of the Gaussian smearing can be related to the noncommutative scale by

$$\sqrt{\theta} = \frac{1}{\Lambda_{NC}}. \tag{2.19}$$

This model considers the ADD [1, 7] scenario at a higher dimensional Planck scale, which is about a TeV in order to observe the effects of noncom-

mutativity. It assumes $\Lambda_{NC}^{-1} \sim M_D$ where M_D is the D-dimensional Planck scale as defined in Ref. [2].

The gravitational radius can be determined using the noncommutative ADD model. The usual black hole theories in particle collisions follow in the same fashion. By considering experimental limits on the Planck scale [13] and the energy reach of the LHC, we can restrict the parameter space to those within the LHC energies and calculate the production cross section for noncommutative inspired black holes. This allows us to make predictions that could guide searches by experiments at the LHC [14].

2.D.1   Black Hole Production

Considering spherically symmetric, nonrotating black holes with no local charges in D-dimensional space, the production cross section for black holes in particle collisions such as those obtainable at the LHC can be calculated by knowing the gravitational radius. This radius is a radius of a sphere in which the mass of an object is compressed within that sphere such that the escape speed from the surface of the sphere equals the speed of light.

Guided by the above considerations, the D-dimensional Schwarzschild-like, spherically symmetric and static solutions for a mass m have been previously obtained by Rizzo [15], and was rewritten in the form below by Gingrich [14]:

$$\frac{m}{M_D} = \frac{k_n}{P\left(\frac{n+3}{2}, \frac{r_g^2}{4\theta}\right)} \left(r_g M_D\right)^{n+1}, \tag{2.20}$$

17

and the gravitational radius r_g is written implicitly as

$$r_g(m) = \frac{1}{M_D} \left(\frac{m}{M_D} \frac{P\left(\frac{n+3}{2}, \frac{r_g^2}{4\theta}\right)}{k_n} \right)^{\frac{1}{n+1}}, \tag{2.21}$$

where

$$k_n = \frac{n+2}{2^n \pi^{(n-3)/2} \Gamma\left(\frac{n+3}{2}\right)} = f(n)^{-(n+1)} \tag{2.22}$$

and

$$P\left(\frac{n+3}{2}, \frac{r_g^2}{4\theta}\right) = \frac{1}{\Gamma\left(\frac{n+3}{2}\right)} \int_0^{r_g^2/(4\theta)} dt \; e^{-t} t^{(n+3)/2-1}. \tag{2.23}$$

The function P is the incomplete gamma function. Writing this function in a simpler form (Ref. [15])

$$F_a(q) = P\left(\frac{n+3}{2}, \frac{r_g^2}{4\theta}\right), \tag{2.24}$$

where $a = (n+3)/2$ and $q = r_g^2/(4\theta)$.

Some properties of $F_a(q)$ and implication of using an approximation are highlighted as follows:

1. $F_a(q) \to 1$ as $q \to \infty$ and $F_a(q) \to 0$ as $q \to 0$, for all values of a. More precisely $F_a(q) \sim q^a$ as $q \to 0$. The gravitational radius for a four dimensional noncommutative case is reproduced for $n \to 0$. Neither of these limits are accurate approximations of $F_a(q)$ for the cases $1 \le n \le 7$, and at the LHC energy [14].

2. From Equation 2.20 and the properties of the incomplete gamma function highlighted above, it was seen that as $r_g \to \infty$, $F_a \to 1$, and therefore $m \to \infty$. Likewise, as $r_g \to 0$, $m \sim r_g^{-2} \to \infty$. Hence, a minimum value

18

of $m = m_{\min}$ exists for some finite positive $r_g = (r_g)_{\min}$. Because there is a minimum mass, hence there are masses below which the black hole will not form, and above the minimum mass the gravitational radius has two solutions. As the masses increases, the inner gravitational radius shrinks to zero, while the outer outer gravitational radius approaches the noncommuative value. Therefore, only the outer gravitational radius $r_g \geq (r_g)_{\min}$ is relevant to this work.

It was shown that experimental lower bounds on M_D and the maximum energy of the LHC will restrict the values of $\sqrt{\theta}$ that can be probed by experiments at the LHC. Black holes are not expected to be formed for masses much less than M_D.

It should be stated here that the noncommutative geometry inspired black hole model in higher dimensions has three unknown parameters: n, M_D and $\sqrt{\theta}$. But, only parameter values that can be probed at the LHC are of interest in this research.

In order to find the gravitational radius at which the minimum mass occurs, we follow Ref. [14, 15] to calculate $\partial m / \partial r_g = 0$ for fixed $\sqrt{\theta}$ using Equation 2.20 to obtain

$$F_a(q_0) - \frac{2q_0^a e^{-q_0}}{(n+1)\Gamma(a)} = 0, \tag{2.25}$$

where q_0 is the root of the equation. We can obtain q_0 by solving Equation 2.24 for each value of a (or n). Following Ref. [14], we calculate $\sqrt{q_0}/2 = (r_g)_{\min}/\sqrt{\theta}$. The values of $(r_g)_{\min}/\sqrt{\theta}$ depend only on the number of dimensions. From the values of $(r_g)_{\min}/\sqrt{\theta}$, $(r_g)_{\min}$ was calculated, and hence the minimum mass, $m_{\min}$, for given values of $\sqrt{\theta}$ and n.

19

We obtain a valid range of $\sqrt{\theta}M_D$ for each number of dimensions by confining the minimum black hole mass at the LHC to be in the range $1 < m_{\min}/M_D < 7$ TeV$/M_D$. The results are given in Table 2.3.

n	$(r_g)_{\min}/\sqrt{\theta}$	$(m_{\min}/M_D)(\sqrt{\theta}M_D)^{-(n+1)}$	$\sqrt{\theta_{\min}}M_D$	$\sqrt{\theta_{\max}}M_D$
2	2.51	65.2	0.248	0.299
3	2.41	58.8	0.361	0.561
4	2.34	48.6	0.460	0.687
5	2.29	37.9	0.546	0.774
6	2.26	28.2	0.621	0.842
7	2.23	20.3	0.686	0.982

Table 2.3: Values of the minimum gravitational radius $(r_g)_{\min}$ in units of $\sqrt{\theta}$ and minimum mass $m_{\min}$ in units of $M_D(\sqrt{\theta}M_D)^{n+1}$. The last two columns show the range of $\sqrt{\theta}$ in units of $1/M_D$ that can be probed at the LHC. From Ref. [14].

Picking $\sqrt{\theta}M_D = 0.6$, the values for the minimum gravitational radius, $(r_g)_{\min}$, and mass, $m_{\min}$ are shown in Table 2.4.

n	$(r_g)_{\min}M_D$	$m_{\min}/M_D$
2	1.51	14.09
3	1.45	7.62
4	1.40	3.78
5	1.38	1.77
6	1.35	0.79
7	1.34	0.34

Table 2.4: Minimum gravitational radius, $(r_g)_{\min}$ and minimum mass, $m_{\min}$ for $\sqrt{\theta}M_D = 0.6$. From Ref. [14].

From Table 2.4, we can deduce the following:

1. For $n \leq 2$, the minimum mass is above the 14 TeV LHC energy reach.

2. For $n \geq 6$, the minimum mass is below the Planck scale.

3. For $3 \leq n \leq 5$, the minimum mass is within the 14 TeV LHC energy reach.

The choice of $M_D = 0.94$ TeV used at the time this research began is low compared to the current $M_D = 2.89$ TeV [13] limit for a number of dimension, $n = 4$.

2.D.2 Black Hole Decay

Noncommutative inspired black holes have minimum mass after decaying. This mass is taken to be the remnant of the black hole [14]. Several quantum gravity models predict that the remnant mass is at the Planck scale. In the case of noncommutative model, this is not the case due to the fact that remnants have a mass above the Planck scale.

It should be noted that black holes in remnant models will be produced predominantly just above the remnant mass, since black holes are predominantly created in proton-proton collisions near the mass threshold.

In this model, only black holes that Hawking evaporate are considered. Therefore, we only expect the decay to be a function of temperature. The noncommutative inspired black hole temperature is derived in Ref. [15] and it is expressed as [14]

$$T = \frac{n+1}{4\pi r_g M_D} \left[1 - \frac{2q^{(n+3)/2}e^{-q}}{F_n(q)(n+1)\Gamma(\frac{n+3}{2})} \right].$$
(2.26)

As the number of extra dimensions, n, increases so does the temperature as shown in Equation 2.25.

Chapter 3

The LHC and the ATLAS Detector

This chapter will briefly describe the Large Hadron Collider, which is a proton-proton accelerator designed to operate with a centre of mass energy up to 14 TeV, followed by a description of the ATLAS experiment which is one of four main detectors observing proton-proton collisions. And finally, this chapter will describe the ATLAS data acquisition and trigger system.

3.A   The Large Hadron Collider

The Large Hadron Collider is a gigantic particle accelerator, as a fact – the world's biggest machine, built in a circular tunnel 27 km in circumference at the European Centre for Nuclear Research (CERN) in Geneva, where it spans the border between Switzerland and France about 100 m underground as shown in Figure 3.1. It is used by physicists to study the smallest known particles – the fundamental building blocks of all things.
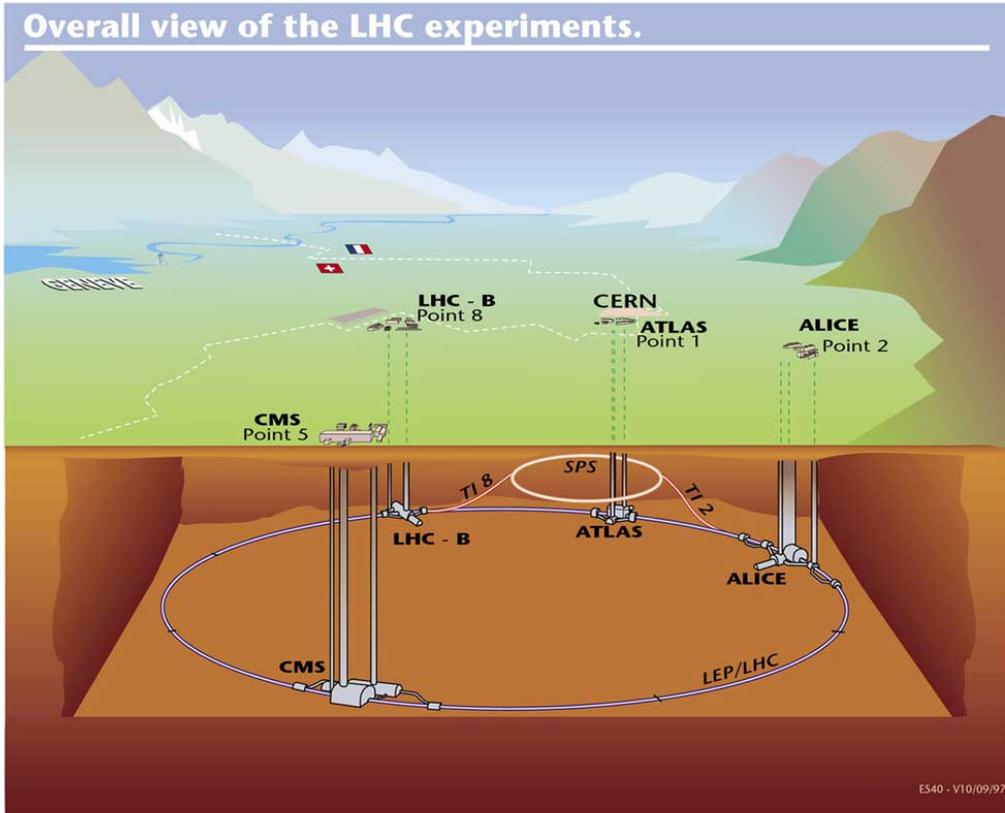
Figure 3.1: Overall view of the LHC experiments. From Ref. [16].

The LHC collides two beams of subatomic particles called hadrons (protons or lead ions) traveling in opposite directions inside the the circular accelerator at almost the speed of light (0.99999996c). The first beams were circulated successfully on 10th September 2008 [4].

There are many models that predict what new physics will be observed at the collider. For decades, the Standard Model of particle physics has served physicists well as a means of understanding the fundamental laws of nature. Only experimental data using the high energies reached by the LHC can push knowledge forward, challenging those who seek confirmation of established knowledge, and those who dare to dream beyond the paradigm.

In the first period of data taking 2010 and 2011, the protons inside the LHC ring were collided with a beam energy of 7 TeV (3.5 TeV per beam). The LHC collides protons at 8 TeV centre of mass energy (4 TeV per beam). This current collision energy started after the winter shutdown of 2012.

3.A.1 The LHC Injection System

In order to accelerate the protons up to the design beam energies, the LHC needs several pre-accelerators. Each of them is designed to increase the particle energy before sending the beam to the next accelerator. Figure 3.2 illustrates the accelerator structure that is used. First, a linear accelerator (LINAC2) ac-
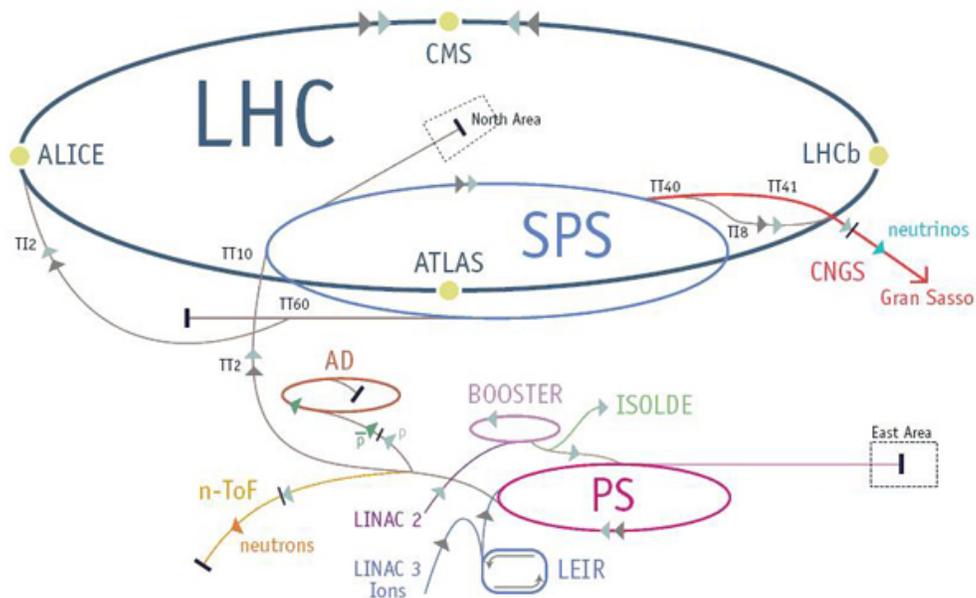
Figure 3.2: Schematic view of the LHC injection system [4].

celerates protons to 50 MeV. They are then sent to the booster, a synchrotron, that accelerates them to 1.4 GeV. The beam is then injected into the Proton Synchrotron (PS) that accelerates them to 25 GeV. Next the protons are sent

to the Super Proton Synchrotron (SPS) which provides acceleration to 450 GeV before the protons enter the 27 km long LHC tunnel [4]. Here the protons are accelerated to their final energy.

3.B The ATLAS Detector
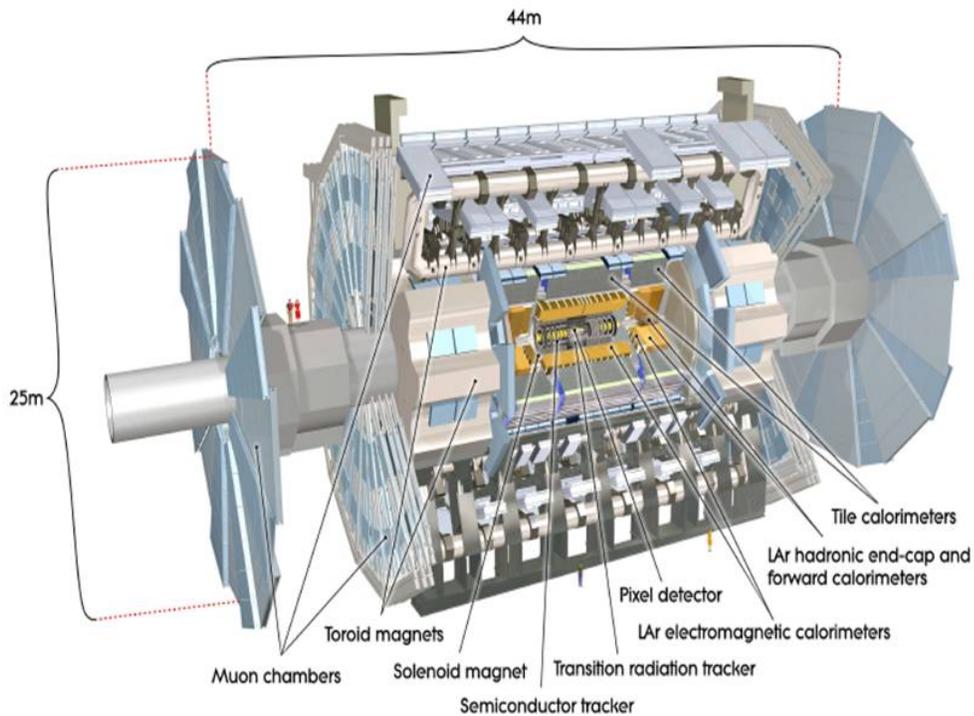
Figure 3.3: Cut-away view of the ATLAS detector. From Ref. [3].

ATLAS, which stands for A Toroidal LHC ApparatuS, is one of four general purpose experiments at the LHC. ATLAS is the largest particle physics detector ever assembled, with a length of 44 m and a diameter of 22 m; a diagram is shown in Figure 3.3. A computer-generated image, Figure 3.4 shows particles

interacting with various part of the ATLAS detector.
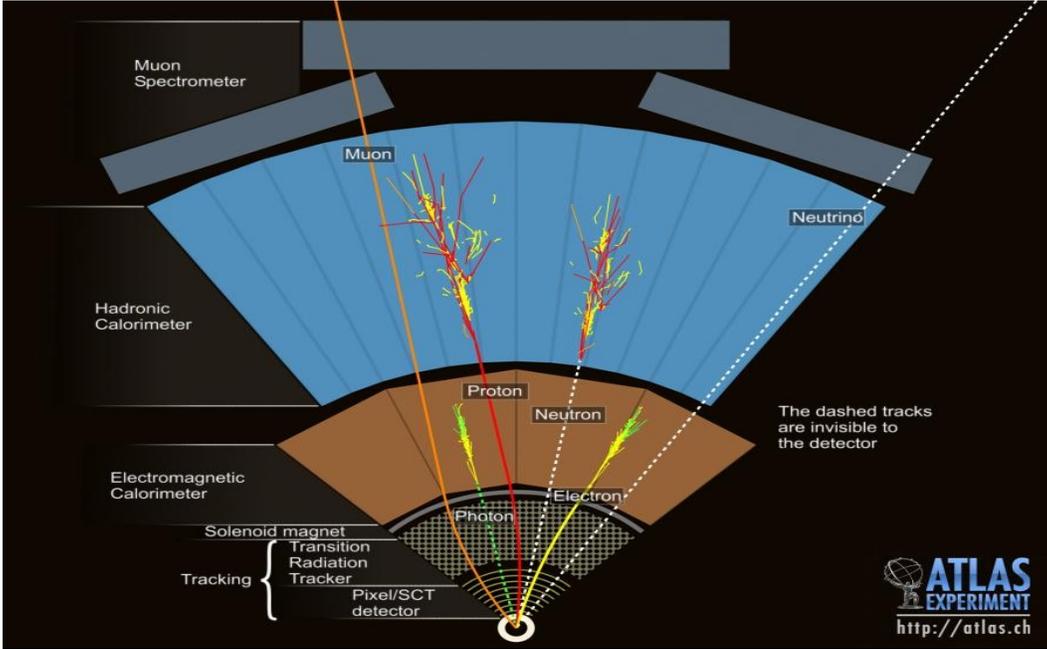
Figure 3.4: Event cross-section in a computer-generated image showing the tracking system, calorimeters, and muon spectrometers. From Ref. [17].

3.C   The ATLAS Coordinate System

The geometric layout of the ATLAS detector is a right handed coordinate system. The origin is placed at the nominal interaction point (IP) in the centre of the detector. The z-axis points along the beam pipe direction, and the distance perpendicular to it is R. The positive x-axis points towards the centre of the LHC ring and the positive y-axis points up towards the surface. The azimuthal angle (ϕ) is used as in spherical coordinates in the $x - y$ plane, and is defined as

$$\phi = \tan^{-1}\left(\frac{p_y}{p_x}\right), \tag{3.1}$$

where p_x and p_y are the x and y-components of the particle momentum. The pseudorapidity (η) is defined as

$$\eta = -\ln\left(\tan\left(\frac{\theta}{2}\right)\right), \tag{3.2}$$

where θ is the polar angle between the beam axis and the particle direction. For relativistic particles, the pseudorapidity is a good approximation of the rapidity, defined by

$$y = \frac{1}{2}\ln\left(\frac{E + p_L}{E - p_L}\right), \tag{3.3}$$

where E is the energy of the particles, and p_L is the momentum parallel to the beam axis. The transverse momentum, p_T is the momentum orthogonal to the beam direction,

$$p_T = \sqrt{p_x^2 + p_y^2} \ . \tag{3.4}$$

The missing transverse energy, E_T^{miss}, is the absolute value of the vectorial sum of all particle contributions to the transverse energies. It is computed from a weighted projection of all calorimeter cells onto the transverse plane.

3.D Luminosity

The luminosity, L, is a quantity in a proton-proton collider experiment which measures the rate of interactions. It has a unit of flux, $\text{cm}^{-2}\text{s}^{-1}$ (Hz/cm^2). The instantaneous luminosity is given by

$$\mathcal{L} = fn\frac{N_1 N_2}{A}, \tag{3.5}$$

where N_i is the number of particles in the bunches of the two beams which are brought to collision, f the revolution frequency and n the number of particle bunches in each of the beams. A is the cross-sectional area of the beams at the interaction point, which is expressed as $A = 4\sigma_x\sigma_y$. σ_x and σ_y characterize the horizontal and vertical profiles of the colliding beams.

The integral of the instantaneous luminosity, $\mathcal{L}$ over time gives the integrated luminosity

$$L = \int_{t_1}^{t_2} \mathcal{L}dt. \tag{3.6}$$

L represents the amount of data collected over a period of time. The number of events for a given scattering process in a given data sample, N is given by

$$N = \sigma L, \tag{3.7}$$

where σ is the cross section for the relevant scattering process.

3.E   Magnet System

The magnetic system of the ATLAS detector consists of the central solenoid and the air-core toroids [3]. Figure 3.5 shows the geometry of the magnets. Together they provide the ATLAS detector with the necessary magnetic field to bend charged tracks, making momentum measurements possible.

The central solenoid is located around the inner detector. Providing a magnetic solenoidal field to the inner detector with a magnetic field strength of 2 T. Thus, charged track are detected in the transverse plane, which enables the particle's transverse momentum, p_T to be measured in that direction. The inner (outer) diameter of the solenoid is 2.46 m (2.56 m). The total length of
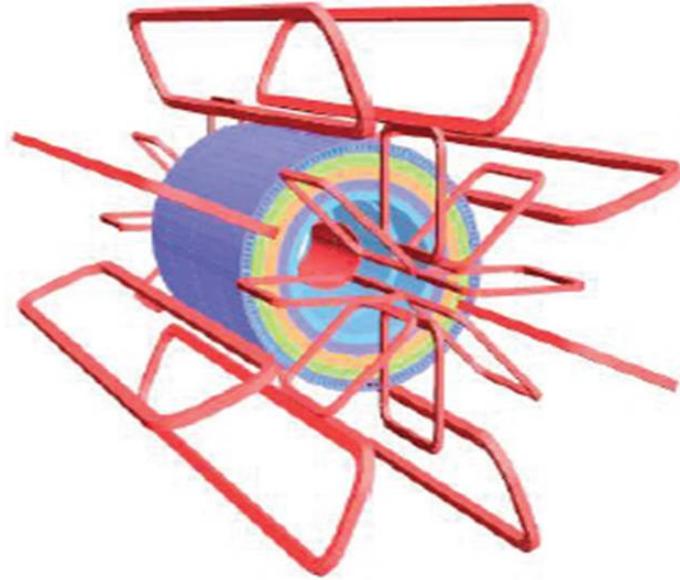
Figure 3.5: The magnet system in ATLAS. From Ref. [3].

the central solenoid is 5.8 m.

The air-core toroids are segmented into a barrel and two end caps. They are designed to detect muons in the $(R - z)$ plane. Each of the three toroids consists of eight coils, placed symmetrically around the beam axis. The central toroid provides a magnetic field of 0.5 T, while the end cap toroids provide a magnetic field of 1.0 T. The barrel has a length of 25.3 m, and has a inner (outer) diameter of 9.4 m (20.1 m).

3.F   Inner Detector

The Inner Detector (ID) [18] of ATLAS is designed to reconstruct tracks and vertices and to provide information for particle identification. Using a 2 T axial field it is possible to reconstruct tracks with a transverse momentum of

$p_T > 0.5$ GeV. Particles with a lower momentum have a too small bending radius and are therefore looping without escaping out of the inner detector with p_L. The inner detector comprises three sub-detectors as shown in Figure 3.6. Closest to the beam axis is the pixel detector, responsible for primary vertex reconstruction and determination of secondary vertices coming from long-lived particles. It is followed by the Semiconductor Tracker (SCT), used for high precision pattern recognition measurements. A pseudo-rapidity range of $|\eta| < 2.5$ is covered by these two detectors. The outermost sub-detector is the Transition Radiation Tracker (TRT). Covering a pseudo-rapidity range of $|\eta| < 2.0$, it enhances the pattern recognition range and additionally provides particle identification information.
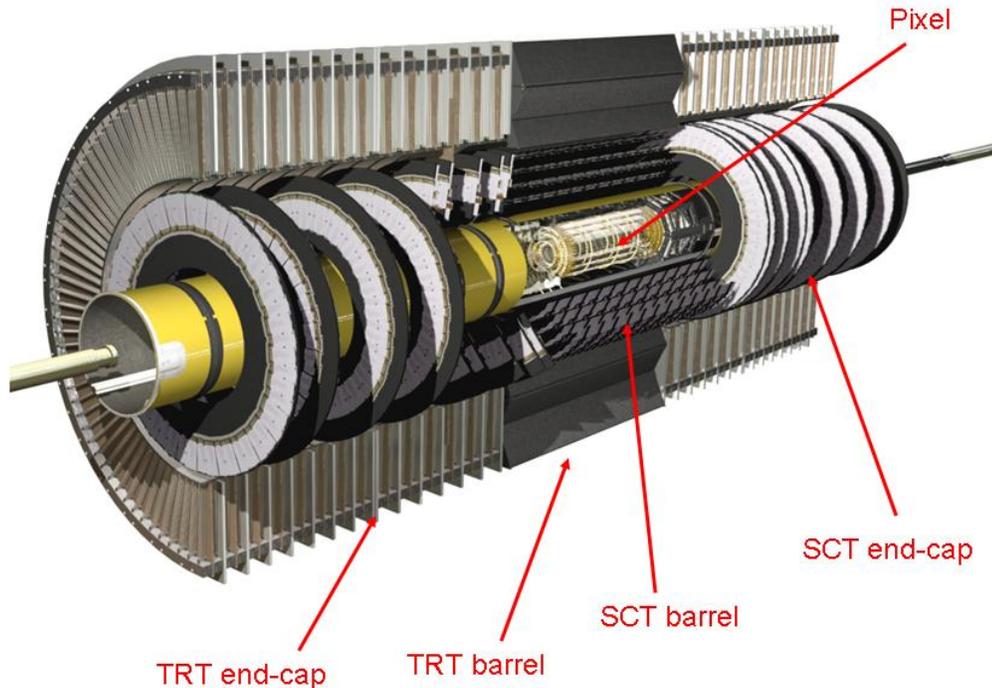
Figure 3.6: ATLAS Inner Detector. From Ref. [18].

3.F.1 Pixel Detector

A pixel sensor [19] is a 16.4×60.8 mm wafer of silicon with 46,080 pixels, 50×400 microns each. A pixel module comprises an assembly of sixteen front-end chips connected with high density bump bonding [20] techniques to the sensor. There are 1,744 modules in the pixel detector for nearly 80 million channels in a cylinder 1.4 m long, 0.5 m in diameter centred on the interaction point. The barrel part of the pixel detector consists of the three cylindrical layers with the radial positions of 50.5 mm, 88.5 mm and 122.5 mm respectively as shown in Figure 3.7. These three barrel layers are made of identical staves (axial strips) inclined with azimuthal angle of 20 degrees. There are 22, 38 and 52 staves in each of these layers respectively. Each stave is composed of thirteen pixel modules. In the module there are sixteen front-end (FE) chips and one Module Control Chip (MCC). One FE chip contains 160 straws and 18 columns of pixel cells, i.e. 2,889 pixels per FE chip or 46,080 pixels per module. There are three disks on each side of the forward regions. One disk is made of eight sectors, with six modules in each sector. Disk modules are identical to the barrel modules, except for the connecting cables. The front-end chips are a major heat source (0.8 Wcm^{-2}) dissipating more than 15 kW into the detector volume. This heat is taken out via integrated cooling channels in the detector support elements: Staves in the barrel region and sectors in the forward region.

3.F.2 The SemiConductor Tracker (SCT)

The Semiconductor Tracker (SCT) [21] is the intermediate sub-detector of the inner detector. It can provide four additional space points to a track, thus con-
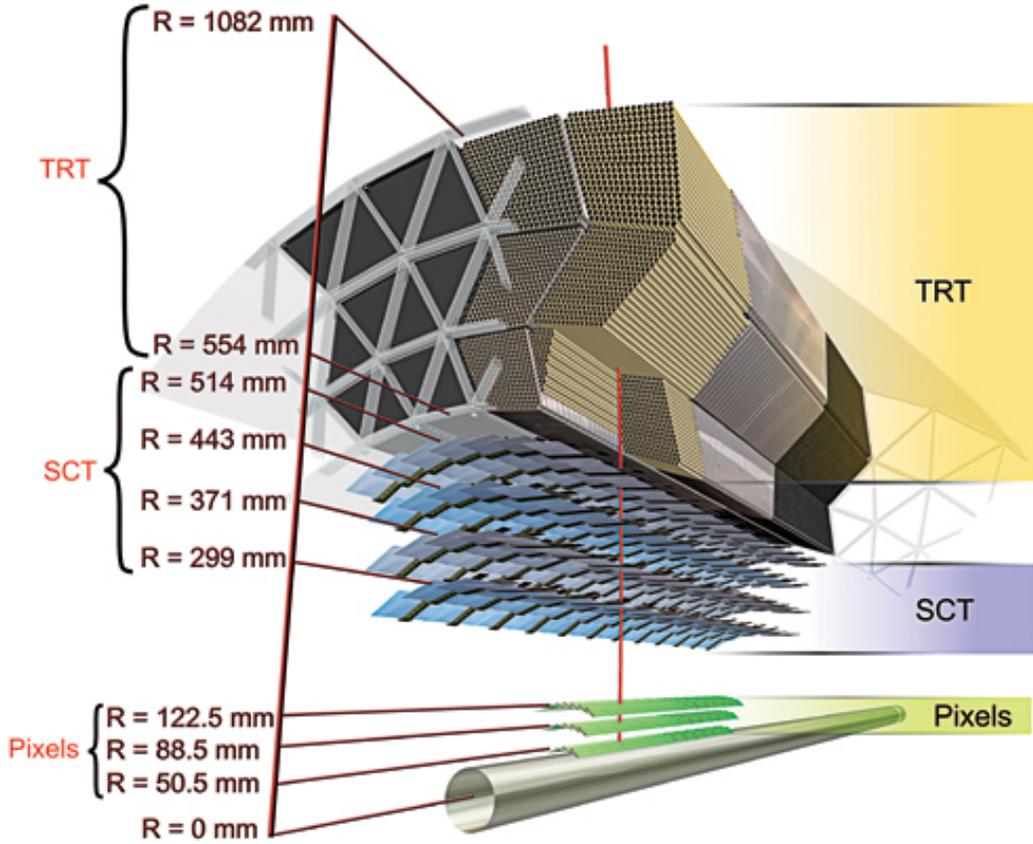
Figure 3.7: Detail of a cutaway view of the ATLAS inner detector. The detector is contained in the 2 T solenoidal magnetic field. Shown here is only the barrel region of the detectors. Each detector has two end caps organized as planar disks. From Ref. [3].

tributing to momentum, impact parameter and vertex position measurement. Due to its relatively high resolution it is also useful for pattern recognition (classifying vertices) . It is based on the same functional principle as the pixel detector, but is equipped with strips instead of pixels. The modules are build as stereo modules with two layers of strips, arranged with an angle of 40 mrad between the orientation of the layers. This provides information of the z (R) position in the barrel (endcap). The modules are installed in four concentric layers in the barrel and nine disks in both end-caps. One strip layer of each

stereo module is placed parallel to the beam axis in the barrel and radially in the end-caps. This ensures a proper measurement of the ϕ coordinate. The position resolution of the SCT is 17 μm in the $R-\phi$ $(z-\phi)$ plane and 580 μm in z (R) for the barrel (end-cap). In total, the silicon modules cover a surface of 63 m^2 and are readout via 6.3 million readout channels.

3.F.3   The Transition Radiation Tracker (TRT)

The Transition Radiation Tracker (TRT) [22] is the outermost sub-detector of the inner detector of ATLAS. It provides further space points for the track reconstruction and additionally a particle identification measure. It is built out of thin proportional drift tubes with a diameter of 4 mm. These straw tubes are filled with a xenon based gas mixture, and have a gold-plated tungsten wire in the centre as anode. An aluminum coating on the tube serves as cathode. As indicated by its name, the detector makes use of the transition radiation effect. A relativistic charged particle emits photons when it crosses the boundary of two materials with different dielectric constants. The radiated energy is linearly proportional to the Lorentz factor ($\gamma = E/m$, $m =$ mass of particle). Thus the TRT can not only be used to determine track points of the charged particle but especially to distinguish between electrons and heavier particles. In the barrel 52,544 straw tubes are arranged in 73 layers parallel to the beam axis. In the end-caps 160 layers comprise 122,880 tubes, which are oriented radially around the beam axis. The space between successive layers is filled with polypropylene foil acting as radiator. A large number of space points per track can be expected from this detectors. The chosen geometry ensures at least 36 hits for a traversing charged particle with $p_T > 0.5$ GeV.

The barrel TRT only provides a $R - \phi$ measurement, with an intrinsic accuracy of 130 μm per straw tube.

3.G   Calorimetry

The purpose of calorimetry is to provide both an energy measurement and directional information about the measured energy deposition. Furthermore it allows the determination of missing transverse energy due to its large coverage in pseudo-rapidity while limiting so called punch-throughs from non-minimum ionizing particles to the muon system. The calorimetry of ATLAS is divided into an electromagnetic part, dedicated to the measurement of electrons and photons, and a hadronic part, optimized for jet reconstruction and missing transverse energy measurements. The general layout of the ATLAS calorimetry is shown in Figure 3.8, Ref. [23].

3.G.1   Electromagnetic Calorimeter

The Electromagnetic Calorimeter (ECAL) [23] is a lead-liquid argon (LAr) sampling calorimeter with accordion geometry covering the region $|\eta| < 3.2$. It has a slightly complex geometry which is shown in Figure 3.9 and provides complete ϕ symmetry without azimuthal cracks. There is, however, a crack at $|\eta| = 1.5$ where the barrel to end-cap transition occurs and a small crack at $\eta = 0$. In order to provide good particle identification (via shower shape) and shower direction, the ECAL has three longitudinal sections, samplings, with high granularity which allows for excellent π^0/γ and e/π separation. The ECAL has a thickness of at least 24 X_0 in the barrel and 26 X_0 to an acceptable level. X_0 is the radiation length. As a sampling calorimeter, its performance
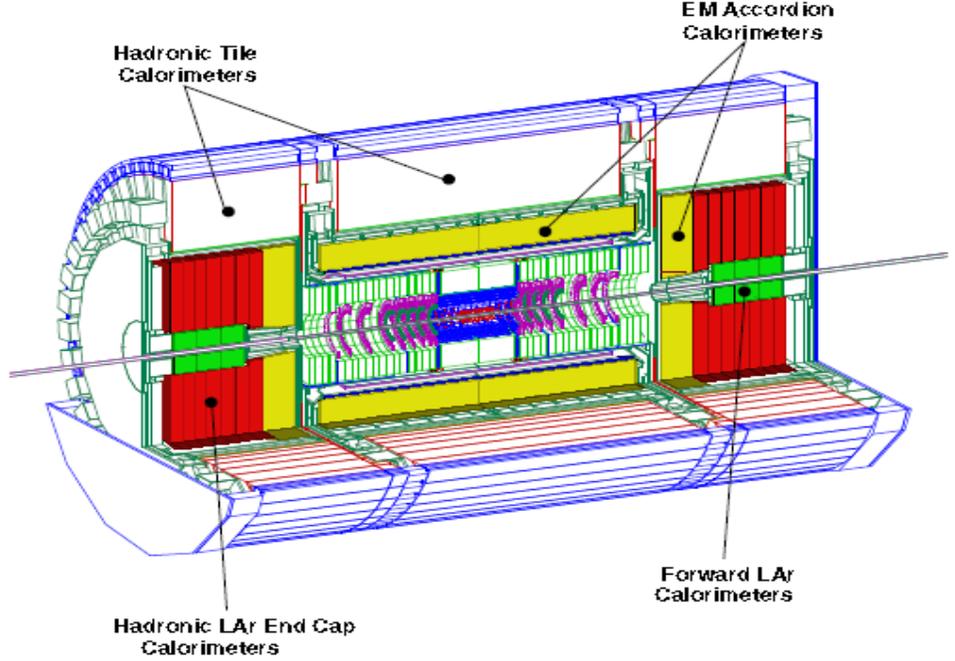
Figure 3.8: Schematic view of the ATLAS calorimeter system. From Ref. [23].

is dominated by sampling fluctuations giving

$$\frac{\sigma_E}{E} = \frac{10\%}{\sqrt{E}} \oplus 0.5\% \tag{3.8}$$

for electrons at $\eta = 0.3$ [23], where E is in units of GeV, σ_E is the uncertainty in the measurement of the calorimeter energy, and $\oplus$ stands for the quadratic sum, $x \oplus y = \sqrt{x^2 + y^2}$. Test beam results of the EM barrel and the end-cap give a combined resolution for the electromagnetic calorimeter of

$$\frac{\sigma_E}{E} = \frac{10\%}{\sqrt{E}} \oplus \frac{0.4}{E} \oplus 0.7\%, \tag{3.9}$$

35
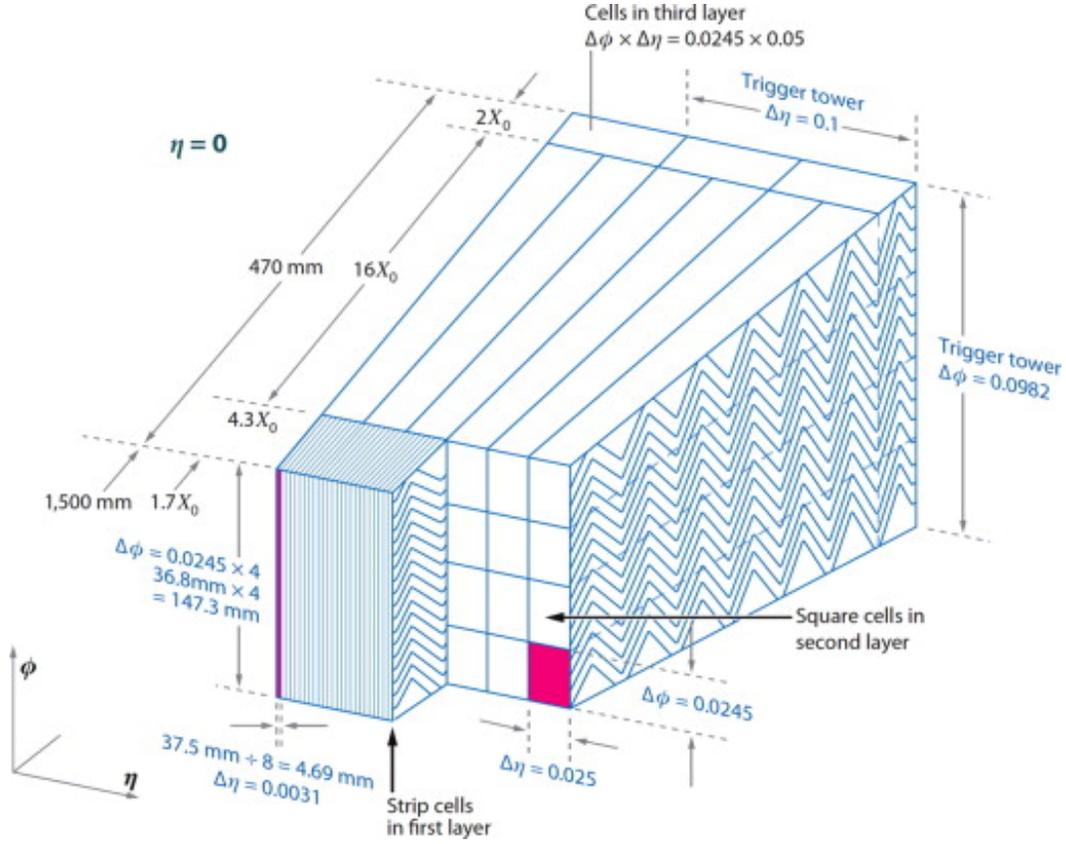
Figure 3.9: Geometry of the electromagnetic calorimeter. From Ref. [23].

the first term is the statistical uncertainty due to the total number of particles in the showers, and the second term is the electronics noise, and the third term is the calibration uncertainty.

3.G.2   Hadronic Calorimeter

The hadronic calorimeter [24] covers a pseudo-rapidity range of $|\eta| < 4.9$ and uses two different techniques. The barrel region is equipped with a tile calorimeter, while the end-cap and forward regions are based on tungsten-liquid-argon technology. The tile calorimeter is divided into a central barrel and two extended barrels, and subdivided in three layers in the radial depth.

It uses steel as absorber and scintillating plates, referred to as tiles, as active medium. An ionizing particle crossing a tile produces ultraviolet light, which is transformed to visible blue light by scintillating additives. The edges of the tile are equipped with wavelength shifting fibres, which collect the light and guide it to two photo multiplier tubes (PMTs). Several tiles are grouped to certain PMTs, forming cells with a size in $\Delta\eta \times \Delta\phi$ of 0.1×0.1 for the inner two layers and 0.2×0.1 for the outer layer. The thickness of the three layers corresponds to 1.5, 4.1 and 1.8 interaction lengths (λ_{int}) from inside to outside at $\eta = 0$. Between the central and the extended barrel is a gap of about 70 cm, mainly used for cabling and services for the sub-detectors closer to the interaction point. This only partially instrumented region is expected to perform poorer compared to the rest of the tile calorimeter. The number of readout channels for the tile calorimeter is about 10,000.

The two hadronic end-cap calorimeters use copper plates as absorbers and liquid argon as active medium. Each end-cap consists of two wheels placed concentrically around the beam axis. Each wheel is constructed from 32 identical modules and is divided into two longitudinal readout segments. Each hadronic end-cap calorimeter provides 5,632 readout channels and has an active part corresponding to approximately $12\lambda_{\text{int}}$.

The two Forward Calorimeters (FCALs) are placed at high $|\eta|$, and are therefore exposed to a high level of radiation. Each FCAL is divided into three 45 cm deep modules, see Figure 3.10. The outer two modules are made of tungsten and have the purpose of measuring mainly hadronic interactions. Compared to the other ATLAS liquid argon calorimeters the design is much denser. Each forward calorimeter has a depth of approximately $10\lambda_{\text{int}}$ and provides 1,762 readout channels.
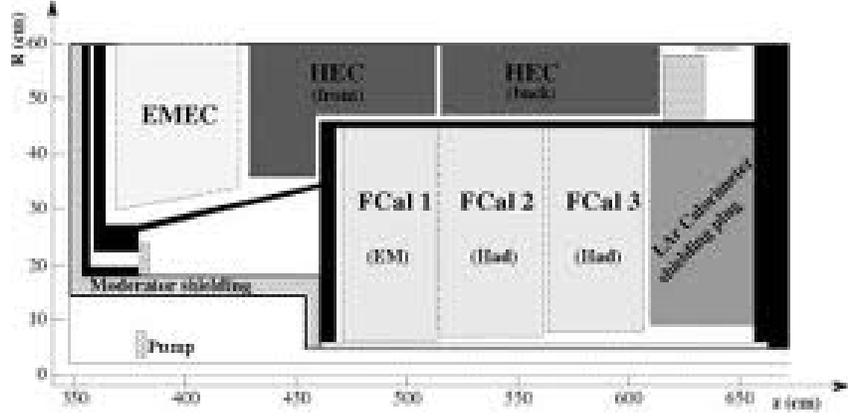
Figure 3.10: Schematic view of the forward calorimeter. From Ref. [23].

3.H   Muon Spectrometer

The muon spectrometer is designed to measure the momentum of high energy muons (low energy muons will be measured by the inner detector) and to trigger on them. These considerations, the large size of the spectrometer and cost, necessitate the use of several different detection technologies. Figure 3.11 gives an overview of the layout of the muon system. The two main detectors are the monitored drift tubes (MDTs) which are used for precision measurements and the resistive plate chambers (RPCs) which are used for triggering. At high $|\eta|$, cathode strip chambers (CSCs) and thin gap chambers (TGCs) are used for these tasks. Ref. [25] provides further details on this.
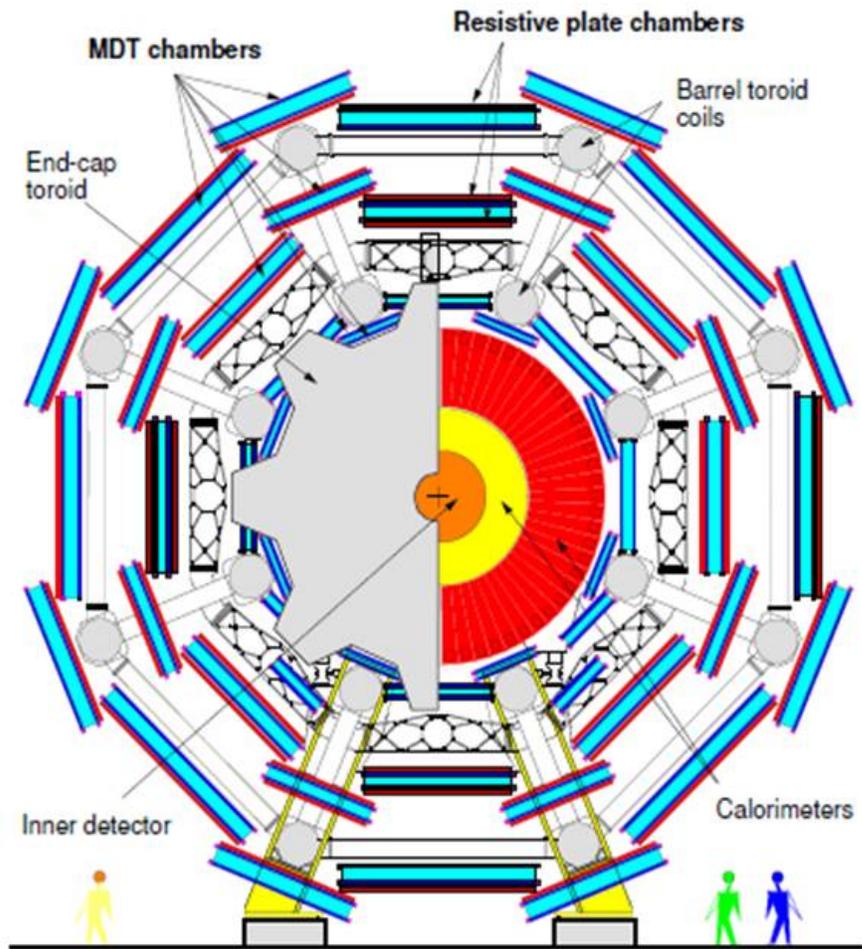
Figure 3.11: End view of the muon spectrometer. From Ref. [25].

The MDTs are 30 mm diameter drift tubes arranged into units called cham-
bers. These incorporate a novel optical monitoring system (providing the M in
the name) to measure any physical deformations. The single-wire resolution
is expected to be 80 μm. The MDTs are arranged to be at approximately
constant η.

The drift time in the MDTs is longer than the 25 ns event time, so they

cannot be used for triggering. Instead RPCs are used which provide a space-time resolution of 1 cm $\times$ 1 ns. An RPC is a pair of parallel plates separated by a narrow gas gap with a high electric field. Primary ionization electrons from the passage of muons cause an avalanche between the plates. The signal is read out by two sets of strips in orthogonal directions. These measurements are used in the Level-1 trigger and also to provide a measurement in the orthogonal direction to the MDTs.

The muon spectrometer should provide three precision measurements over the range $|\eta| < 2.7$ (triggering for $|\eta| < 2.4$) except where there are cracks (most notably at $\eta = 0$ where there is a large crack for cabling). This allows the muon momentum to be measured to 2% at 20 GeV with good acceptance. At 1 TeV the momentum can be measured to 10% although the acceptance is rather low (50%), but rises to nearly 90% for a 20% momentum measurement.

3.I   Data Acquisition and Trigger System

The design luminosity of 10^{34} cm^{-2}s^{-1} corresponds to approximately an interaction rate of 1 GHz. The luminosity of the data used for this research is 1.27×10^{33} cm^{-2}s^{-1} (runnumber $= 182726 - 183462$) which corresponds to a rate of 127 MHz. This is a huge amount of data, that needs to be reduced to a rate of 200 events per second. The trigger consists of three levels of online event selection, the Level-1 trigger (L1), Level-2 trigger (L2) and Event Filter (EF). The Level-2 trigger and the Event Filter together make up the High-Level Trigger (HLT). Figure 3.12 shows the ATLAS trigger system, indicating the rate, and latency (time taken by a signal to travel through a circuit to reach its intended destination) for each trigger level.
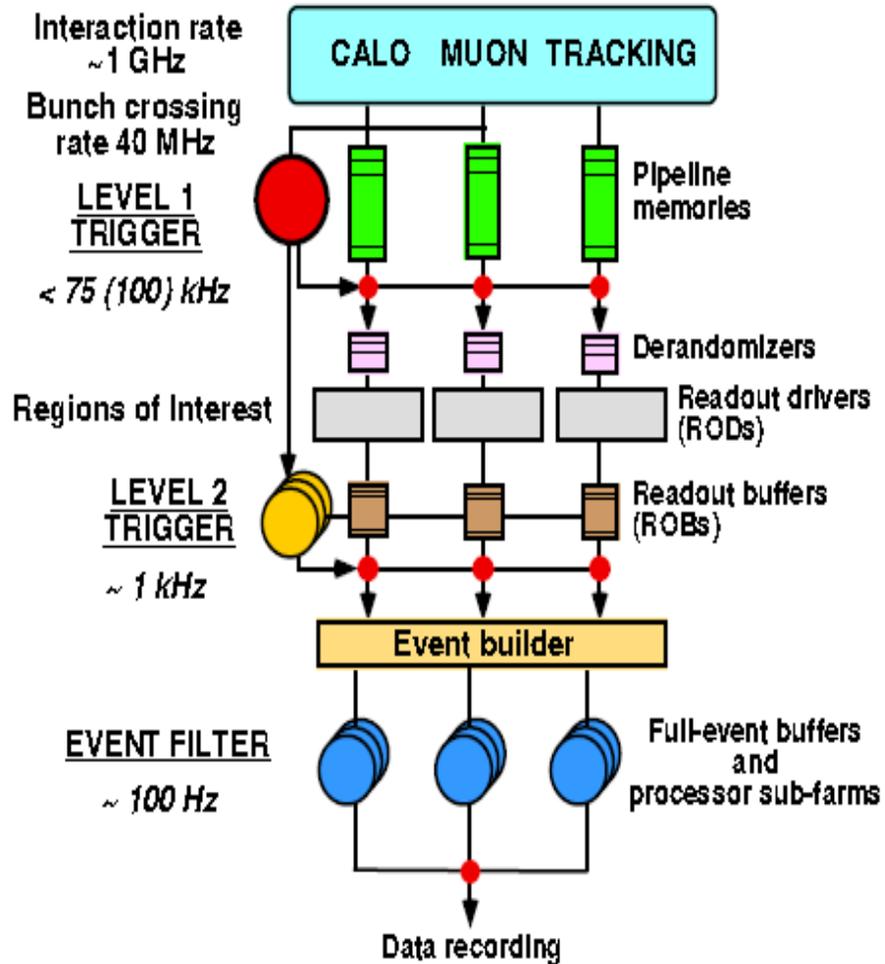
Figure 3.12: Trigger overview. From Ref. [26].

The Level-1 trigger is based on the information provided by a subset of the detectors. It searches for signatures from high-p_T muons, photons, electrons, jets and taus decaying to hadrons. It also searches for large missing energy and large total transverse energy. For the muon momentum identification, it uses the muon trigger system. It also uses information of all the calorimeters, to identify electromagnetic clusters, jets, τ-leptons, missing transverse energy

and total transverse energy. Events that pass the Level-1 trigger will define Regions of Interest (RoIs) and the information is sent to the Level-2 trigger. The RoIs are characterized by their coordinates in η and ϕ. The Level-1 trigger accept rate is 75 kHz, with a design latency of 2.5 μs.

The Level-2 trigger receives the RoIs from the Level-1 trigger. It uses the full granularity and precision of all the data, including the inner detector, to further reduce the amount of data. It uses the information from the inner detector to confirm track and energy clusters found in the Level-1 trigger. The Level-2 trigger is designed to reduce the trigger rate to approximately 3.5 kHz, with processing time of 40 ms.

The Event Filter is the last stage in the online selection, and it will decide which events will go to permanent storage. The Event Filter reduces the trigger rate further, to approximately 200 Hz, with a processing time of 4 s. Once an event is selected by the event filter it will be send to permanent storage, and is available for future physics analysis. The average event size is 1.3 MB.

Chapter 4

ATLAS Analysis Software

This chapter will describe the ATLAS software used to carry out the data analysis. The ATLAS offline software aims to reconstruct and help analyze the processed data by the ATLAS trigger and data acquisition system described in Section 3.I.

In order to find interesting signals for new physics in ATLAS, the ATLAS software must be able to support analysis of recorded events from the ATLAS detector (experiment) as well as simulated events from a Monte Carlo (MC) event generator throughout the experiment operational lifetime.

Hence, the ATLAS software group provides and develops a common event processing framework called the Athena framework, which is written mainly in the C++ programming language with various supporting components and interfaces via Python scripts. The Athena framework is being used by the ATLAS collaboration as the main tool for data analysis.

4.A   ATHENA Framework

Athena is the common software framework for the ATLAS experiment [4]. It is based on the Gaudi framework, which was originally developed by LHCb, but presently it is a common kernel of software for both the ATLAS and the LHCb experiments, with Athena including some ATLAS specific program enhancements. All levels of data processing [27] (Figure 4.1) in the ATLAS experiment are done in the Athena framework [28], that includes software for example for event simulation, event trigger, event reconstruction, and physics analysis tools.

4.A.1   Event Generation

The generation of events is the first step of the event simulation and reconstruction in the ATHENA framework. Before the LHC became operational, all of the physics studies were done by simulated events of proton-proton collision. At present, there are several popular event generators e.g., HERWIG [29], PYTHIA [30], ALPGEN [31], CHARYBDIS [32], and so on. These generators can be run inside of ATHENA individually.

4.A.2   HepMC (High Energy Physics Monte Carlo)

HepMC is an object-oriented event record written in C++ for Monte Carlo event generators. Generated event data from event generation are mapped into HepMC as a common format in the StoreGate (the ATLAS transient data store). Now, the recorded events are sent to G4ATLAS simulation after a particle filtering. These data objects containing Monte Carlo truth information are read by G4ATLAS simulation based mainly on Geant4 [33].
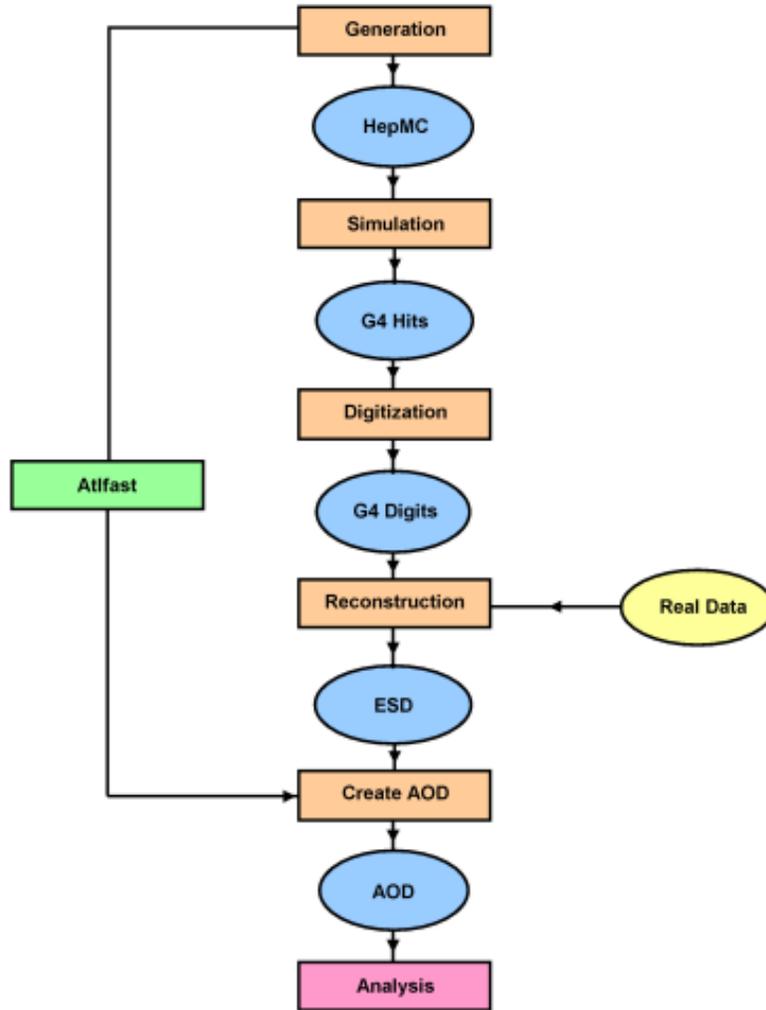
Figure 4.1: Schematic representation of the full chain Monte Carlo production. From Ref. [27].

4.A.3 Simulation

In recent years, a huge amount of effort on improving the Geant4 simulation has been carried out in order to provide the modeling of hadronic physics processes. The Geant4 toolkits allows us to build the virtual ATLAS detector with specific descriptions of materials.

4.A.4 Digitization

G4ATLAS simulates physics processes in the ATLAS detector, so it reads out the hits which include energy, position, and interaction information. The produced hits will correspond to the readout electronics and the propagation of charges or light into the media. Thus, the stage of digitization requires detailed detector knowledge. At the end of this step, Raw Data Objects (RDOs) are produced which pass the event filter of the high level trigger (HLT) for reconstruction. The RDOs are similar to the real detector data. The most important role of this step is that one can compare the RDO output to real data to test the detector response of experiment.

4.A.5 Reconstruction

Reconstruction from simulated data (see Section 6.C for reconstruction of real data) is an essential part of this work because it enables one to reconstruct MC signal events for physics analysis. Reconstruction plays the role of deriving particle kinematics (energy, transverse momentum, etc.) and information for physical objects such as muons, electrons, photons, tau-leptons, jets, missing transverse energy, and primary vertex.

4.A.6 ESD

The ESD (Event Summary Data) contains detailed output from the reconstruction to re-run track re-fitting, jet calibration, and the first stage of particle identification. Thus, it is good for tuning of reconstruction algorithms and calibrations of the ATLAS experiment for real data. However, it does not allow to fully re-run pattern recognition from the inner detector clusters

or recalibration of all the calorimeter cells because the ESD is designed to compactify the largest objects.

The Analysis Object Data (AOD) is produced from the ESD via the AOD builders and it contains the necessary information to satisfy the requirements for further analysis. The AOD contains a summary of the reconstructed event from the ESD. Therefore, the size of the AOD file is much smaller than the ESD files.

DPD (Derived Physics Data) is derived from AOD (Analysis Object Data) on which the end user can perform physics analyses on. They are ntuple style representations that can be used easily with analysis tools such as ROOT (see subsequent section, 4.B). The analysis in this thesis is performed on ntuple files.

4.B   ROOT

ROOT is an object-oriented analysis program developed at CERN for all high energy particle physics experiments. It has a built-in C++ interpreter (CINT). This allows the user to run small C++ programs, without being compiled. ROOT is designed to handle large amounts of data in a very efficient way and it provides a large amount of analysis package tools such as:

1. histogramming and graphing to view and analyze distributions and functions,

2. curve fitting (regression analysis) and minimization of functionals,

3. statistics tools used for data analysis,

4. matrix algebra,

5. four-vector computations, as used in high energy physics,

6. standard mathematical functions, etc.

4.C Data and Monte Carlo Samples

The data used in this analysis were collected at the LHC operating at a centre of mass energy of 7 TeV. The total integrated luminosity after detector and data-quality requirement (bad runs) is $316\,\mathrm{pb}^{-1}$, with an uncertainty of 1.8% [34]. The data were recorded with a missing energy trigger with the threshold at 60 GeV (cf. Chapter 5) on the missing transverse energy. The trigger efficiency reaches a plateau regime for missing transverse energy above 140 GeV (cf. Chapter 5).

Monte Carlo samples are used both for signal modeling and background estimation. These samples are processed with the ATLAS full detector simulation [35] which is based on the GEANT4. The simulated events are then reconstructed with the same software chain as the data.

Background Monte Carlo samples were generated for QCD processes with PHYTHIA, using the MRST2007LO* modified leading-order parton distribution functions (PDF) [36], The $t\bar{t}$ events were generated with MC@NLO [37] with top-quark mass of 173.2 GeV [38], and with the next-to-leading order (NLO) PDF set CTEQ6L1 [39]. The W+jets and Z+jets Monte Carlo events were produced with ALPGEN, using the CTEQ6L1 PDFs. Fragmentation and hadronisation for the ALPGEN and MC@NLO samples were performed with HERWIG using JIMMY [40] for the underlying events. These Monte Carlo samples were produced using a specific ATLAS parameter tune [41] depending on the event generator.

Signal Monte Carlo sample were generated using modified CHARYBDIS2 [14]. The shower evolution and hadronisation uses PYTHIA. The samples were produced with the CTEQ6L1 PDF set with the radius of the black hole used as the QCD scale, $Q = 1/r_g$. For the signal sample, $M_D = 0.94$ TeV and the black hole remnant mass threshold, $M_{\mathrm{min}} = 3.6$ TeV is for a case of 4 extra dimensions. The resulting black mass ranges from this threshold to the maximum black hole mass, $\sqrt{s} = 7$ TeV.

Chapter 5

Trigger Analysis

All ATLAS events have to be selected by the trigger system before they are recorded for offline study. There are three levels in the trigger system as mentioned in Section 3.H.

5.A Trigger Nomenclature

In this thesis, trigger chains will be referred to by giving their official names as they appear in the trigger menu. These names are composed according to the following conventions. The general structure of the trigger names is:

(Trigger Level)_(Multiplicity if > 1)(Threshold Type)(Threshold Value)_(Postfix)

The prefix indicating the trigger level is always L1, L2 or EF, followed by an underscore. For triggers which require a multiplicity of trigger objects larger than 1, the multiplicity is then given in front of the threshold type. The threshold type is an abbreviation stating the type of the trigger. The most important abbreviations for object triggers are e for electrons, g for photons, mu for muons, tau for tau leptons, j for jets and fj for forward jets. Triggers which use global quantities have mb for minimum bias, rd for random triggers, ht for the sum of the transverse energy, je for

the total energy in jets, xe for the missing transverse energy, E_T^{miss}. In addition, at Level 1, there is EM, standing for the item triggering on electron/photon objects, which cannot be distinguished at L1. Threshold type and value may appear several times for combined triggers.

The names for L1 items always consist only of uppercase letters, whereas for L2 and EF usually lowercase letters are used, but here the postfixes may vary. An important postfix of the chain studied here is *noMu*, which is common to all configured missing energy trigger chains at L2 and EF and says that no muon contributions are taken into account in the trigger decision.

Some examples for illustration are:

1. L1_MU20 = L1 muon trigger item, requiring a muon with a p_T of at least 20 GeV.

2. L2_j45_xe20_noMu = jet + E_T^{miss} trigger at L2, requiring a jet with at least 45 GeV and E_T^{miss} of at least 20 GeV excluding muon contributions.

3. EF_j55_a4tc_EFFS = EF jet trigger item, requiring a jet with anti-k_t R = 0.4 (R = distance parameter) and p_T of at least 55 GeV with full scanning at EF (EFFS = Event Filter Full Scan).

4. EF_xe30_loose_noMu = E_T^{miss} trigger, requiring at least 30 GeV of missing transverse energy at EF, which has looser thresholds at L1 and / or L2.

We have selected a high level E_T^{miss} trigger, EF_xe60_noMu for this thesis. Table 5.1 shows the acceptance for the various datasets used for this thesis. These acceptances are the ratio of events that passed the trigger to the number of events in the sample,

$$\text{acceptance} = \frac{\text{Number of events passing trigger}}{\text{Total number of events in sample}} \times 100\%. \tag{5.1}$$

Process	$t\bar{t}$	W+jets	Z+jets	QCD dijet	Black Hole	Data
Acceptance (%)	1.7	9.2	8.5	20.8	55.0	3.8

Table 5.1: Acceptance for MC simulated Standard Model backgrounds, data and black hole events using EF_xe60_noMu trigger.

5.B   Efficiency Estimation

The basic principle of the computation of a trigger efficiency is selecting the number of occurrences in which the trigger could have fired (the denominator of the efficiency estimate n), and the number of occurrences in which it actually did (the numerator m), both as a function of the offline variable which are used to parametrize the trigger efficiency. The ratio of the counts is used as the estimator of the trigger efficiency,

$$\epsilon = \frac{m}{n},$$
(5.2)

where m obviously depends on n. The counting is usually done using two 1–dimensional histograms with an appropriate binning in the relevant offline variable.

The next stage of this analysis is to plot an efficiency histogram using our datasets to determine the fully efficient region of this trigger, which will further be applied in our subsequent analysis. ATLAS data and Monte Carlo (MC) datasets are employed for this purpose. We chose EF_xe20_noMu and EF_j55_a4tc_EFFS as our reference trigger for this exercise. A low threshold value trigger (EF_xe20_noMu and EF_j55_a4tc_EFFS) is usually used as a reference trigger for the purpose of efficiency estimation.

The efficiency histogram below was achieved using Equation 5.1. For the data and QCD dijet sample (contribution of events that are dominated by the strong

interactions), the equation becomes,

$$\epsilon_{\text{Data(QCD)}} = \frac{(\text{EF\_j55\_a4tc\_EFFS}) \bigcap (\text{EF\_xe60\_noMu})}{\text{EF\_j55\_a4tc\_EFFS}}, \qquad (5.3)$$

where $\bigcap$ stands for intersection. While for $t\bar{t}$, W+jets, Z+jets and black hole, Equation 5.1 becomes,

$$\epsilon = \frac{(\text{EF\_xe20\_noMu}) \bigcap (\text{EF\_xe60\_noMu})}{\text{EF\_xe20\_noMu}}. \qquad (5.4)$$

Different formulas were applied for the purpose of calculating the efficiency because some trigger variables were missing in some datasets.
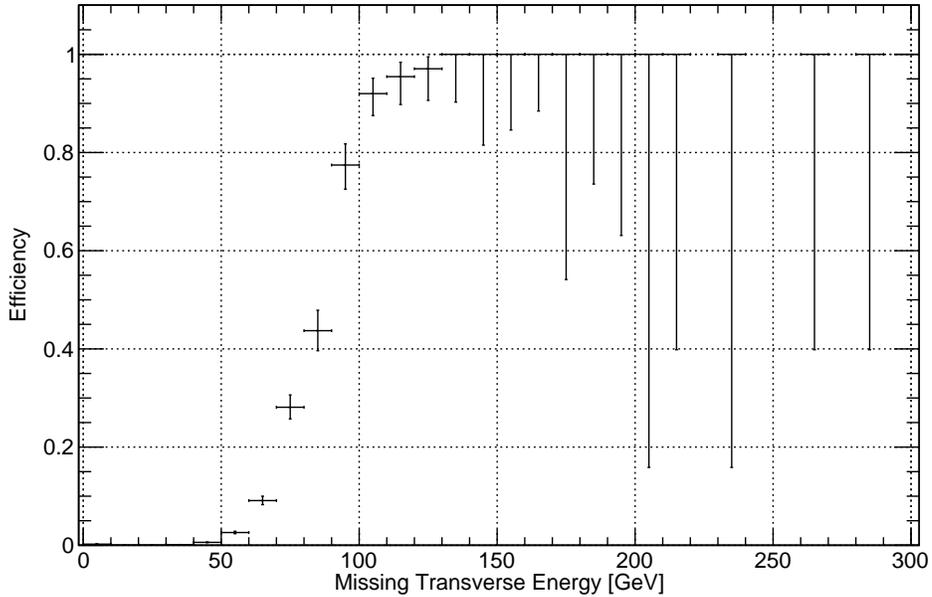
Figure 5.1: Efficiency plot for EF_xe60_noMu trigger using ATLAS data.

Shown in Figure 5.1, the trigger appears to be 100% efficient, with large error, at a missing transverse energy of at least 140 GeV. Hence, we use this value as one of our analysis selection criteria for our black hole search.

Also shown are efficiency plots for the Monte Carlo background samples used

for this work. The background Monte Carlo samples show the following efficiency values: the QCD (Figure 5.2) shows an 88% trigger efficiency, the black hole signal (Figure 5.3) shows about 96% efficiency, the $t\bar{t}$ (Figure 5.4) shows about 90% efficiency, the $W + \text{jets}$ (Figure 5.5) shows about 97% efficiency and the $Z + \text{jets}$ (Figure 5.6) shows about 90% efficiency.

Since the MC simulated efficiency is not 100%, the inefficiency is compensated in the calculation of the number of events.
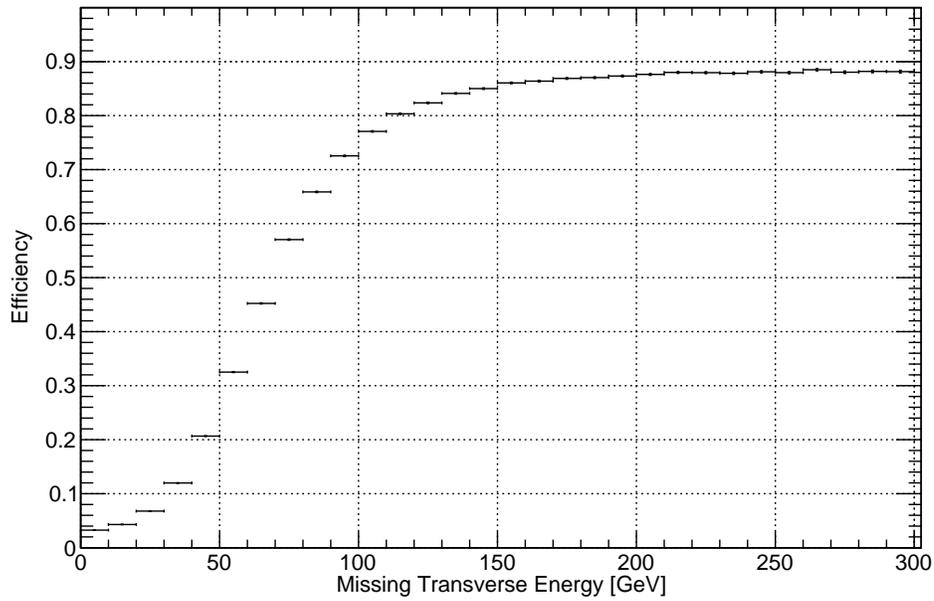
Figure 5.2: Efficiency plot for EF_xe60_noMu trigger using QCD dijet samples.
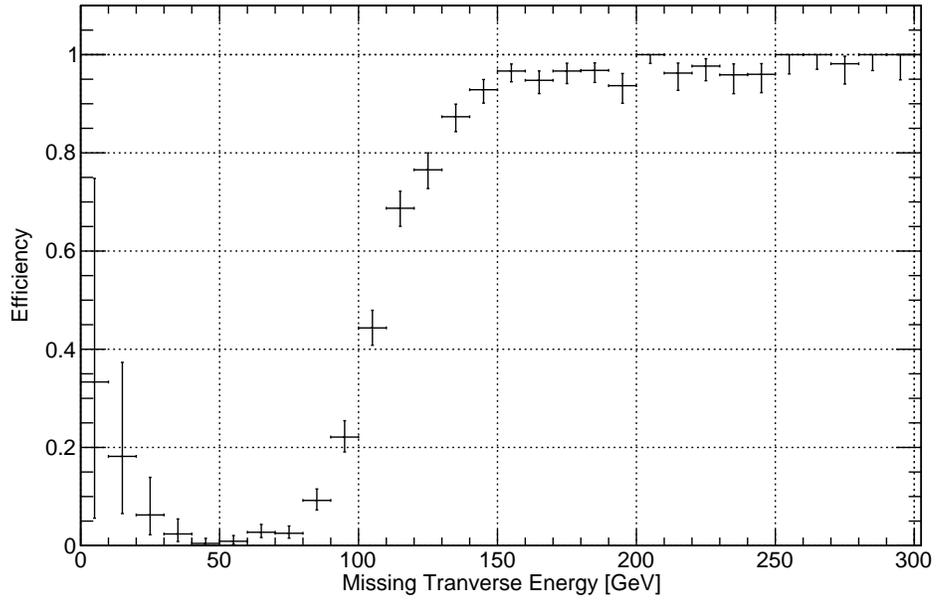
Figure 5.3: Efficiency plot for EF_xe60_noMu trigger using black hole sample.
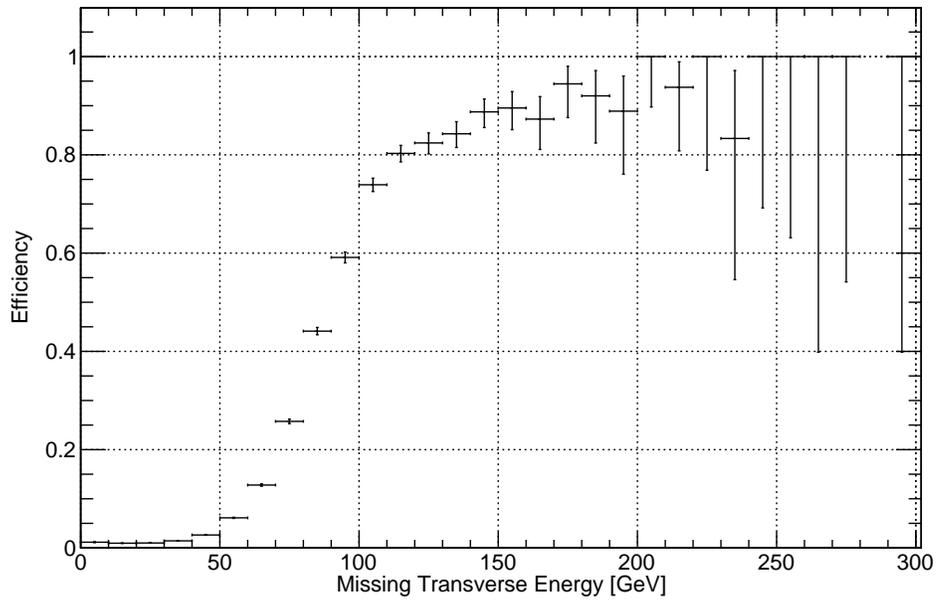
Figure 5.4: Efficiency plot for EF_xe60_noMu trigger using $t\bar{t}$ sample.

55
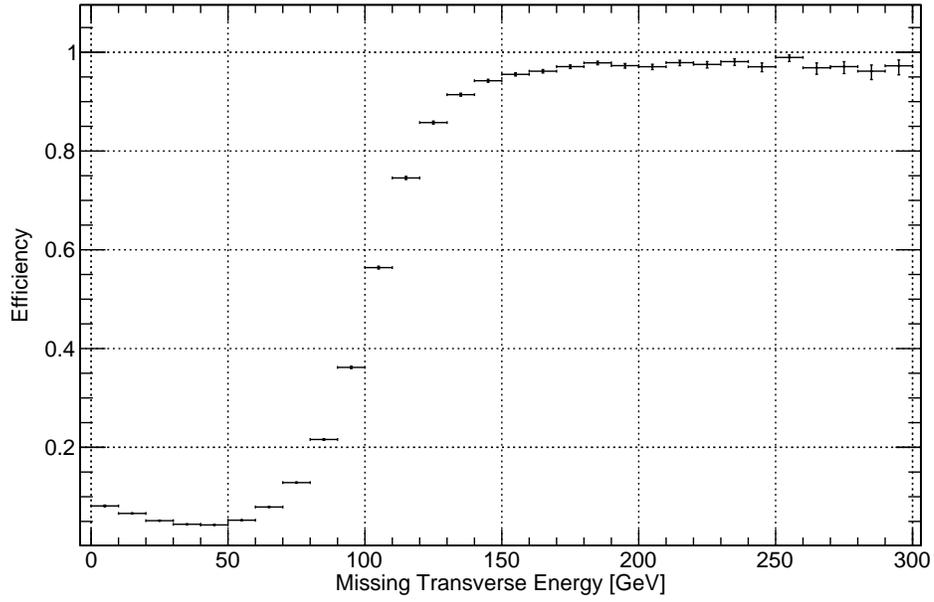
Figure 5.5: Efficiency plot for EF_xe60_noMu trigger using $W + $ jets sample.
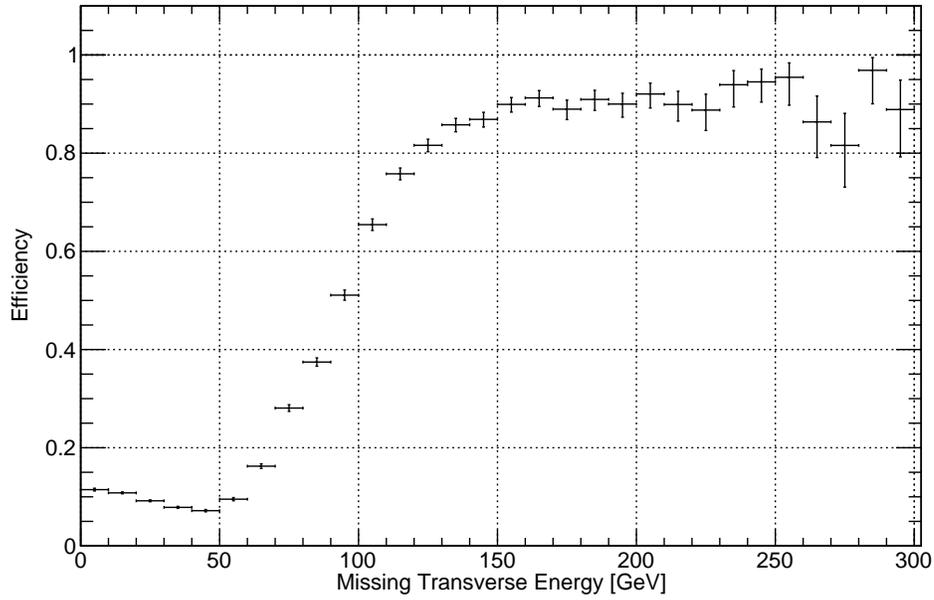
Figure 5.6: Efficiency plot for EF_xe60_noMu trigger using $Z + $ jets sample.

Chapter 6

Analysis Strategy

6.A CHARYBDIS: A black hole event generator

The black hole event generator CHARYBDIS2 [32] version 1.003 has been used to generate a Monte Carlo event sample. It is designed to simulate the production and decay of black holes in hadron collider experiments. The generator is interfaced, via the Les Houches accord [43], to PYTHIA version 6.421 which performs the parton shower evolution and hadronization, and decays.

The CHARYBDIS2 event generator models the production and decay of black holes. The decay particles are chosen according to the relative emission probabilities calculated for the evaporation phase. The decay of black hole is subject to the constraint that baryon number and charge must be conserved.

We have used the three parameters: $n = 4$, $M_D = 0.94$ TeV and $\sqrt{\theta} = 0.64$ TeV^{-1} as described in Chapter 2 of Section 2.D.1 to calculate the remnant mass of the black hole used for this work. $\sqrt{\theta}$ [14] is special for modifying CHARYBDIS2 to model noncommutative black holes. Table 6.1 shows the input parameters used

in generating the black hole signal sample for this work.

Name	Description	Value
MINMSS	Minimum mass of black hole	0.94 TeV
MAXMSS	Maximum mass of black hole	7 TeV
MPLNCK	Planck scale	0.94 TeV
TOTDIM	Total number of dimensions	8

Table 6.1: Some input parameter used with CHARYBDIS2 in creation of a black hole signal sample with 4 extra dimensions, $D-$dimensional Planck scale, $M_D = 0.94$ TeV and remnant mass of 3.6 TeV.

6.B   Black Hole and Background Samples

In this study, we have used a beam energy of 7 TeV. Our simulated signal is a non-commutative black hole in four extra spatial dimensions, and with a cross section of 4.67 pb (this value is as a result of computing, πr_g^2, where r_g is the noncommutative gravitational radius, which depends on the number of dimensions and M_D). The signal sample consists of 5000 events, and corresponds to a luminosity of 1.1 fb^{-1}. Our goal has been to separate a black hole signal from that of Standard Model background processes. Noncommutative black hole events will have high multiplicity with soft p_T jets.

The relevant background to a back hole signal, will be highly energetic events. Events with soft scalar sum of transverse momentum and high multiplicity of particles are of interest. The main backgrounds that we have studied is QCD dijet production, $t\bar{t}$ production, $W+$jets production and $Z+$jets production.

Since dijet events have a large production cross section, they provide a considerable source of background for many processes. In ATLAS, Monte Carlo (MC) simulated dijet samples are often called JN (where N is 0,1,..,8), and indicate the

momentum range in GeV for the most energetic (leading) jet before radiation as shown in Table 6.2.

6.B.1 Normalizing the signal and background samples

In order to obtain the right ratio between Monte Carlo simulated samples (signal and background) and data from the LHC, we have to normalize the Monte Carlo simulated samples and the data. In this study, we normalized both the Monte Carlo simulated number of events, background and signal, to the data by scaling the Monte Carlo samples to the same luminosity as the data. The scaling factor, or weight (w) is given by

$$w = \frac{\mathrm{Lumi_{data}}\sigma_{\mathrm{MC}}}{\text{Number of MC events}}, \tag{6.1}$$

where w is the weight listed in Table 6.2, $\mathrm{Lumi_{data}}$ is the luminosity of the data and σ_{MC} is the cross-section for the respective background and signal Monte Carlo simulated processes.

Process	Generator	Sample	$\hat{p}_T$ [GeV]	σ [pb]	# Events before weighting	weight (w)
QCD dijet	PYTHIA	J0	$8-17$	$1.2030.10^{10}$	999997	$6.8625.10^{6}$
		J1	$17-35$	$8.0726.10^{8}$	999993	$4.6051.10^{5}$
		J2	$35-70$	$4.8048.10^{7}$	999999	$2.7409.10^{4}$
		J3	$70-140$	$2.5369.10^{6}$	999992	$1.274.10^{3}$
		J4	$140-280$	$9.9608.10^{4}$	989992	57.3958
		J5	$280-560$	$2.5950.10^{3}$	999987	1.48034
		J6	$560-1120$	35.4890	999974	$2.0245.10^{-2}$
		J7	$1120-2240$	0.13391	998955	$7.6469.10^{-5}$
		J8	$2240-\infty$	$5.6799.10^{-6}$	998948	$3.2435.10^{-9}$
$t\bar{t}$	MC@NLO	$t\bar{t}$	$-$	$1.4552.10^{2}$	1179034	$6.8842.10^{-2}$
W+jets	ALPGEN	W+jets	$-$	31.1060	1989246	$8.1768.10^{-3}$
Z+jets	ALPGEN	Z+jets	$-$	4.5721	249999	$1.0201.10^{-3}$
Black Hole	CHARYBDIS	Black Hole	$-$	4.6700	5000	$4.8881.10^{-1}$

Table 6.2: Monte Carlo simulated samples showing various processes with their respective weighting factor, w. These values are are based on those obtained from the ATLAS Metadata Interface (AMI).

6.B.2 Signal Properties

Quantum black holes are assumed to decay dominantly to Standard Model particles with quarks and gluons having the highest degree of freedom. The decay products from the noncommutative black hole with $M_D = 0.94$ TeV, $n = 4$ and minimum mass of 3.6 TeV are as shown in Figure 6.1 while Table 6.3 shows the numbering scheme. A particle ID is a Monte Carlo numbering scheme developed by the Particle Data Group (PDG) for representing particles. This figure shows the quarks ($|\text{pdgID}| < 7$) and gluon ($\text{pdgID} = 21$) occurring frequently followed by the leptons and neutrinos with absolute particle ID between 10 and 17.

Quarks	Leptons	Gauge bosons
d 1	e^- 11	g 21
u 2	ν_e 12	γ 22
s 3	μ^- 13	Z^0 23
c 4	ν_μ 14	W^+ 24
b 5	τ^- 15	h^0/H_1^0 25
t 6	ν_τ 16	

Table 6.3: Particle Data Group Monte Carlo particle numbering scheme [2].

Figures 6.1 to 6.8 show the characteristics of a noncommutative black hole signal with $n = 4$, $M_D = 0.94$ TeV and $M_{\min} = 3.6$ TeV. The distribution of the transverse momentum of the primary particles, Figure 6.3 to Figure 6.5 show a low value with high number of particles, Figure 6.2. This high number of particles is due to low energy particles being emitted during the later stage of the black hole decay. On average, seven particles are produced from the decay of the black hole in question, with an average of 42 GeV transverse momentum, Figure 6.3. The sum of transverse momentum, missing transverse energy and black hole invariant mass distributions are shown in Figures 6.6, 6.7 and 6.8 respectively.

Primary particles are the immediate decay product from a black hole, and are referred to as truth particle at the simulation or generator level. These decay products contain jet of particles which are narrow cone of hadrons and other particles produced by the hadronization of a quark or gluon.
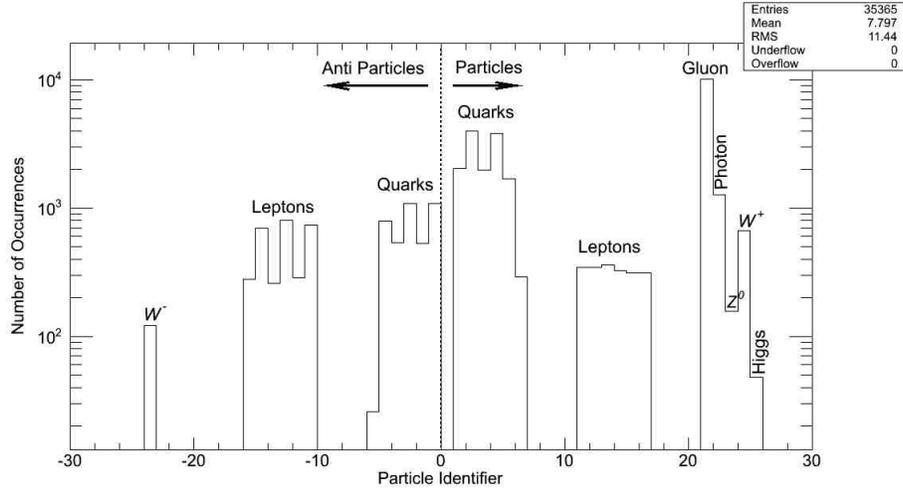
Figure 6.1: Primary particle ID of the decay products from a black hole with $n = 4$ extra dimensions, $M_D = 0.94$ TeV and $M_{\min} = 3.6$ TeV. To the left of the zero mark indicates anti-particles, while to the right of the zero mark indicates particles.
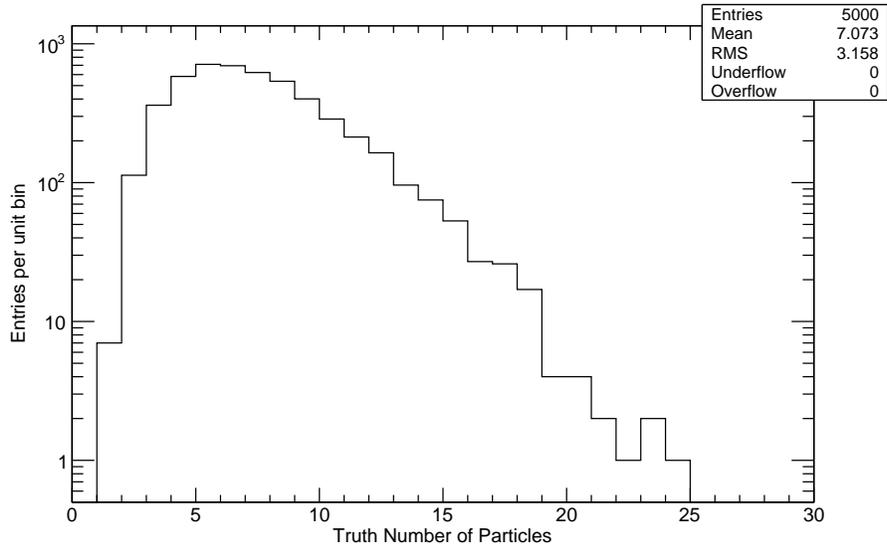
Figure 6.2: Primary particles from the decay of a black hole with $n = 4$ extra dimensions, $M_D = 0.94$ TeV and $M_{\min} = 3.6$ TeV.
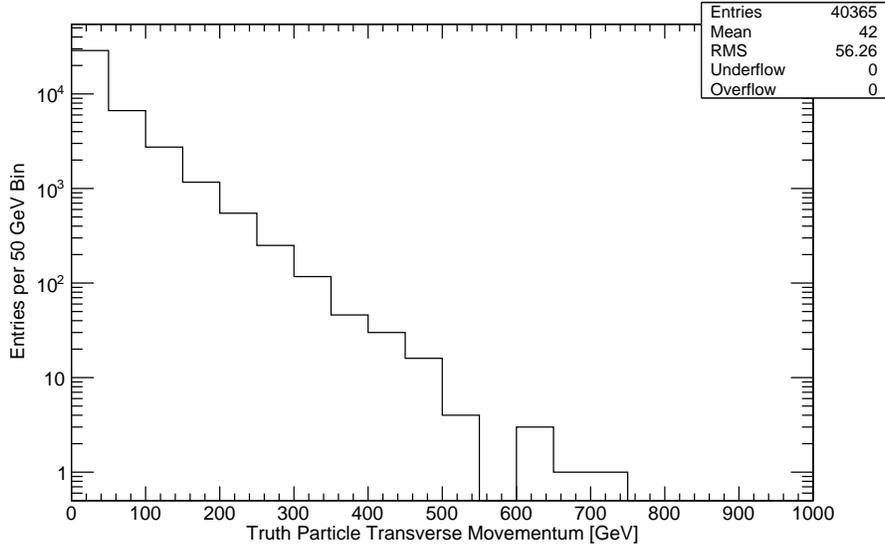
Figure 6.3: Primary particle transverse momentum from the decay of a black hole with $n = 4$ extra dimensions, $M_D = 0.94$ TeV and $M_{\min} = 3.6$ TeV.
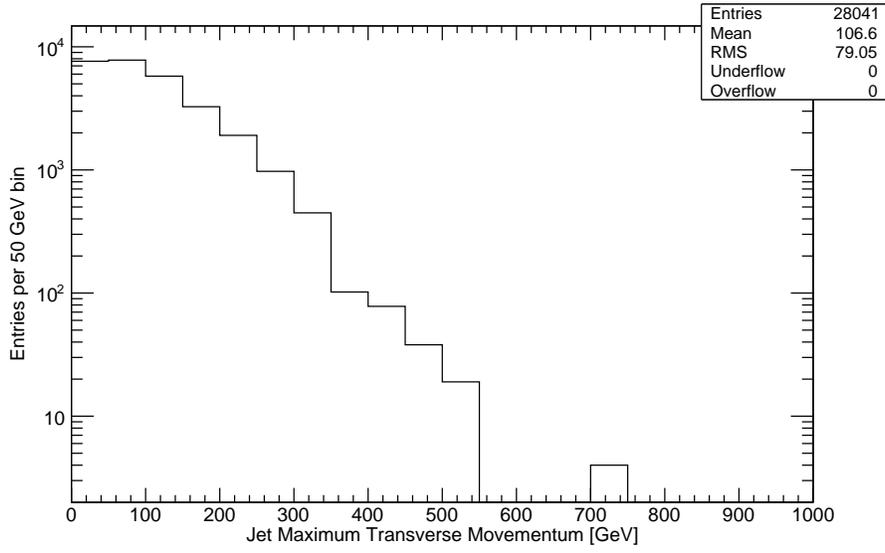
Figure 6.4: Jet maximum transverse momentum from the decay of a black hole with $n = 4$ extra dimensions, $M_D = 0.94$ TeV and $M_{\min} = 3.6$ TeV.
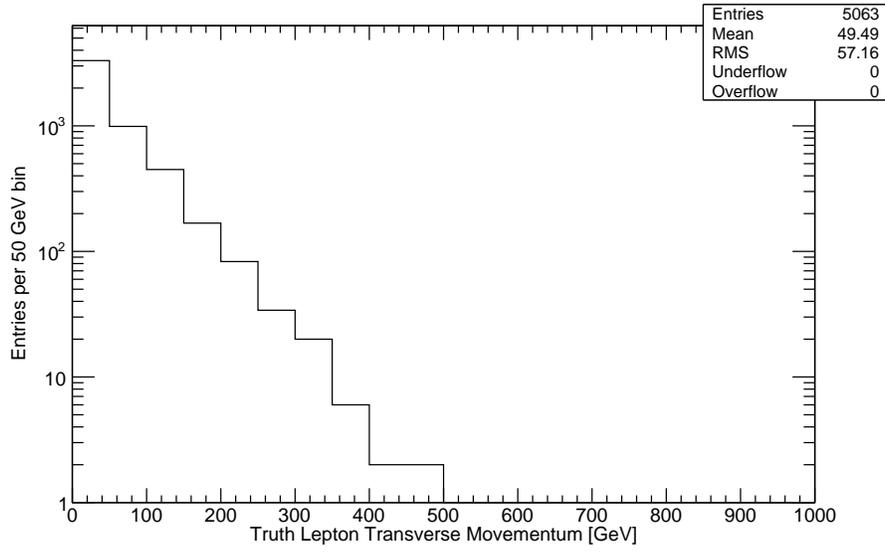
Figure 6.5: Lepton maximum transverse momentum from the decay of a black hole with $n = 4$ extra dimensions, $M_D = 0.94$ TeV and $M_{\min} = 3.6$ TeV.
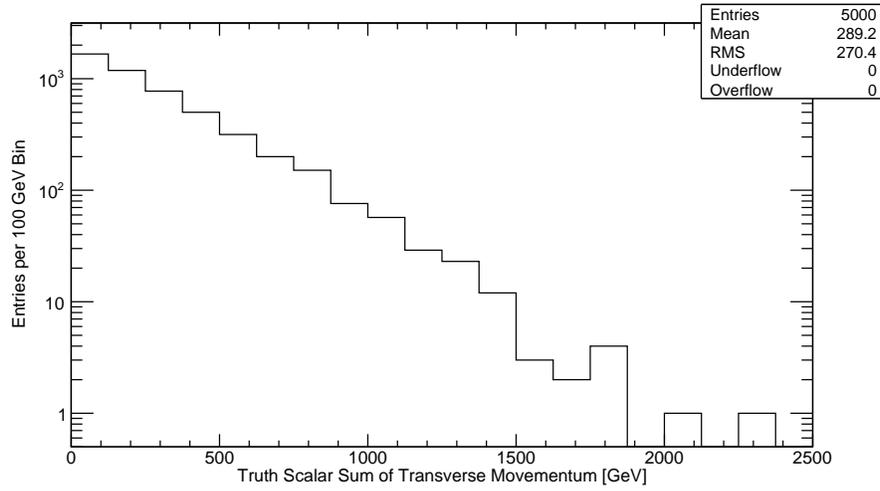
Figure 6.6: Scalar sum of transverse momentum from the decay of a black hole with $n = 4$ extra dimensions, $M_D = 0.94$ TeV and $M_{\min} = 3.6$ TeV.
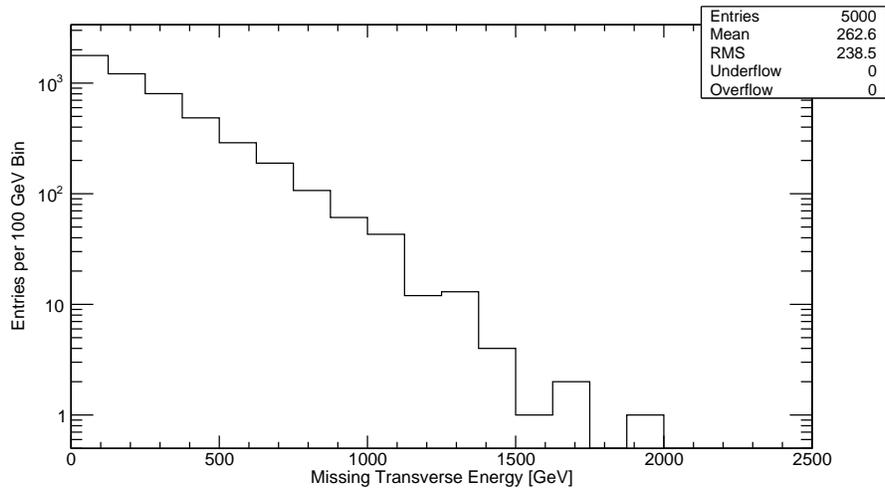
Figure 6.7: Missing transverse energy from the decay of a black hole with $n = 4$ extra dimensions, $M_D = 0.94$ TeV and $M_{\min} = 3.6$ TeV.
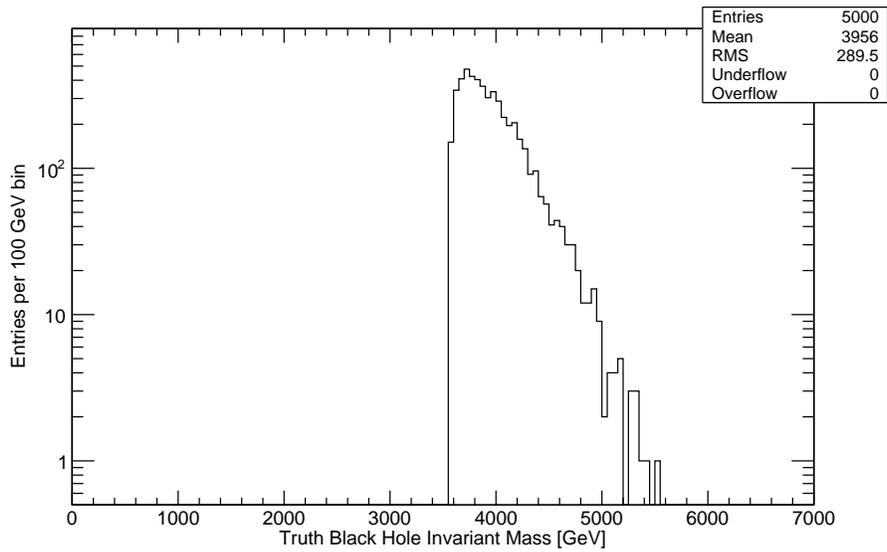
Figure 6.8: Invariant mass distribution of a black hole with $n = 4$ extra dimensions, $M_D = 0.94$ TeV and $M_{\min} = 3.6$ TeV.

6.C   Reconstruction and object selection

6.C.1   Jets

Anti-$k_\perp$

In order to form jets as physics objects from calorimeter clusters [44] an algorithm is needed. A relatively new approach is the anti-$k_\perp$ jet clustering algorithm [45].

This algorithm calculates, for all input objects i, the quantities d_{ij} and d_{iB} as follows:

$$d_{ij} = \min\left(k_{\perp i}^{-2}, k_{\perp j}^{-2}\right) \frac{(\Delta R)_{ij}^2}{R^2}, \tag{6.2}$$

$$d_{iB} = k_{\perp i}^{-2}, \tag{6.3}$$

where

$$(\Delta R)_{ij}^2 = \sqrt{(y_i - y_j)^2 + (\phi_i - \phi_j)^2}, \tag{6.4}$$

with $k_{\perp i}$ being the transverse momentum of object i and y_i its pseudorapidity (which will be represented by η later). The quantities d_{ij} and d_{iB} can be seen as distance parameters between objects, and an object to the beam, respectively. Having calculated all d_{ij} and d_{iB}, a sorted list is compiled. If the smallest entry is d_{ij} then the corresponding objects are merged. If the smallest entry is d_{iB}, object i is considered a jet. As a finalized object it is removed from the list. Thus this algorithm merges or finalizes objects with large transverse momentum first. The quantity R is a resolution parameter which determines the distance at which two neighbouring jets are resolved. After each step the list is recalculated until all objects are finalized. ΔR is the distance between particles in the $\eta - \phi$ plane.

In ATLAS, two versions of this algorithm are commonly used, only differing in the parameter R. These are named AntiKt4 and AntiKt6 with $R = 0.4$ and $R = 0.6$, respectively.

Jet Energy Scale and Resolution

The algorithm for reconstructing and measuring jet kinematics in data and detector-level simulated events uses topological clusters (topoclusters) [44] in the calorimeters. Topoclusters are groupings of neighbouring calorimeter cells that have significant energy above the expected noise level. This results in clusters that have a variable number of cells. They are three dimensional objects designed to follow the shower development, taking advantage of the calorimeter segmentation of the ATLAS detector. They are built around seeds, which are calorimeter cells with a signal-to-noise ratio above a certain threshold value. The baseline calibration of these clusters is based on test-beam measurements. This corrects the cluster energy to the electromagnetic scale. Since the ATLAS calorimeters have a lower response to hadronic than to electromagnetic energy deposition, a further correction is needed once a jet is identified. This correction factor is determined with global cell weighting using simulated data and is mainly η and p_T dependent. Energy losses due to material in front of the calorimeters are compensated by this calibration method. Dead material and fluctuations in the hadronic shower, in particular in its electromagnetic content, worsen the resolution beyond the intrinsic energy resolution of the calorimeters. Test-beam data [46, 47] and in-situ measurements [48, 49] show, that the detector simulation describes the calorimeter response to single hadrons to within 5%.

The final energy scale calibration and its uncertainty account by design for uncertainties in the hadronic shower modeling, description of calorimeter noise, material in front of the calorimeters and uncertainties due to differences between test-beam measurements and the in-situ detector. In a study done with the first 7 nb^{-1} of data [50], the jet energy scale calibration is determined using numerical inversion of the response calculated from MC. The overall p_T correction for jets is below 50%, for central jets (i.e. the barrel region) with $p_T > 60$ GeV below 35%. The overall

uncertainty is below 9% for the entire η and p_T range and below 7% for central jets with $p_T > 60$ GeV.

With the first 6 nb^{-1} of data, the jet energy resolution was determined [51]. Two different techniques are used. The first method uses dijet balance. A Gaussian is fitted to the distribution of the asymmetry of the two jet transverse momenta and its width is used to determine the resolution. The other method is called bi-sector method and uses an imbalance vector, defined as vector sum of the two leading (most energetic) jets in the event. Deviations from zero are used to determine the resolution. The results from both methods are compared to the MC prediction from Pythia. Both methods give consistent results, and the resolution on Monte Carlo is found to agree with the resolution on data within 14% for jets with 20 GeV $< p_T < 80$ GeV and $|\eta| < 2.8$.

Event Cleaning

Especially in the early data taking periods of an experiment it is probable to find a behaviour of the detector which is unexpected. These detector effects can lead to fake jets (called *bad jets*) or to problems in the jet energy scale (called *ugly jets*). Typical causes are sporadic noise cells in the LAr and Tile calorimeter, noise bursts in the HEC and coherent noise in the electromagnetic calorimeter. Additionally, cosmics and beam background can distort the measurement. To ensure a clean data sample, selection criteria have to be defined to find jet candidates which are with a high probability good jets, i.e. not bad or ugly jets. An extensive study of these effects has been done by the ATLAS collaboration [52]. These are the recommended selection criteria:

Reject jets created by detector effects (bad jets)

1. The five cells with the highest energy deposition must contain less than 90% of the energy of the jet.

2. The fraction of the jet energy deposited in the hadronic end-cap (fHEC) is less than or equal to 0.8.

3. The absolute value of the jet quality variable, which quantifies how closely the measured calorimeter pulses match a reference pulse is less than 1-fHEC.

4. The fraction of energy of the jet deposited in the electromagnetic calorimeter is less than or equal to 0.95.

5. The cell-weighted time of the jet is less than 50 ns different from the average event time.

Reject jets with problematic Jet Energy Scale (ugly jets)

1. The fraction of the jet energy deposited in the TileGap3 scintillators must be less than or equal to 0.5.

2. The fraction of the jet energy coming from masked cells, whose energy is extrapolated using the energy density of neighbouring cells, must be less than or equal to 0.5.

A fake or wrongly measured jet has two effects on the analysis. Besides the energy from the bad or ugly jet itself, it leads to a mis-measurement of E_T^{miss} in the event. Since, in this work, both the energy and E_T^{miss} are used, this leads to poorly measured event properties. Thus if a bad or ugly jet is found with $p_T > 70$ GeV, the whole event is rejected. This avoids faked signal candidates and ensures a clean data sample at a fraction of 0.78.

Jet Selection

In this thesis jets reconstructed with the anti-$k_\perp$ algorithm and a resolution parameter of $R = 0.4$ (AntiKt4) are used. The transverse momentum is taken at the calibrated jet energy scale determined with global cell weighting. The momentum

69

requirement for a jet is $p_T > 70$ GeV. The fiducial selection is the restriction to central jets with $|\eta| < 2.8$. This is the range, for which the energy calibration is valid.

6.C.2   Missing Transverse Energy

The reconstruction of the missing transverse energy E_T^{miss} is based on calorimeter energy deposits as well as on muon information. The algorithm and performance is described in Ref. [53]. The calorimeter contribution is calculated using cells from topological clusters. This helps to limit the number of contributing cells, N_{cell} and thus the influence of noise on E_T^{miss}. For calibration purposes the so called local cluster weighting scheme is used. It first classifies a hadronic topocluster as electromagnetic or hadronic, depending on its topology. Additional corrections are applied for energy loss due to deposits outside the topocluster or in dead material in front or close to the topocluster. Weights determined from Monte Carlo simulations are then used to calibrate the topocluster cells. The muon contribution is calculated from both isolated and non-isolated (within $\Delta R < 0.3$ to the closest jet) muon candidates. Isolated muons are using the combined information from both the muon system and the inner detector. For non-isolated muons it is impossible to distinguish between muon and jet tracks in the inner detector. Therefore, only the information from the muon system is used.

The missing transverse energy is then calculated as:

$$E_T^{\mathrm{miss}} = \sqrt{(E_{\mathrm{x}}^{\mathrm{miss}})^2 + (E_{\mathrm{y}}^{\mathrm{miss}})^2}, \tag{6.5}$$

where

$$E_{\mathrm{x(y)}}^{\mathrm{miss}} = -\left(E_{\mathrm{x(y)}}^{\mathrm{calo}} + E_{\mathrm{x(y)}}^{\mu(\mathrm{iso})} + E_{\mathrm{x(y)}}^{\mu(\mathrm{non-iso})}\right), \tag{6.6}$$

where $E_{\mathrm{x(y)}}^{\mathrm{calo}}$ is the contribution from energy lost by muons in the calorimeter, the

$E_{x(y)}^{\mu(\text{iso})}$ is the contribution from isolated muons, and $E_{x(y)}^{\mu(\text{non}-\text{iso})}$ from non-isolated muons.

6.C.3   Definitions

In this work, the following definitions are chosen for the transverse momentum sum and invariant mass: $\sum p_T$ is defined as the scalar sum of the transverse momentum p_T for all selected reconstructed final jets. E_T^{miss} is not included in this sum.

6.C.4   Primary Vertices

The reconstruction of the primary vertex and secondary vertices is part of the track reconstruction [54]. It is divided into two steps. In the first step, the primary vertex finding, reconstructed tracks are associated to a particular vertex candidate. In the second step, the vertex fitting, the actual vertex position is reconstructed and its quality estimated. Candidates for primary vertices can for example be created from a pre-selection of tracks with a given minimum p_T. These tracks are compatible with the expected bunch-crossing region which are grouped into clusters. These clusters are then cleaned iteratively for outlying tracks based, for example, on the χ^2 of the fit of the track and the vertex. For our analysis, we require a primary vertex having at least five tracks.

6.C.5   Good Run Lists

Data collected in ATLAS are taken in periods which spans a certain interval of time, or a certain range of run numbers. Each run at the start of the year is given a letter starting with A. Runs may have sub-periods, i.e. period 2011A comprise A1 and A2.

Each period may consist of one or more physics runs. A physics run usually

starts after the beams in the LHC have been accelerated to the nominal centre-of-mass energy and declared stable. Each run comprises luminosity blocks (LBs), which in turn consist of several thousand events each. A luminosity block is the smallest entity over which the detector and beam conditions are assumed to be stable.

Not all of the data which has been recorded with the ATLAS detector is suitable for physics analyses. Problems with the detector may compromise the data and render part of the data unusable. The requirements of individual physics analyses with respect to the quality of the data differs depending on the type of analysis. To accommodate for the needs of different analyses, while providing a unified approach to assess the data quality, the status of the detector is monitored throughout data taking and observed problems with the data are stored in a database. From this database, a Good Run Lists (GRLs) can be created [55]. They are part of the input to every analysis and define which subset of the data taken with the ATLAS detector is suitable to be considered for physics or performance analyses.

GRLs are stored as text files in the extensible markup language (xml) file format and contain lists of runs. Each run contains a list of the luminosity blocks for which all quality requirements (non problematic detectors) have been met.

6.C.6 LAr hole and LArError

The LAr hole is a term used for a detector problem, which affects part of the electromagnetic liquid-argon calorimeter in the barrel. The region affected by the LAr hole is $[-0.1, 1.5] \times [-0.9, -0.5]$ in $\eta \times \phi$ space. For physics analyses, a way to deal with this problem is to reject events which include jets that fall into the LAr hole region.

The LArError are errors due to bad or corrupted events. They are as a result of LAr noise burst and data corruption at the detector level. These faults are corrected

by rejecting events having this problem.

6.D   Event Selection

Black holes are searched for in the 2011 ATLAS data and the official selection developed within the ATLAS JetEtMiss group have been implemented on this data.

To give a first idea of how the analysis proceeds, the cuts can be grouped into non physics (standard ATLAS JetEtMiss group cuts) and physics cuts (derived cuts).

The non physics cuts are selection of collision candidates and event clean-up (cf. Section 6.C.1). This step filters out bad data from runs with known detector problems, and also implements the trigger selection. Physics cuts on the other hand help optimize our signal event sample, while reducing the MC simulated background events.

Selection cut	Cut	Cut description	Event count	$\epsilon_{\mathrm{cut}}[\%]$	$\epsilon_{\mathrm{cd}}[\%]$
–		Raw events	59001494	–	–
1		Good Runs List (GRL)	54207738	91.9	–
2		Trigger	2263965	4.2	100
3	Non physics	Primary vertex	2222849	98.2	98.2
4		LArError	2208330	99.3	97.5
5		Bad jets	1770833	80.2	78.2
6		LArHole	1426730	80.6	63.0
7		$E_T^{\mathrm{miss}} > 140$ GeV	34418	2.4	1.5
8		$N_{jet} \geq 2$	13053	37.9	0.6
9	Physics	$\sum p_T / E_T^{\mathrm{miss}} < 7$	12566	96.3	0.6
10		$p_T^{1st} / E_T^{\mathrm{miss}} < 3$	11911	94.8	0.5

Table 6.4: Overview of the complete selection of the analysis with short description of the cuts given together with the number of events in data left after each cut. ϵ_{cut} is the efficiency of the cut on this sample with respect to the preceding cut, while ϵ_{cd} is the cumulative decrease of efficiency of the cut with respect to the trigger cut.

Tables 6.4 and 6.5 summarizes the event counts in data and in Monte Carlo,

following from the selection criteria according to the cut presented in the Table 6.4, as well as the statistical uncertainties on these numbers.

Table 6.5 lists the event counts from the cut on Monte Carlo for the different QCD background samples, while Table 6.6 shows the number of expected events in the QCD background samples. The expected events are events that have been weighted with the luminosity of the data, and the process's respective cross-section.

In Table 6.6, all Monte Carlo simulated samples used for this analysis are shown as well as event counts which follows from the selection criteria used. Tables 6.7 and 6.8 shows the event counts in all Monte Carlo samples and the expected numbers respectively.

The cut efficiency, ϵ_{cut}, on the respective samples with respect to the preceding cut is shown in Table 6.10. The table shows which of the backgrounds gives the largest contribution and allows to compare the efficiency of the cuts with respect to the suppression of the backgrounds. It demonstrates that a strong suppression of the dominating QCD background is achieved by cutting on the E_T^{miss}. The table allows to compare the expected event counts in the signal regions from Standard Model backgrounds modeled in the Monte Carlo simulated samples to the event counts that were actually measured in data.

Selection cut	J0	J1	J2	J3	J4	J5	J6	J7	J8
Raw Events	999997	999993	999999	999992	989992	999987	999974	998955	998948
GRL	999997	999993	999999	999992	989992	999987	999974	998955	998948
Trigger	1	1	4	366	16542	129812	354699	605452	762945
Primary Vertex	1	1	4	366	16528	129714	354292	604082	760034
LArError	1	1	4	366	16528	129714	354292	604082	760034
Bad jets	0	0	1	300	14809	117247	321492	551858	699864
LArHole	0	0	1	290	14275	113274	311219	535589	682237
$E_T^{\mathrm{miss}} > 140$ GeV	0	0	0	0	73	4203	47477	207680	435428
$N_{jet} \geq 2$	0	0	0	0	59	4188	47476	207680	435428
$\sum p_T/E_T^{\mathrm{miss}} <7$	0	0	0	0	59	4038	25434	41521	61557
$p_T^{1st}/E_T^{\mathrm{miss}} < 3$	0	0	0	0	59	3547	13687	23059	35722

Table 6.5: Number of QCD Monte Carlo simulated events left after selection criteria.

Selection cut	J0	J1	J2	J3	J4	J5	J6	J7	J8
Raw Events	$6.9.10^{12}$	$4.6.10^{11}$	$2.7.10^{10}$	$1.4.10^9$	$5.7.10^7$	$1.5.10^6$	$2.0.10^4$	76.4	0.0
GRL	$6.9.10^{12}$	$4.6.10^{11}$	$2.7.10^{10}$	$1.4.10^9$	$5.7.10^7$	$1.5.10^6$	$2.0.10^4$	76.4	0.0
Trigger	$6.9.10^6$	$4.6.10^5$	$1.1.10^4$	$5.3.10^5$	$9.5.10^5$	$1.9.10^5$	7181.0	46.3	0.0
Primary Vertex	$6.9.10^6$	$4.6.10^5$	$1.1.10^4$	$5.3.10^5$	$9.5.10^5$	$1.9.10^5$	7172.7	46.2	0.0
LArError	$6.9.10^6$	$4.6.10^5$	$1.1.10^4$	$5.3.10^5$	$9.5.10^5$	$1.9.10^5$	7172.7	46.2	0.0
Bad jets	0.0	0.0	$2.7.10^4$	$4.3.10^5$	$8.5.10^5$	$1.7.10^5$	6508.7	42.2	0.0
LArHole	0.0	0.0	$2.7.10^4$	$4.2.10^5$	$8.2.10^5$	$1.7.10^5$	6300.7	41.0	0.0
$E_T^{\mathrm{miss}} > 140$ GeV	0.0	0.0	0.0	0.0	4189.9	6221.9	961.2	15.9	0.0
$N_{jet} \geq 2$	0.0	0.0	0.0	0.0	3386.4	6199.7	961.2	15.9	0.0
$\sum p_T/E_T^{\mathrm{miss}} <7$	0.0	0.0	0.0	0.0	0.0	5977.6	514.9	3.2	0.0
$p_T^{1st}/E_T^{\mathrm{miss}} < 3$	0.0	0.0	0.0	0.0	0.0	5250.8	277.1	1.8	0.0

Table 6.6: Number of QCD Monte Carlo simulated events left after the selection criteria normalized to an integrated luminosity of 502 pb^{-1}.

The background sample is the total sum of all Monte Carlo simulated events: QCD + (Z+jets)+(W+jets)+$t\bar{t}$.

Selection cut	QCD	Z+jets	W+jets	$t\bar{t}$	Background	Black Hole
Raw Events	8987837	249999	1989246	1179034	12406116	5000
GRL	8987837	249999	1989246	1179034	12406116	5000
Trigger	1865022	21168	183182	19708	2093880	2748
Primary Vertex	1865022	20990	181936	19667	2087605	2608
LArError	1865022	20990	181936	19657	2087605	2608
Bad jets	1705571	16176	149500	17229	1888476	2585
LArHole	1656885	15941	147631	16549	1837006	2585
$E_T^{\mathrm{miss}} > 140$ GeV	694861	2019	21055	322	718257	1742
$N_{jet} \geq 2$	694831	670	7473	319	703293	1077
$\sum p_T/E_T^{\mathrm{miss}} < 7$	132609	668	7466	290	141033	1077
$p_T^{1st}/E_T^{\mathrm{miss}} < 3$	76074	666	7452	271	84463	1077

Table 6.7: Expected number of background, signal and total background Monte Carlo simulated events for the selection criteria.

Selection cut	QCD	Z+jets	W+jets	$t\bar{t}$	Background	Black Hole
Raw Events	7.3×10^{12}	2550.2	1.6×10^4	8.0×10^4	7.3×10^{12}	2444.1
GRL	7.3×10^{12}	2550.2	1.6×10^4	8.0×10^4	7.3×10^{12}	2444.1
Trigger	9.1×10^6	215.9	1497.9	1356.7	9.1×10^6	1343.3
Primary Vertex	9.1×10^6	214.1	1487.7	1353.2	9.1×10^6	1274.8
LArError	9.1×10^6	214.1	1487.7	1353.2	9.1×10^6	1274.8
Bad jets	1.5×10^6	165.0	1222.4	1186.1	1.5×10^6	1263.6
LArHole	1.4×10^6	162.6	1207.1	1139.3	1.4×10^6	1263.6
$E_T^{\mathrm{miss}} > 140$ GeV	1.1×10^4	20.6	172.2	22.2	1.2×10^4	851.5
$N_{jet} \geq 2$	1.1×10^4	6.8	61.1	22.0	1.1×10^4	526.5
$\sum p_T/E_T^{\mathrm{miss}} < 7$	6495.7	6.8	61.0	20.0	6583.5	526.5
$p_T^{1st}/E_T^{\mathrm{miss}} < 3$	5529.6	6.8	60.9	18.7	5616.0	526.5

Table 6.8: Expected number of background, signal and total background Monte Carlo simulated events for the selection criteria normalized to an integrated luminosity of 502 pb^{-1}.

Selection cut	QCD[%]	Z+jets[%]	W+jets[%]	$t\bar{t}$[%]	Background[%]	Black Hole[%]
Raw Events	–	–	–	–	–	–
GRL	–	–	–	–	–	–
Trigger	100.0	100.0	100.0	100.0	100.0	100.0
Primary Vertex	100.0	99.2	99.3	99.7	100.0	94.9
LArError	100.0	99.2	99.3	99.7	100.0	94.9
Bad jets	16.4	76.4	81.6	87.4	16.4	94.1
LArHole	15.8	75.3	80.6	84.0	15.8	94.1
$E_T^{\mathrm{miss}} > 140$ GeV	0.1	9.5	11.5	1.6	0.1	63.4
$N_{jet} \geq 2$	0.1	3.2	4.1	1.6	0.1	39.2
$\sum p_T/E_T^{\mathrm{miss}} < 7$	0.1	3.2	4.1	1.5	0.1	39.2
$p_T^{1st}/E_T^{\mathrm{miss}} < 3$	0.1	3.1	4.1	1.4	0.1	39.2

Table 6.9: Percentage cumulative decrease (ϵ_{cd}) of expected number of black hole and background Monte Carlo simulated events for the selection criteria with respect to the trigger cut.

Selection cut	QCD[%]	Z+jets[%]	W+jets[%]	$t\bar{t}$[%]	Background[%]	Black Hole[%]
Raw Events	–	–	–	–	–	–
GRL	100.0	100.0	100.0	100.0	100.0	100.0
Trigger	0.0	8.5	9.2	1.7	0.0	55.0
Primary Vertex	100.0	99.2	99.3	99.7	100.0	94.9
LArError	100.0	100.0	100.0	100.0	100.0	100.0
Bad jets	16.4	77.1	82.2	87.6	16.4	99.1
LArHole	96.6	98.5	98.7	96.1	96.6	100
$E_T^{\mathrm{miss}} > 140$ GeV	0.8	12.7	14.3	1.9	0.8	67.4
$N_{jet} \geq 2$	92.7	33.2	35.5	99.1	91.8	61.6
$\sum p_T/E_T^{\mathrm{miss}} < 7$	61.5	99.7	99.9	90.9	61.8	100.0
$p_T^{1st}/E_T^{\mathrm{miss}} < 3$	85.1	99.7	99.8	93.4	85.3	100.0

Table 6.10: Percentage of expected number of black hole and background Monte Carlo simulated events for the selection criteria with respect to the proceeding cut.

6.D.1 Statistical Uncertainty

The statistical uncertainty is determined by the number of events available within the Monte Carlo simulated samples. It can be directly evaluated from Monte Carlo, assuming no error on w_i for the bin contents or the number of events at a certain step of the selection criteria. If N_i is the number of events from Monte Carlo simulated sample i remaining after each selection cut, the uncertainty σ_i on the contribution from this sample is taken to be the square root of the number of events $\sqrt{N_i}$, which is just the standard deviation of a distribution with expectation value N_i. The total uncertainty is the weighted sum over all Monte Carlo simulated samples. Denoting the weight of sample i with w_i, the total uncertainty σ_N is therefore given by

$$\sigma_N = \sqrt{\sum_i w_i^2 \sigma_i^2} = \sqrt{\sum_i w_i^2 N_i}. \tag{6.7}$$

Selection cut	QCD	Z+jets	W+jets	$t\bar{t}$	Background	Black Hole
Raw Events	7.3×10^{12} $\pm 6.9 \times 10^9$	2550.2 ± 35.0	1.6×10^4 ± 14.1	8.0×10^4 ± 76.0	7.3×10^{12} $\pm 6.9 \times 10^9$	2444.1 ± 34.6
GRL	7.3×10^{12} $\pm 6.9 \times 10^9$	2550.2 ± 35.0	1.6×10^4 ± 14.1	8.0×10^4 ± 76.0	7.3×10^{12} $\pm 6.9 \times 10^9$	2444.1 ± 34.6
Trigger	9.1×10^6 $\pm 6.9 \times 10^6$	215.9 ± 10.2	1497.9 ± 4.3	1356.7 ± 9.8	9.1×10^6 $\pm 6.9 \times 10^6$	1343.3 ± 25.7
Primary Vertex	9.1×10^6 $\pm 6.9 \times 10^6$	214.1 ± 10.1	1487.7 ± 4.3	1353.2 ± 9.8	9.1×10^6 $\pm 6.9 \times 10^6$	1274.8 ± 25.0
LArError	9.1×10^6 $\pm 6.9 \times 10^6$	214.1 ± 10.1	1487.7 ± 4.3	1353.2 ± 9.8	9.1×10^6 $\pm 6.9 \times 10^6$	1274.8 ± 25.0
Bad jets	1.5×10^6 $\pm 3.8 \times 10^4$	165.0 ± 8.9	1222.4 ± 3.9	1186.1 ± 9.8	1.5×10^6 $\pm 3.8 \times 10^4$	1263.6 ± 24.9
LArHole	1.4×10^6 $\pm 3.7 \times 10^4$	162.6 ± 8.8	1207.1 ± 3.8	1139.3 ± 9.0	1.4×10^6 $\pm 3.8 \times 10^4$	1263.6 ± 24.9
$E_T^{\mathrm{miss}} > 140$ GeV	1.1×10^4 ± 490.4	20.6 ± 3.1	172.2 ± 1.5	22.2 ± 1.3	1.2×10^4 ± 496.3	851.5 ± 20.5
$N_{jet} \geq 2$	1.1×10^4 ± 440.9	6.8 ± 1.8	61.1 ± 0.9	22.0 ± 1.3	1.1×10^4 ± 444.8	526.5 ± 16.1
$\sum p_T / E_T^{\mathrm{miss}} < 7$	6495.7 ± 440.9	6.8 ± 1.8	61.0 ± 0.9	20.0 ± 1.2	6583.5 ± 444.8	526.5 ± 16.1
$p_T^{1st} / E_T^{\mathrm{miss}} < 3$	5529.6 ± 440.9	6.8 ± 1.8	60.9 ± 0.9	18.7 ± 1.2	5616.0 ± 444.7	526.5 ± 16.1

Table 6.11: Expected number with statistical uncertainty from the Monte Carlo simulated events normalized to an integrated luminosity of 502 pb^{-1}.

6.D.2 $E_T^{\mathrm{miss}} > 140$ GeV selection cut

The E_T^{miss} cut is made in order to achieve a trigger efficiency of 100%. In Table 6.10, we observe a significant suppression of QCD events as a result of applying this cut.

6.D.3 $N_{jet} \geq 2$ selection cut

Since noncommutative black hole events are characterized by high multiplicity with soft-p_T jets, care is taken not to impose a high cutoff value on the p_T of the jet with

the purpose of reducing the Monte Carlo background samples drastically. The N_{jet} cut is based on a jet having a p_T greater than 70 GeV and an absolute η of less than 2.8.

A number of important distributions on which the $N_{jet} \geq 2$ selection cut in the analysis are based, are shown in Figures 6.9 through 6.30. All of them show the distribution of the respective variable in data and in Monte Carlo simulated events. The upper part of each plot shows several distributions in terms of event counts, the data being represented by the black dots, for which the error bars give statistical uncertainties. The background expectations from Monte Carlo are represented by the histograms, superimposing the QCD, $W+$ jets, $Z+$ jets and $t\bar{t}$ background expectations on top of each other in different colours. They are normalized to the integrated luminosity of $502\,\mathrm{pb}^{-1}$ (cf. Equation (6.1)). Not shown on the histograms are the total background contributions from all Monte Carlo simulated background events which are often stacked histograms.

In the lower part of each plot, the ratio of the observed data and Monte Carlo expectation are compared bin-by-bin to provide an overview of where the Monte Carlo underestimates or overestimates the number of events observed in data at one glance. The error bars show the uncertainties on the ratio, which comes from the statistical uncertainty on the number of data events (cf. Equation 6.9 and Table 6.4).

The distributions shown in the plots are the distributions after the $N_{jet} \geq 2$ selection cut. Specifically, the plots show the following distributions: Figure 6.9 shows the distribution of the jet multiplicity. In the first bin, the Monte Carlo simulated background underestimates the data, while in the last two bins, the Monte Carlo simulated overestimates it. Figure 6.10 shows the distribution of the E_T^{miss} at 140 GeV in the dijet channel. Figure 6.11 shows the distribution of the leading jet transverse momentum, p_T^{1st}. The Monte Carlo QCD background in the lower p_T

regime significantly misrepresents the data, hence we apply a p_T cut of 150 GeV to achieve a close agreement between simulated QCD and data. This procedure is a trade-off between achieving a good agreement of data and Monte Carlo background with decreasing the Monte Carlo signal yield since noncommutative black holes posses soft-p_T jets. The scalar sum of jet transverse momentum, $\sum p_T$ is shown in Figure 6.12. Cutting on the $\sum p_T$ of jets with a value greater than 300 GeV helps achieve a good modeling (or agreement) of the Monte Carlo simulated QCD background with the data, with the QCD process underestimating the data by a factor of 0.4 in the first bin.

In all plots, the MC simulated events are normalized to the data.
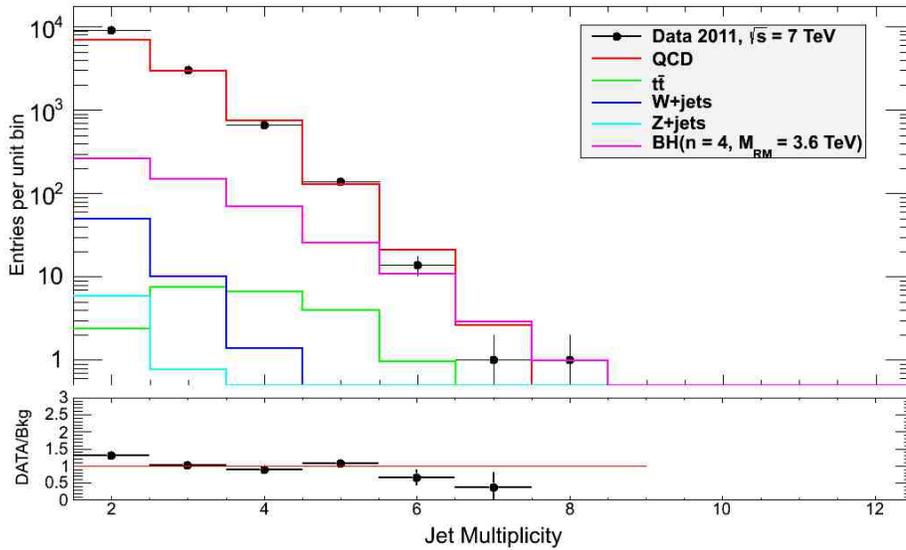
Figure 6.9: Comparison of the distribution of jet multiplicity.

81
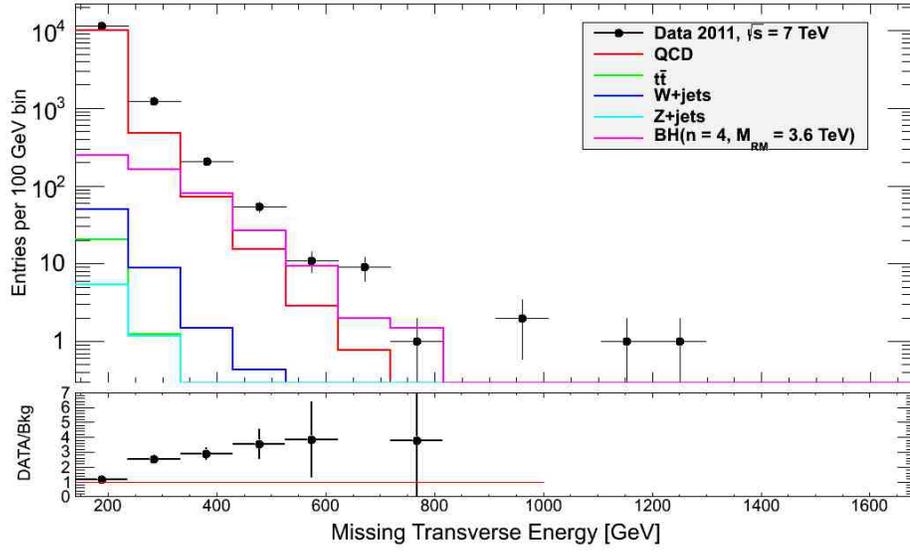
Figure 6.10: Comparison of the distribution of missing transverse energy after $N_{jet} \geq 2$ selection cut.
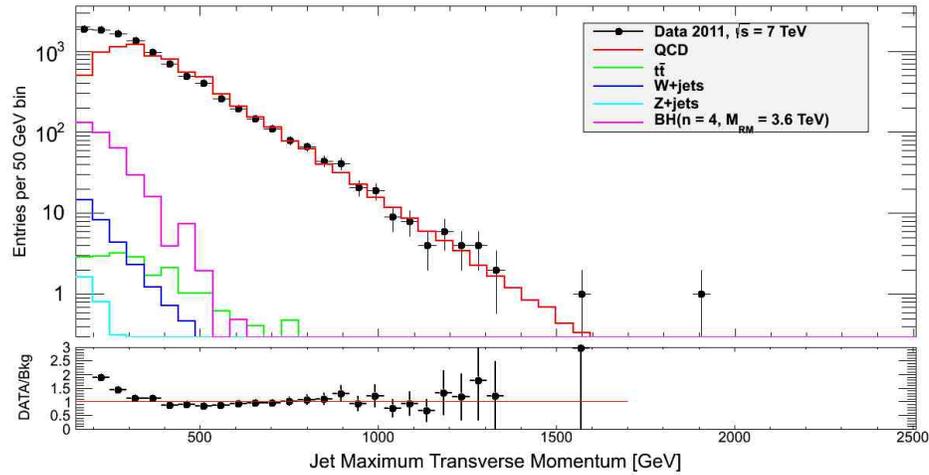
Figure 6.11: Comparison of distribution of leading jet p_T of all data samples after the $N_{jet} \geq 2$ selection cut.

82
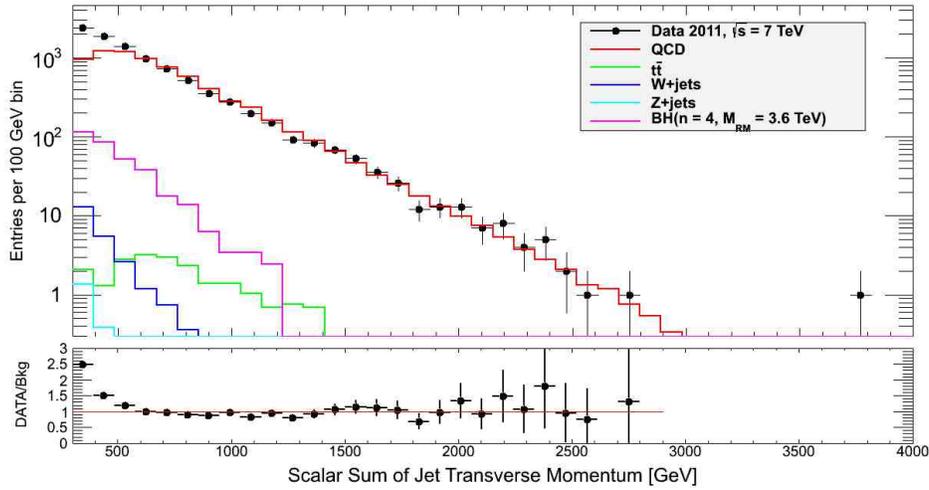
Figure 6.12: Comparison of distribution of jet $\sum p_T$ of all data samples after the $N_{jet} \geq 2$ selection cut.

After the $N_{jet} \geq 2$ we observe more background to signal events in the distribution of the most energetic jet and sum p_T, Figures 6.11 and 6.12. Therefore, to reduce the background, we check the correlation of our kinematic variables: leading jet transverse momentum, p_T^{1st}, scalar sum of jet transverse momentum, $\sum p_T$, and missing transverse energy, E_T^{miss}. Figures 6.13 through 6.30 show correlation plots of scalar sum of jet transverse momentum and leading jet transverse momentum, leading jet transverse momentum and missing transverse energy, and scalar sum of jet transverse momentum and missing transverse energy of the data, QCD, $t\bar{t}$, $W+$ jets, $Z+$ jets and black hole, respectively.

The distribution of $\sum p_T$ versus p_T^{1st}, Figures 6.13 through 6.18, show a linear correlation. Hence, those combinations or candidates can not be a suitable parameter for reducing our background sample.
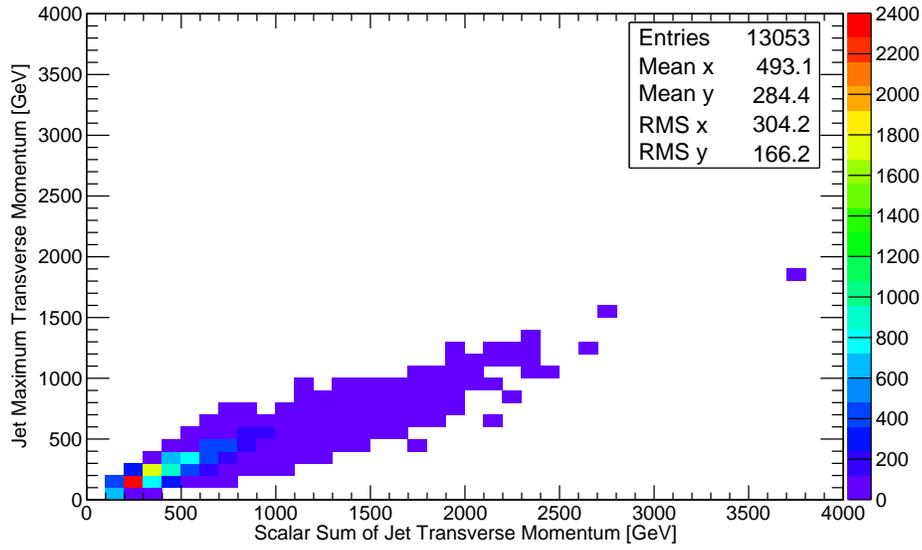
Figure 6.13: ATLAS data: Two-dimensional correlation plots of $\sum p_T$ and p_T^{1st} after the $N_{jet} \geq 2$ selection cut.
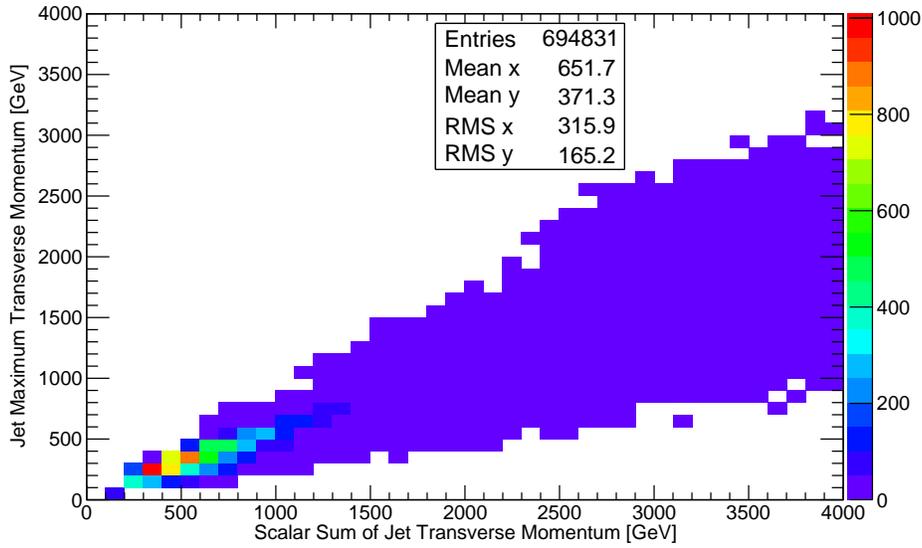
Figure 6.14: QCD: Two-dimensional correlation plots of $\sum p_T$ and p_T^{1st} after the $N_{jet} \geq 2$ selection cut.
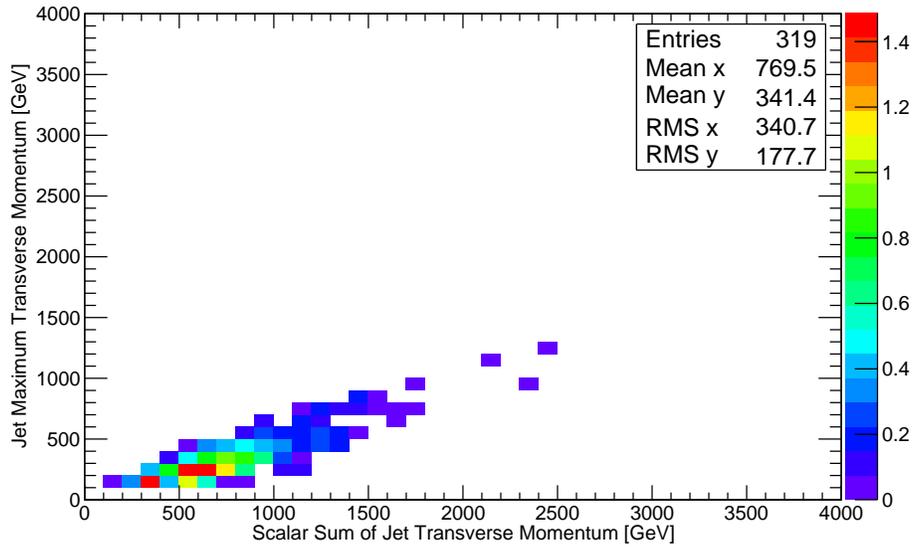
Figure 6.15: $t\bar{t}$: Two-dimensional correlation plots of $\sum p_T$ and p_T^{1st} after the $N_{jet} \geq 2$ selection cut.
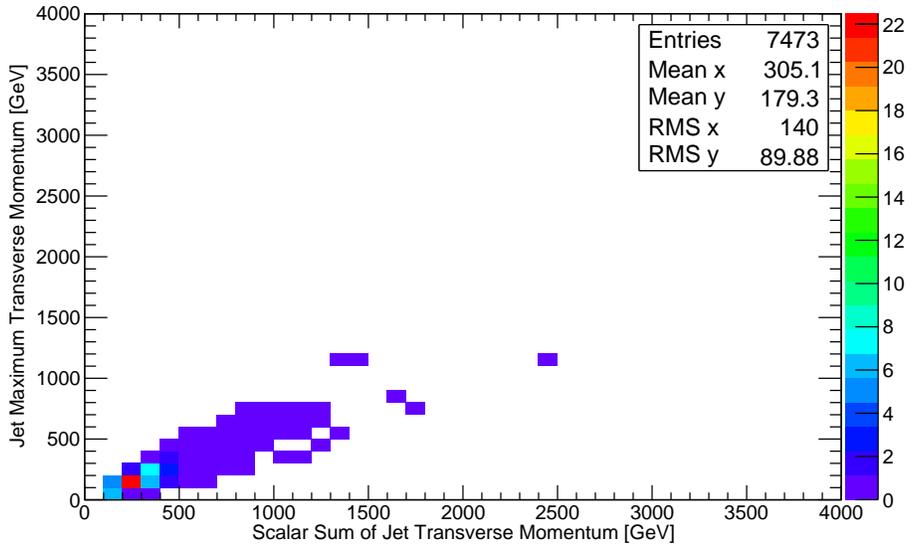
Figure 6.16: $W+$ jets: Two-dimensional correlation plots of $\sum p_T$ and p_T^{1st} after the $N_{jet} \geq 2$ selection cut.
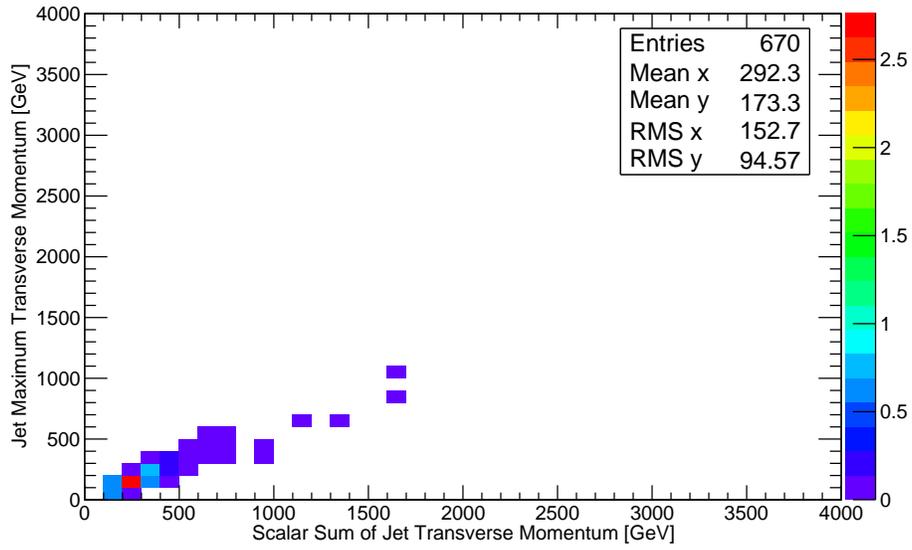
Figure 6.17: $Z+$ jets: Two-dimensional correlation plots of $\sum p_T$ and p_T^{1st} after the $N_{jet} \geq 2$ selection cut.
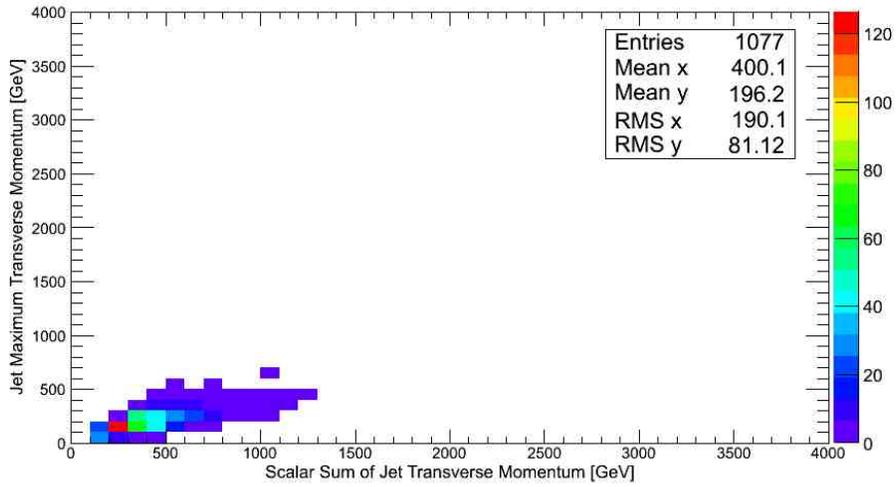
Figure 6.18: Black Hole: Two-dimensional correlation plots of $\sum p_T$ and p_T^{1st} after the $N_{jet} \geq 2$ selection cut.
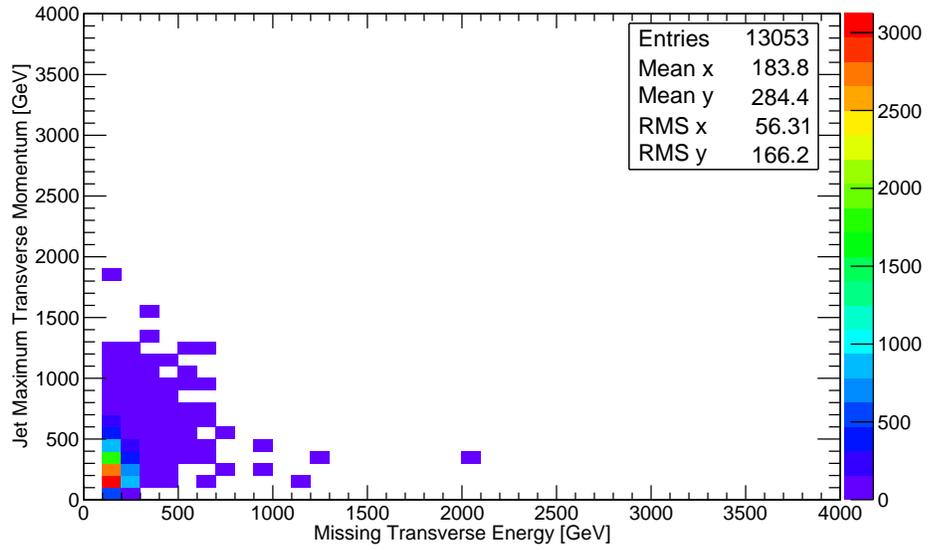
Figure 6.19: ATLAS data: Two-dimensional correlation plots of p_T^{1st} and missing transverse energy after the $N_{jet} \geq 2$ selection cut.
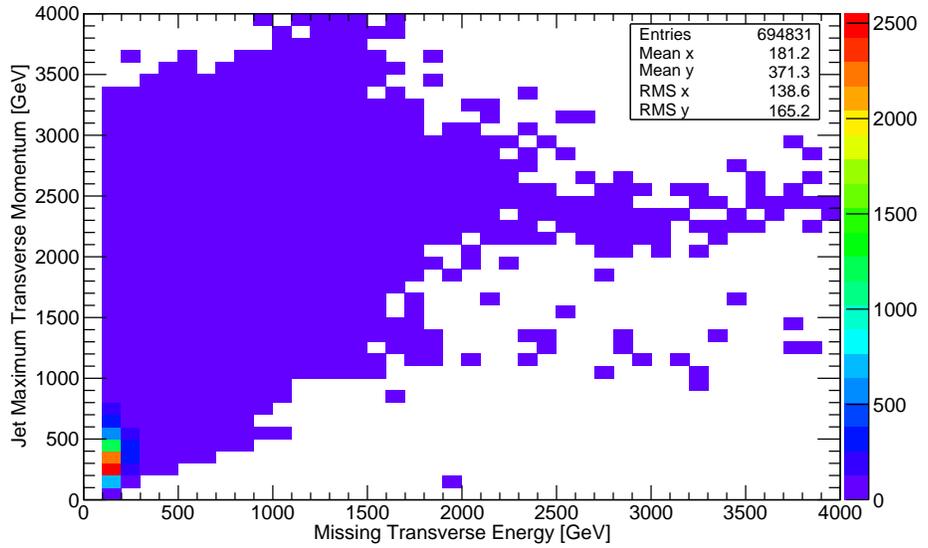
Figure 6.20: QCD: Two-dimensional correlation plots of p_T^{1st} and missing transverse energy after the $N_{jet} \geq 2$ selection cut.
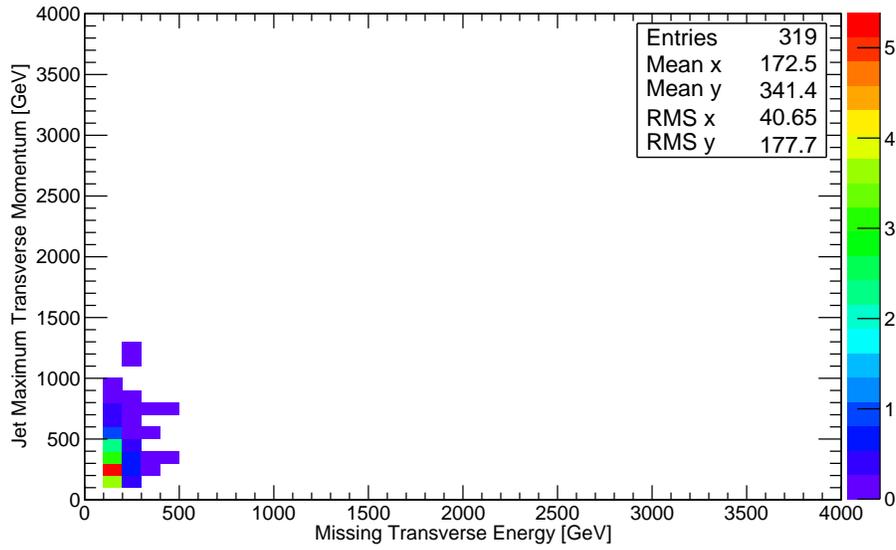
Figure 6.21: $t\bar{t}$: Two-dimensional correlation plots of p_T^{1st} and missing transverse energy after the $N_{jet} \geq 2$ selection cut.
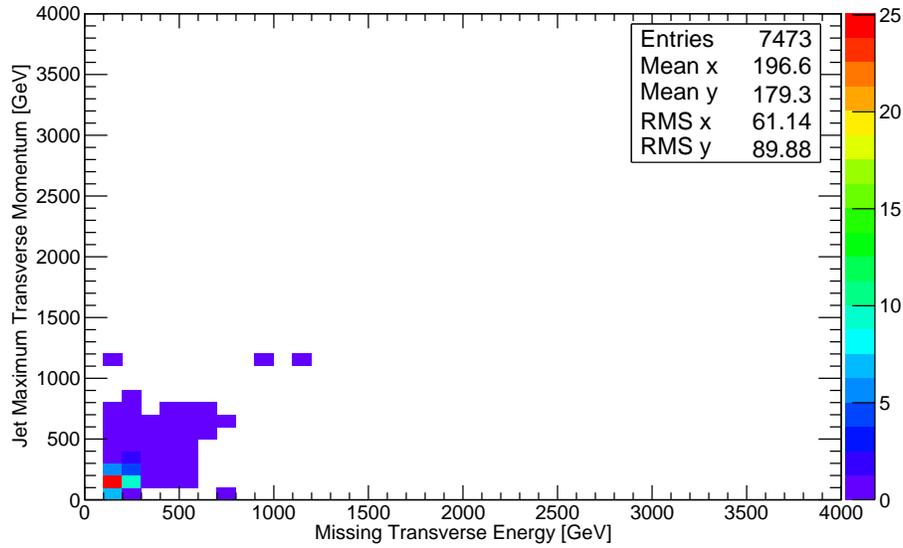
Figure 6.22: $W+$ jets: Two-dimensional correlation plots of p_T^{1st} and missing transverse energy after the $N_{jet} \geq 2$ selection cut.
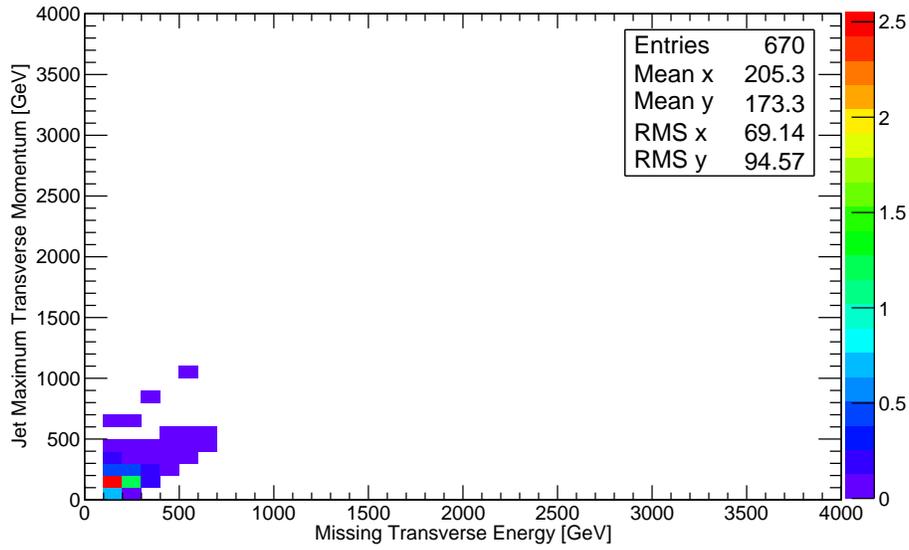
Figure 6.23: $Z+$ jets: Two-dimensional correlation plots of p_T^{1st} and missing transverse energy after the $N_{jet} \geq 2$ selection cut.
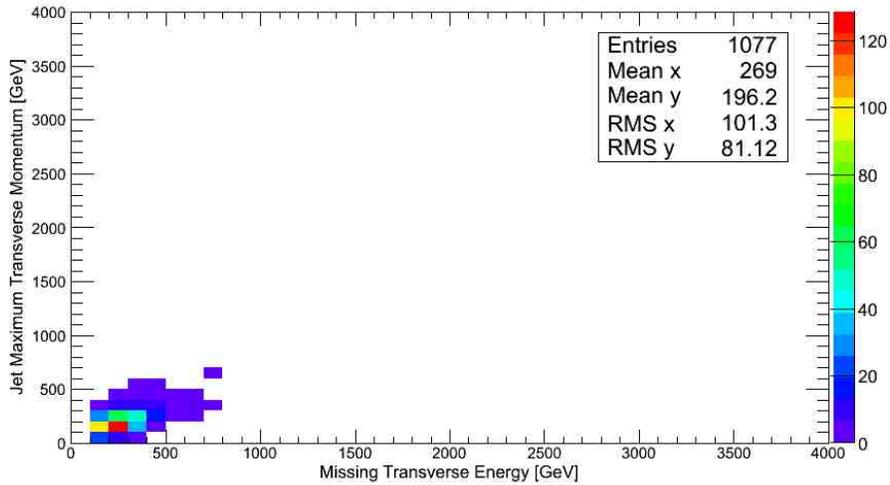
Figure 6.24: Black Hole: Two-dimensional correlation plots of p_T^{1st} and missing transverse energy after the $N_{jet} \geq 2$ selection cut.
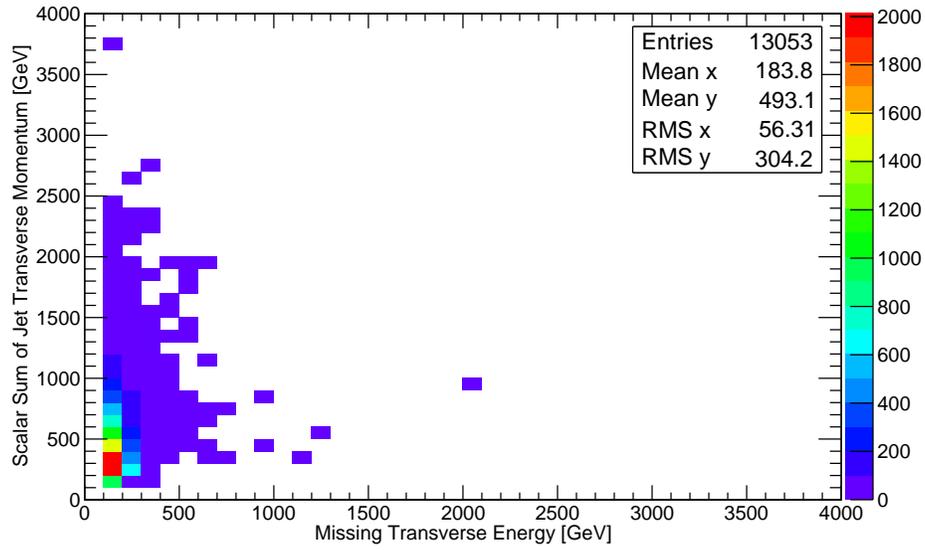
Figure 6.25: ATLAS data: Two-dimensional correlation plots of $\sum p_T$ and missing transverse energy after the $N_{jet} \geq 2$ selection cut.
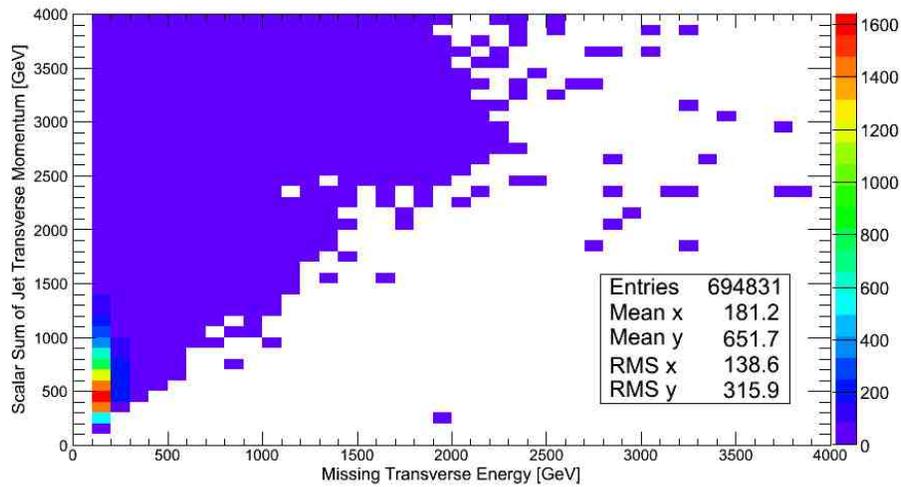
Figure 6.26: QCD: Two-dimensional correlation plots of $\sum p_T$ and missing transverse energy after the $N_{jet} \geq 2$ selection cut.
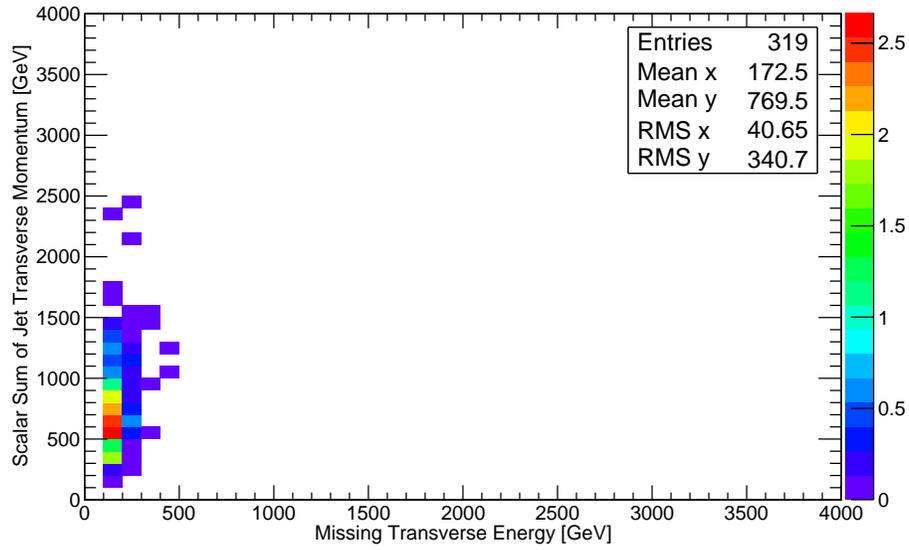
Figure 6.27: $t\bar{t}$: Two-dimensional correlation plots of $\sum p_T$ and missing transverse energy after the $N_{jet} \geq 2$ selection cut.
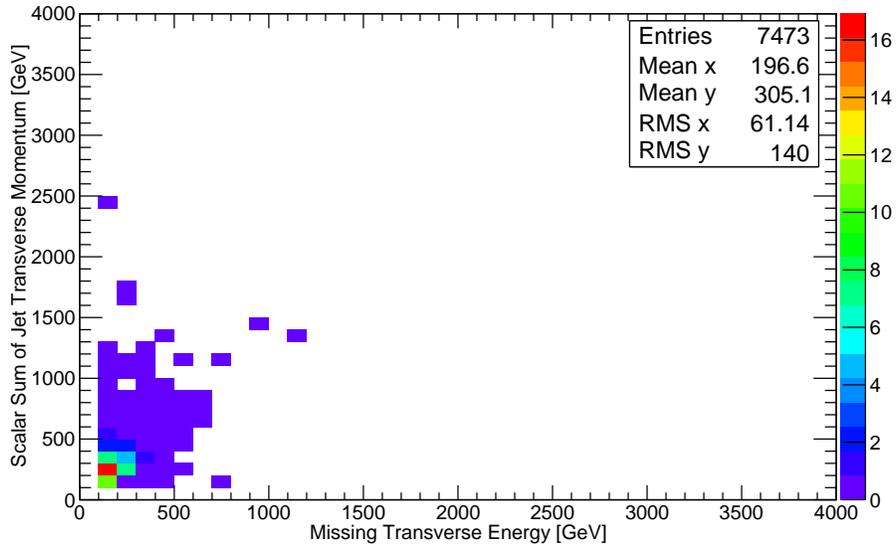
Figure 6.28: $W+$ jets: Two-dimensional correlation plots of $\sum p_T$ and missing transverse energy after the $N_{jet} \geq 2$ selection cut.
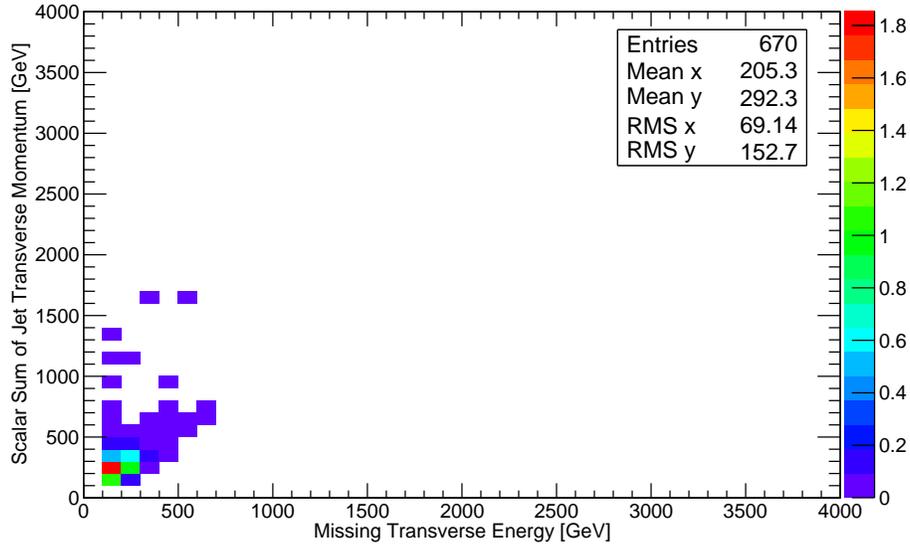
Figure 6.29: $Z+$ jets: Two-dimensional correlation plots of $\sum p_T$ and missing transverse energy after the $N_{jet} \geq 2$ selection cut.
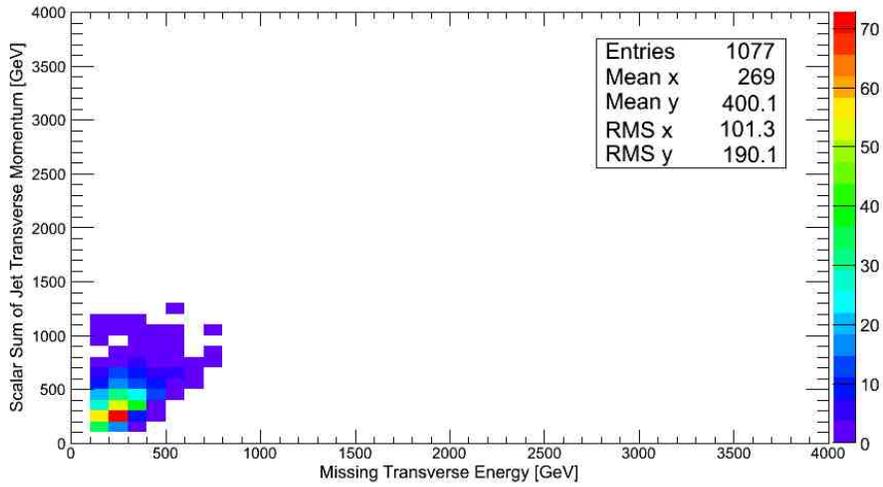
Figure 6.30: Black Hole: Two-dimensional correlation plots of $\sum p_T$ and missing transverse energy after the $N_{jet} \geq 2$ selection cut.

Figures 6.19 through 6.30 show an uncorrelated distribution of the leading jet transverse momentum and scalar sum of the jet transverse momentum with respect to the missing transverse energy. Since these distributions are uncorrelated, we con-

clude a combination of these kinematic variables (leading jet transverse momentum, scalar sum of jet transverse momentum and missing transverse energy) are good candidates to reduce the QCD background events which clearly dominates over the black hole signal. We derived a parameter by plotting the distribution of the ratios of the leading jet transverse momentum and missing transverse energy, and scalar sum of jet transverse momentum and missing transverse energy as shown in Figures 6.31 and 6.32.
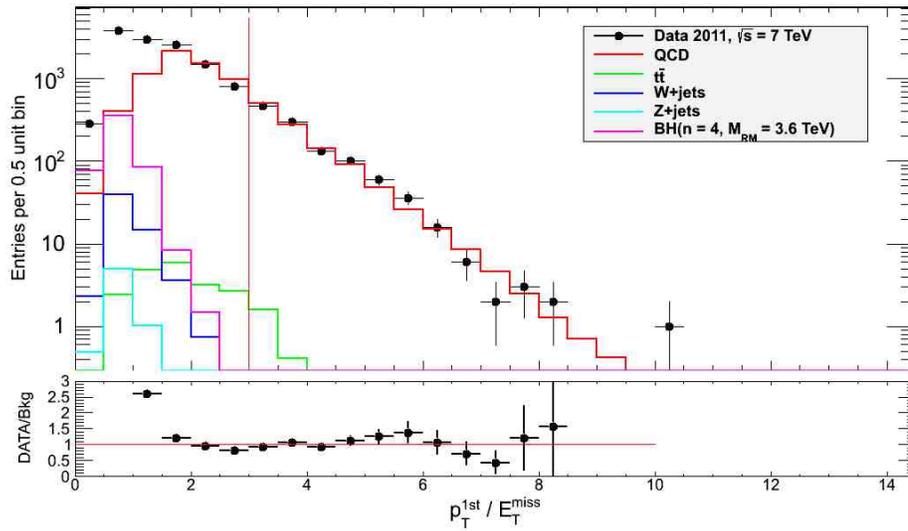
Figure 6.31: $p_T^{1st}/E_T^{\mathrm{miss}}$: Comparison of distribution of $p_T^{1st}/E_T^{\mathrm{miss}}$ after the $N_{jet} \geq 2$.
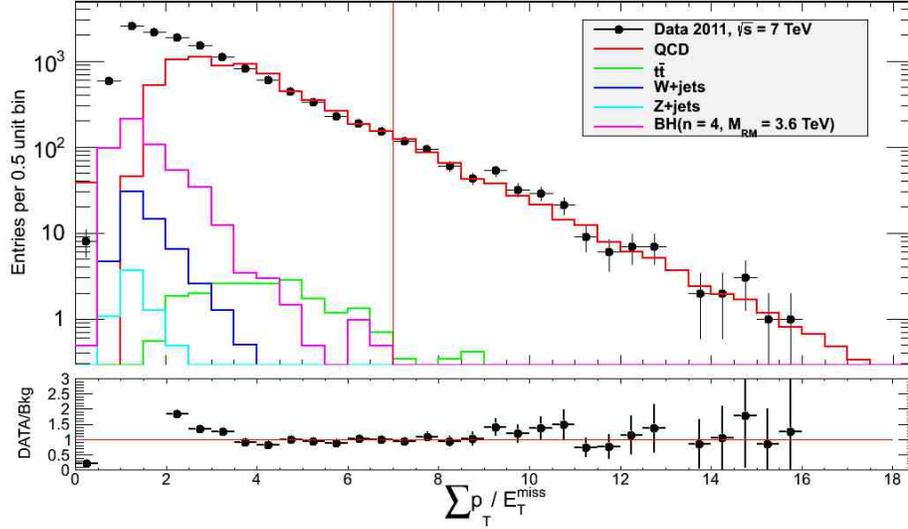
Figure 6.32: $\sum p_T/E_T^{\mathrm{miss}}$: Comparison of distribution of $\sum p_T/E_T^{\mathrm{miss}}$ after the $N_{jet} \geq 2$.

6.D.4 $\sum p_T/E_T^{\mathrm{miss}} < 7$ and $p_T^{1st}/E_T^{\mathrm{miss}} < 3$ selection cuts

Finally, we apply selection cuts derived from the ratio plots of the leading jet transverse momentum and missing transverse energy, and scalar sum of jet transverse momentum and missing transverse energy as shown in Figures 6.31 and 6.32, to further reduce our background sample. The $\sum p_T/E_T^{\mathrm{miss}} < 7$ cut optimizes the black hole signal, while the $p_T^{1st}/E_T^{\mathrm{miss}} < 3$ cut leaves the number of signal events unchanged. On the hand, the background was reduced after the $\sum p_T/E_T^{\mathrm{miss}} < 7$ and $p_T^{1st}/E_T^{\mathrm{miss}} < 3$ cuts.

Figures 6.33 through 6.36 show distributions after the $p_T^{1st}/E_T^{\mathrm{miss}}$ selection cut for the jet multiplicity (Figure 6.33), missing transverse energy (Figure 6.34), jet leading transverse momentum (Figure 6.35) showing a tail reduction by about 250 GeV and scalar sum of jet transverse momentum (Figure 6.36) showing a tail reduction of about 1 TeV.
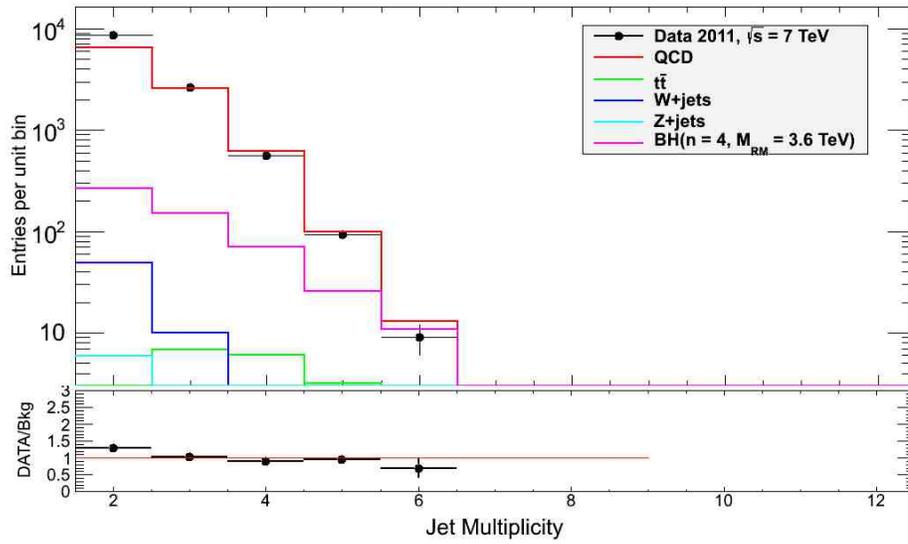
Figure 6.33: Jet multiplicity: Comparison of distribution of jet multiplicity after the $p_T^{1st}/E_T^{\mathrm{miss}}$ selection cut.
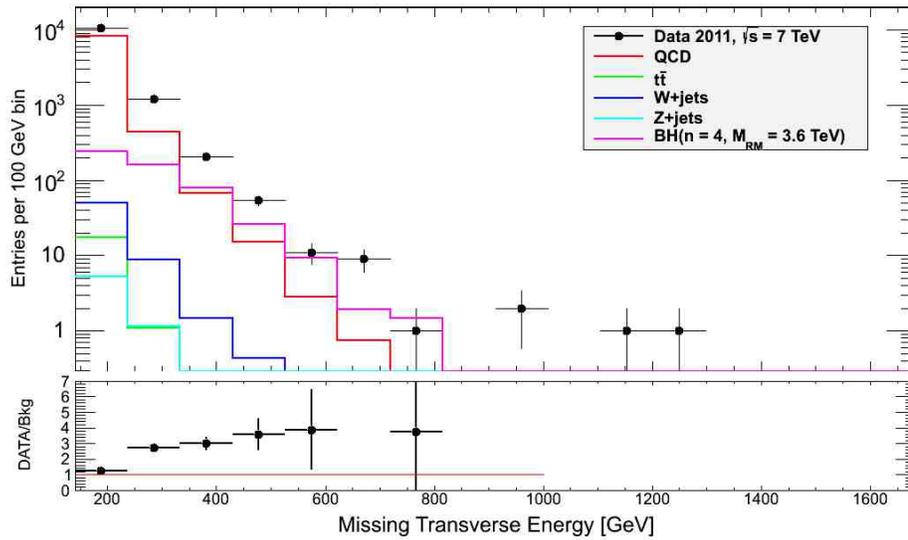
Figure 6.34: Missing transverse energy: Comparison of distribution of missing transverse energy after the $p_T^{1st}/E_T^{\mathrm{miss}}$ selection cut.
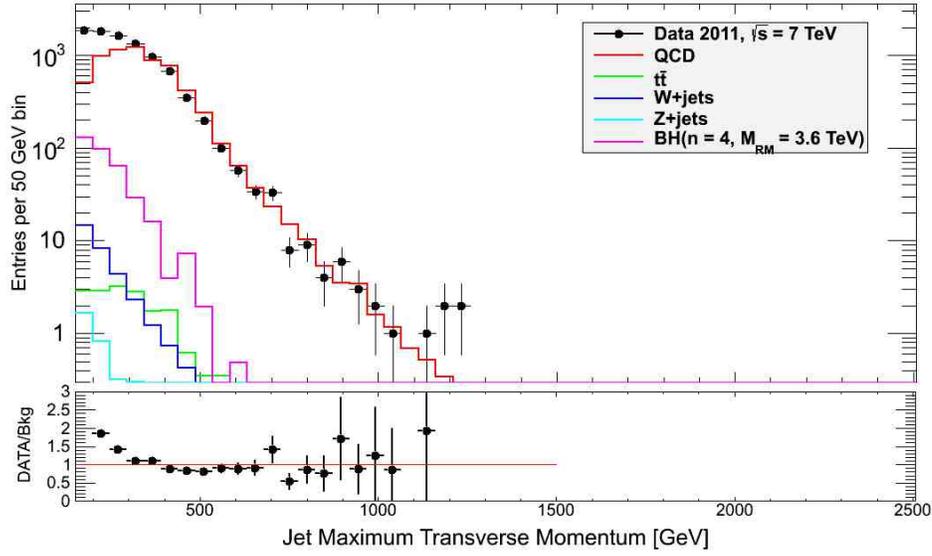
Figure 6.35: Comparison of distribution of leading jet p_T after the p_T^{1st}/E_T^{miss} selection cut.
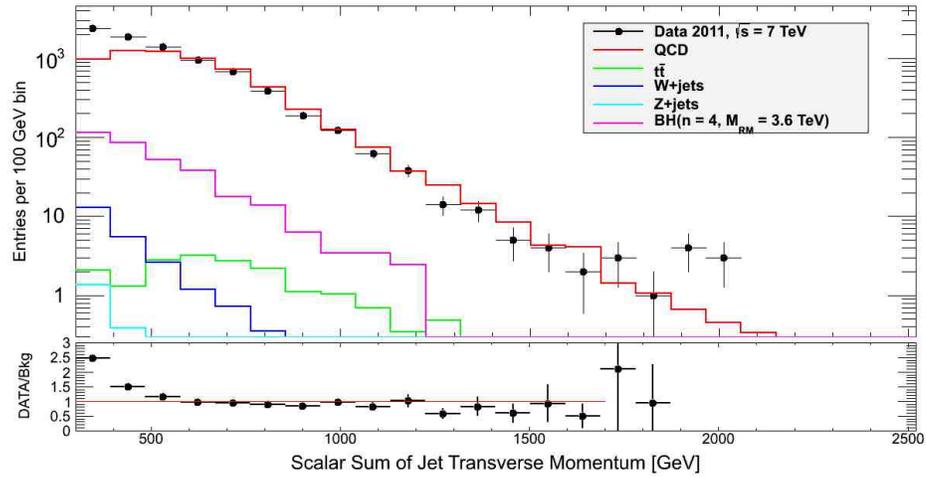
Figure 6.36: Comparison of jet $\sum p_T$ distribution after the p_T^{1st}/E_T^{miss} selection cut.

6.E   Black Hole Discovery Potential at the LHC

The black hole discovery potential in ATLAS has been evaluated by applying the selection criteria in Section 6.D. Table 6.12 shows the numbers of signal and background events normalized to the integrated luminosity of the data after each selection cut and the statistical significance of black hole discovery, respectively.

In order to observe any discovery in ATLAS, we follow the ATLAS physics performance [56] definition of signal significance, P,

$$P = \frac{S}{\sqrt{B}}, \tag{6.8}$$

where S and B are the number of signal and background events, respectively. The criterion for discovery is $P > 5$ and at least 10 observed signal events. Table 6.12 shows the corresponding selected number of events for signal and background samples as well as the $S/\sqrt{B}$ ratios. The last column of Table 6.12 shows the significance of the MC simulated sample.

Selection cut	QCD	Z+jets	W+jets	$t\bar{t}$	Bkg	Black Hole	$S/\sqrt{B}$
$E_T^{\text{miss}} > 140$ GeV	1.1×10^4	20.6	172.2	22.2	1.2×10^4	851.5	7.9
$N_{jet} \geq 2$	1.1×10^4	6.8	61.1	22.0	1.1×10^4	526.5	5.1
$\sum p_T / E_T^{\text{miss}} < 7$	6495.7	6.8	61.0	20.0	6583.5	526.5	6.5
$5\ p_T^{1st} / E_T^{\text{miss}} < 3$	5529.6	6.8	60.9	18.7	5616.0	526.5	7.0

Table 6.12: Ratio $S/\sqrt{B}$ for the physics selection criteria.

Chapter 7

Summary

The possibility for new physics beyond the Standard Model has been studied through noncommutative inspired geometry. This model considers the extra dimensions model of Arkani-Hamed, Dimopoulos and Dvali (ADD) at low-scale gravity in order to observe the effects of noncommutativity. The gravitational radius was determined using the noncommutative ADD model. In this model, black holes have minimum mass, called the remnant mass after decaying and the remnant mass can be above the Planck scale contrary to several quantum gravity models that predicts the remnant to be at the Planck scale.

By considering experimental limits on the Planck scale and the energy reach of the LHC, one can restrict the parameter space and calculate the production cross section for noncommutative inspired black holes.

A sensitive study for noncommutative inspired black hole events was conducted with a total luminosity of 502 ± 9 pb^{-1} of data from the Large Hadron Collider running at centre-of-mass energy, $\sqrt{s} = 7$ TeV. Noncommutative black hole events having a cross-section, $\sigma = 4.67$ pb were simulated with the following parameters: number of extra dimensions, $n = 4$, D-dimensional Planck scale, $M_D = 0.94$ TeV, $\sqrt{\theta} = 0.64$ TeV^{-1} and remnant mass of 3.6 TeV, while the following Standard Model

samples were used to estimate the background: QCD, $t\bar{t}$, $W+$ jets and $Z+$jets.

Standard Model simulated background events were reduced by selection cuts derived from trigger efficiency studies, and analysis using the following variables: jet multiplicity, jet maximum transverse momentum, scalar sum of jet p_T and missing transverse energy. After applying the selection cuts, 526 black hole events were left.

The sensitivity of black hole events using the ATLAS detector was estimated using the ATLAS statistical significance condition, P. With a value of $P > 5$. However, not all Standard Model simulated backgrounds events were used in this thesis and most importantly, the total MC simulated background events is less than the data. Therefore, we conclude that the ATLAS detector might be sensitive to black holes.

Bibliography

[1] N. Arkani-Hamed, S. Dimopoulos and G. R. Dvali, The Hierarchy problem and new dimensions at a millimeter, Phys. Lett. B **429**, 263 (1998) [hep-ph/9803315].

[2] K. Nakamura *et al.* [Particle Data Group Collaboration], Review of particle physics, J. Phys. G **37**, 075021 (2010).

[3] G. Aad *et al.* [ATLAS Collaboration], The ATLAS Experiment at the CERN Large Hadron Collider, JINST **3**, S08003 (2008).

[4] C. Lefevre, LHC: the guide, available at `http://cds.cern.ch/record/1092437/files/CERN-Brochure-2008-001-Eng.pdf`, 2008.

[5] D. Bourilkov, Gauge coupling unification, SUSY scale and strong coupling running, AIP Conf. Proc. **842**, 634 (2006) [hep-ph/0602168].

[6] C. M. Harris, Physics beyond the standard model: Exotic leptons and black holes at future colliders, [hep-ph/0502005].

[7] I. Antoniadis, N. Arkani-Hamed, S. Dimopoulos and G. R. Dvali, New dimensions at a millimeter to a Fermi and superstrings at a TeV, Phys. Lett. B **436**, 257 (1998) [hep-ph/9804398].

[8] R.C. Myers and M.J. Perry, Black Holes in Higher Dimensional Space-times, *Ann. Phys. (N.Y.)* **172**, 304-347 (1986).

[9] S. Dimopoulos and G. L. Landsberg, Black holes at the LHC, Phys. Rev. Lett. **87**, 161602 (2001) [hep-ph/0106295].

[10] S. W. Hawking, Particle Creation by Black Holes, Commun. Math. Phys. **43**, 199 (1975).

[11] G. L. Landsberg, Black Holes at Future Colliders and Beyond, J. Phys. G **32**, R337 (2006) [hep-ph/0607297].

[12] S. B. Giddings and S. D. Thomas, High-energy colliders as black hole factories: The End of short distance physics, Phys. Rev. D **65**, 056010 (2002) [hep-ph/0106219].

[13] D. M. Gingrich, Experimental limits on the fundamental Planck scale in large extra dimensions, arXiv:1210.5923 [hep-ex].

[14] D. M. Gingrich, Noncommutative geometry inspired black holes in higher dimensions at the LHC, JHEP **1005**, 022 (2010) [arXiv:1003.1798 [hep-ph]].

[15] T. G. Rizzo, Noncommutative Inspired Black Holes in Extra Dimensions, JHEP **0609**, 021 (2006) [hep-ph/0606051].

[16] ATLAS, Overall view of the LHC experiments, available at `http://www.atlas.ch/photos/atlas_photos/selected-photos/lhc/9906026_01_layout_sch.jpg`.

[17] General Detection - ATLAS Experiment - Photos, available at `http://atlas.ch/photos/events-general-detection.html`.

[18] G. Aad *et al.* [ATLAS Collaboration], The ATLAS Inner Detector commissioning and calibration, Eur. Phys. J. C **70**, 787 (2010) [arXiv:1004.5293 [physics.ins-det]].

[19] G. Aad *et al.*, ATLAS pixel detector electronics and sensors, JINST **3**, P07007 (2008).

[20] F. Hugging *et al.* , Studies on ATLAS pixel modules, International Workshop on Semiconductor Pixel Detectors for Particles and X-Ray (Pixel 2002), Carmel, CA, 2002.

[21] A. Ahmad *et al.*, The Silicon microstrip sensors of the ATLAS semiconductor tracker, Nucl. Instrum. Meth. A **578**, 98 (2007).

[22] E. Abat *et al.* [ATLAS TRT Collaboration], The ATLAS Transition Radiation Tracker (TRT) proportional drift tube: Design and performance, JINST **3**, P02013 (2008).

[23] A. Airapetian *et al.* [ATLAS Collaboration], ATLAS calorimeter performance Technical Design Report, CERN-LHCC-96-40.

[24] [ATLAS Collaboration], ATLAS tile calorimeter: Technical design report, CERN-LHCC-96-42.

[25] [ATLAS Collaboration], ATLAS muon spectrometer: Technical design report, CERN-LHCC-97-22.

[26] [ATLAS Collaboration], ATLAS high-level trigger, data acquisition and controls: Technical design report, CERN-LHCC-2003-022.

[27] See http://twiki.ific.uv.es/twiki/bin/view/Main/VictoriaSanchezMartinez

[28] G. Duckeck, (Ed.) *et al.* [ATLAS Collaboration], ATLAS computing: Technical design report, CERN-LHCC-2005-022.

101

[29] G. Corcella, I. G. Knowles, G. Marchesini, S. Moretti, K. Odagiri, P. Richardson, M. H. Seymour and B. R. Webber, HERWIG 6: An Event generator for hadron emission reactions with interfering gluons (including supersymmetric processes), JHEP **0101**, 010 (2001) [hep-ph/0011363].

[30] T. Sjostrand, P. Eden, C. Friberg, L. Lonnblad, G. Miu, S. Mrenna and E. Norrbin, High-energy physics event generation with PYTHIA 6.1, Comput. Phys. Commun. **135**, 238 (2001) [hep-ph/0010017].

[31] M. L. Mangano, M. Moretti, F. Piccinini, R. Pittau and A. D. Polosa, ALPGEN, a generator for hard multiparton processes in hadronic collisions, JHEP **0307**, 001 (2003) [hep-ph/0206293].

[32] J. A. Frost, J. R. Gaunt, M. O. P. Sampaio, M. Casals, S. R. Dolan, M. A. Parker and B. R. Webber, Phenomenology of Production and Decay of Spinning Extra-Dimensional Black Holes at Hadron Colliders, JHEP **0910**, 014 (2009) [arXiv:0904.0979 [hep-ph]].

[33] S. Agostinelli *et al.*, GEANT4: A simulation toolkit. Nucl. Instrum. Methods A **506**, 250-303 (2003).

[34] [ATLAS Collaboration], Improved luminosity determination in pp collisions at $\sqrt{s} = 7$ TeV using the ATLAS detector at the LHC, arXiv:1302.4393 [hep-ex].

[35] [ATLAS Collaboration], The ATLAS Simulation Infrastructure, Eur. Phys. J. C **70**, 823 (2010) [arXiv:1005.4568 [physics.ins-det]].

[36] A. Sherstnev and R. S. Thorne, Parton Distributions for LO Generators, Eur. Phys. J. C **55**, 553 (2008) [arXiv:0711.2473 [hep-ph]].

[37] S. Frixione, P. Nason and B. R. Webber, Matching NLO QCD and parton showers in heavy flavor production, JHEP **0308**, 007 (2003) [hep-ph/0305252].

[38] [Tevatron Electroweak Working Group and CDF and D0 Collaborations], Combination of CDF and D0 results on the mass of the top quark using up to 5.8 fb^{-1} of data, arXiv:1107.5255 [hep-ex].

[39] J. Pumplin, D. R. Stump, J. Huston, H. L. Lai, P. M. Nadolsky and W. K. Tung, New generation of parton distributions with uncertainties from global QCD analysis, JHEP **0207**, 012 (2002) [hep-ph/0201195].

[40] J. M. Butterworth, J. R. Forshaw and M. H. Seymour, Multiparton interactions in photoproduction at HERA, Z. Phys. C **72**, 637 (1996) [hep-ph/9601371].

[41] [ATLAS Collaboration], New ATLAS event generator tunes to 2010 data, ATL-PHYS-PUB-2011-008.

[42] C.M. Harris, P. Richardson and B.R. Webber, CHARYBDIS: A black hole event generator, JHEP **08**, 033 (2003) [arXiv:0307305 [hep-ph]].

[43] E. Boos *et al.*, Generic user process interface for event generators, hep-ph/0109068.

[44] W. Lampl *et al.*, Calorimeter clustering algorithms: Description and performance, ATL-LARG-PUB-2008-002.

[45] M. Cacciari, G. P. Salam and G. Soyez, The Anti-k(t) jet clustering algorithm, JHEP **0804**, 063 (2008) [arXiv:0802.1189 [hep-ph]].

[46] M. Aharrouche *et al.*, Measurement of the response of the ATLAS liquid argon barrel calorimeter to electrons at the 2004 combined test-beam, Nucl. Instrum. Meth. A **614**, 400 (2010).

[47] E. Abat *et al.*, Response and shower topology of 2 to 180 GeV pions measured with the ATLAS barrel calorimeter at the CERN test-beam and comparison to Monte Carlo simulations, ATL-CAL-PUB-2010-001.

[48] [ATLAS Collaboration], Response of the ATLAS calorimeters to single isolated hadrons produced in proton proton collisions at a center of mass energy of $\sqrt{s} = 900$ GeV, ATLAS-CONF-2010-017.

[49] [ATLAS Collaboration], Properties of Jets and Inputs to Jet Reconstruction and Calibration with the ATLAS Detector Using Proton-Proton Collisions at $\sqrt{s} = 7$ TeV, ATLAS-CONF-2010-053.

[50] [ATLAS Collaboration], Jet energy scale and its systematic uncertainty for jets produced in proton-proton collisions at $\sqrt{s} = 7$ TeV and measured with the ATLAS detector, ATLAS-CONF-2010-056.

[51] [ATLAS Collaboration], Jet energy resolution and selection efficiency relative to track jets from in-situ techniques with the ATLAS Detector Using Proton-Proton Collisions at a Center of Mass Energy $\sqrt{s} = 7$ TeV, ATLAS-CONF-2010-054.

[52] [ATLAS Collaboration], Data-Quality Requirements and Event Cleaning for Jets and Missing Transverse Energy Reconstruction with the ATLAS Detector in Proton-Proton Collisions at a Center-of-Mass Energy of $\sqrt{s} = 7$ TeV, ATLAS-CONF-2010-038.

[53] [ATLAS Collaboration], Performance of the Missing Transverse Energy Reconstruction and Calibration in Proton-Proton Collisions at a Center-of-Mass Energy of 7 TeV with the ATLAS Detector, ATLAS-CONF-2010-057.

[54] E. Bouhova-Thacker *et al.*, Vertex Reconstruction in the ATLAS Experiment at the LHC, ATL-INDET-PUB-2009-001.

[55] M. Baak *et al.*, Data Quality Status Flags and Good Run Lists for Physics Analysis in ATLAS. ATLAS Note ATLCOM-GEN-2009-015, CERN, Geneva, 2009.

[56] [ATLAS Collaboration], ATLAS: Detector and physics performance technical design report. Volume 1, CERN-LHCC-99-14.